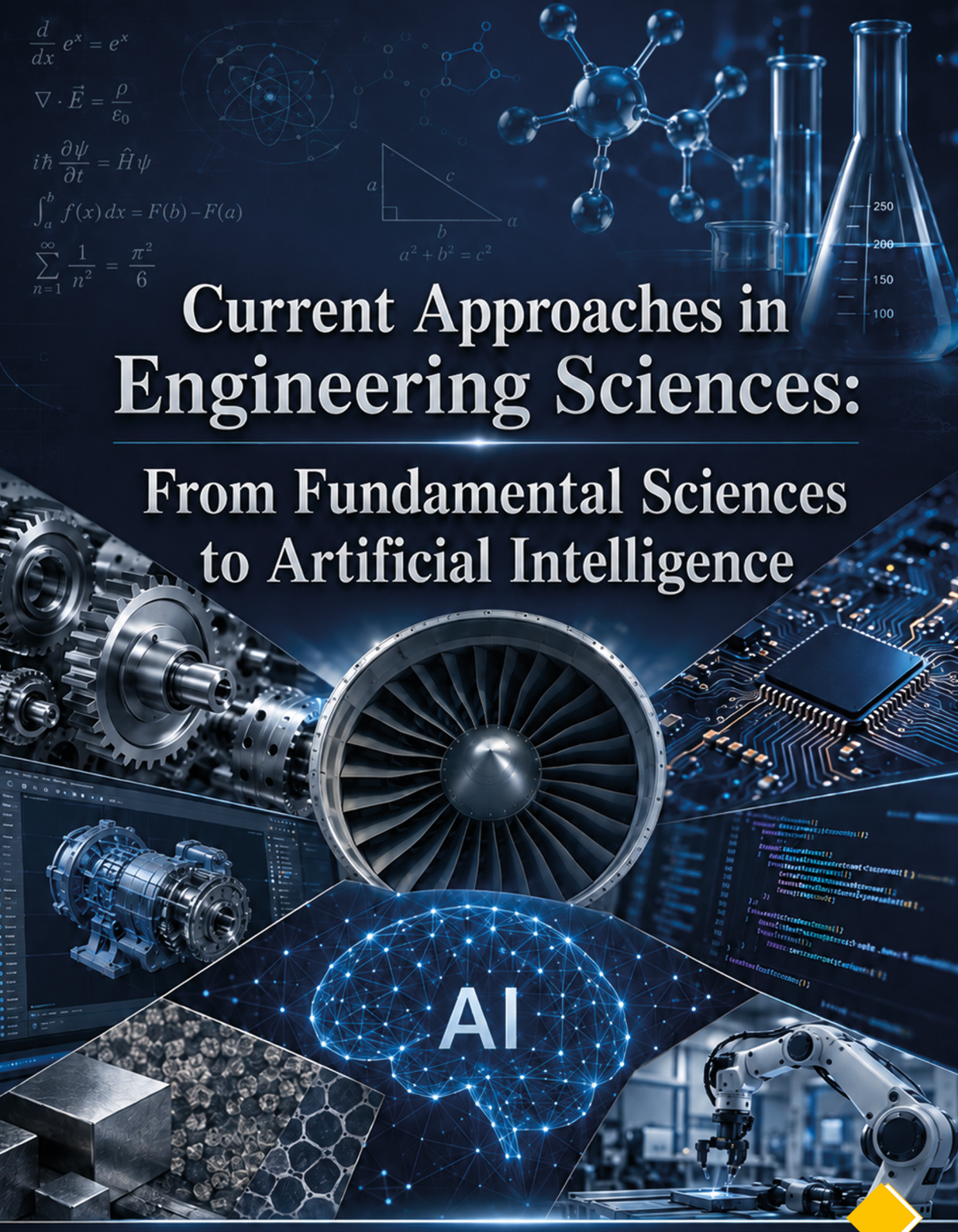
Current Approaches in Engineering Sciences:

From Fundamental Sciences to Artificial Intelligence



Editors: Assoc. Prof. Dr. Mehmet AKKAŞ
Assoc. Prof. Dr. Musa KILIÇ
and Prof. Dr. İhsan KIRIK

DUVAR

CURRENT APPROACHES IN ENGINEERING SCIENCES:

From Fundamental Sciences to Artificial Intelligence

Editors

Assoc. Prof. Dr. Mehmet AKKAŞ

Assoc. Prof. Dr. Musa KILIÇ

and Prof. Dr. İhsan KIRIK



Current Approaches in Engineering Sciences: From Fundamental Sciences to Artificial Intelligence
Assoc. Prof. Dr. Mehmet AKKAŞ,
Assoc. Prof. Dr. Musa KILIÇ, and Prof. Dr. İhsan KIRIK

General Director: Berkan Balpetek
Cover and Page Design: Duvar Design
Printing : November-2026
Publisher Certificate No: 49837
E-ISBN: 978-625-5471-36-9

© Duvar Yayınları
853 Sokak No:13 P.10 Kemeraltı-Konak/İzmir
Tel: 0 232 484 88 68
www.duvaryayinlari.com
duvarkitabevi@gmail.com

"The authors bear full responsibility for the sources, opinions, findings, results, tables, figures, images, and all other content presented in the chapters of this book. They are solely accountable for any financial or legal obligations that may arise in connection with national or international copyright regulations.The publisher and editors shall not be held liable under any circumstances"

TABLE OF CONTENTS

Chapter 1 1
A Comparative Analysis of YOLO Models for Steel Surface Defect Detection
Deniz KORKMAZ, Hakan AÇIKGÖZ

Chapter 2 14
Characterization of Alloy Steels Tensile Properties of
Cr-Ni Reinforced PM AISI 4140 Steel
Mehmet Akif ERDEN, Burak AYVACI, Bekir GÜNEY

Chapter 3 29
Seeing What Nano YOLO Detectors See:Military Aircraft Recognition
Ertuğrul DOĞRULUK

Chapter 4 38
Powder Metallurgy Processing of W-Based Cutting Tools: Impact of Alloy
Chemistry on Microstructure and Mechanical Performance
Aboubaker Alferjani H. ALRAJHE, Zakaria Ahmad Farag ALDALİMİ,
Mehmet AKKAŞ

Chapter 5 48
Industrial Applications of Laser Technology and Future Perspectives
Bekir GÜNEY, Mehmet Akif ERDEN

Chapter 6 70
Intravenous (IV) Stand with Human Following Ability and Its Prototype Study
Oktay ADIYAMAN

Chapter 7 91
GUI-Based Image Processing for Automated Delamination Detection and Quantification in Composite Laminates
Şehmus BADAY, Hüseyin GÜRBÜZ, Mehmet Emin DEMİR

Chapter 8 107
Microstructural Engineering of Fiber Modified Thermoplastic Composites for Lightweight Aerospace Components
Mehmet AKKAŞ

Chapter 1

A Comparative Analysis of YOLO Models for Steel Surface Defect Detection

Deniz KORKMAZ[1], Hakan AÇIKGÖZ[2]

1. INTRODUCTION

In industrial production processes, it is essential to reliably evaluate product quality, maintain production efficiency, and ensure the sustainable adherence to quality standards. As steel is a material widely used across various sectors such as the automotive, machinery manufacturing, railway, and construction industries, the surface quality of steel products is critical both for product performance and for the reliability of production processes. During the production of hot-rolled steel strips, in particular, various surface defects can arise due to mechanical factors, material properties, and specific production conditions. Failure to identify these defects in a timely manner can lead to the passage of defective products into subsequent stages of the production line, resulting in quality losses and additional production costs. Consequently, the rapid and reliable detection of surface defects has become a key area of research within automated industrial quality control systems (Song and Yan, 2013; Kou et al., 2021).

Classical surface defect detection methods primarily rely on expert observation, image processing techniques, and predefined visual features. In this context, the objective is to distinguish defects from normal surface regions by utilizing characteristics such as edge information, local texture, gray-level distribution, and regional contrast. On the other hand, the development of deep learning methods is enabled the analysis of surface defects through features automatically learned from images. Convolutional Neural Networks (CNNs) make it possible to represent complex visual patterns by learning low- and high-level features from images across successive layers. This approach allows for the simultaneous learning of various visual characteristics, rather than evaluating defects based solely on specific texture or edge features. The Northeastern University Surface Defect Database (NEU-DET),

[1] Assoc. Prof. Dr. Department of Electrical and Electronics Engineering, Faculty of Engineering and Natural Sciences, Malatya Turgut Ozal University, Malatya, 44900, Turkey; e-mail: deniz.korkmaz@ozal.edu.tr, ORCID ID: 0000-0002-5159-0659
[2] Assoc. Prof. Dr. Department of Software Engineering, Faculty of Engineering, Architecture and Design, Istiklal Science and Technology University, Kahramanmaraş, 46050, Turkey; e-mail: hakan.acikgoz@istiklal.edu.tr, ORCID ID: 0000-0002-6432-7243 *Corresponding Author: hakan.acikgoz@istiklal.edu.tr

a significant research resource for the deep learning-based detection of steel surface defects, contains images acquired from the surfaces of hot-rolled steel. Introduced by Song and Yan (2013), this database is widely used in the literature for the development and evaluation of methods aimed at the automated recognition of surface defects. The standard NEU-DET dataset consists of six defect classes, each containing 300 images, for a total of 1,800 grayscale images, each measuring 200 × 200 pixels. These classes are identified as crazing, inclusions, patches, pitted surfaces, rolled-in scale, and scratches. The fact that the defects in the dataset vary in terms of texture, shape, spatial distribution, and distinctiveness provides a suitable experimental environment for evaluating various detection architectures (Song and Yan, 2013; Chazhoor et al., 2024).

Single-stage methods developed in the field of object detection represent a significant alternative for industrial applications that require high processing speeds. These methods perform the detection process in an integrated manner by predicting the classes and locations of objects within an image through a single network. The You Only Look Once (YOLO) family is a prominent example of this approach. Research has been conducted on adapting YOLO architectures for the detection of defects on steel surfaces, examining the impact of various network structures and feature-processing mechanisms. Kou et al. (2021) developed a model based on YOLOv3, aiming to improve defect representation through connection-free feature-scale selection and dense convolutional blocks. The proposed method achieved a mean Average Precision (mAP) of 72.2% on the NEU-DET dataset. Qian et al. (2022) employed ShuffleNetV2 for feature extraction and a lightweight feature pyramid network for the more efficient fusion of multi-scale features. Furthermore, an adaptive receptive field feature extraction module was utilized to more effectively represent information regarding defects of varying sizes. The study reported an mAP of 79.23% on the NEU-DET dataset. Wang et al. (2022) utilized a weighted feature fusion approach in their YOLOv7-based steel surface defect detection model, incorporating the Efficient Channel Attention (ECA) mechanism to highlight significant feature channels and applying the SIoU loss function for bounding box regression. This study achieved an mAP of 81.9% on the NEU-DET dataset. In the YOLO model developed by Zhou and Zhao (2025), a multi-path convolutional attention module was employed. This module was integrated into the C2f structure; furthermore, a partial self-attention mechanism and auxiliary detection heads were added to model long-range feature dependencies and evaluate multi-level information. The study achieved an mAP of 81.5% on the NEU-DET dataset, representing a 3.4% improvement over the baseline YOLOv8 model. The method developed by Luo et al. (2025) is based on YOLOv8n and incorporates a spatial pyramid pooling structure with large separable kernels to support the detection of

multi-scale defects. Modifications made to the backbone and neck networks aim to reduce the model's computational cost. In this study, which achieved an mAP of 79.5% on the NEU-DET dataset, a 20.0% reduction in the number of parameters and a 15.5% reduction in floating-point operations were reported compared to the baseline YOLOv8n model. Research on steel surface defect detection is not limited to the YOLO family. Chazhoor et al. (2024) compared Faster R-CNN, Deformable DETR, Double Head R-CNN, RetinaNet, and Deformable CNN methods using the NEU dataset. In their study, which employed five-fold cross-validation, the Deformable Convolution Network achieved an accuracy of 77.28% based on the reported evaluation metric.

These developments in the literature highlight three fundamental requirements for the detection of steel surface defects. The first is the reliable identification of defects across various shapes and sizes. The second is achieving high detection performance in the classification of these defects. The third is ensuring that this performance is attained with an acceptable computational cost and inference speed. These requirements necessitate that model evaluation not be based solely on a single accuracy metric. In this study, the performance of YOLOv5nu, YOLOv8n, YOLO11n, and YOLO26n models in detecting steel surface defects is analyzed comparatively using the NEU-DET dataset. Within a consistent experimental framework, the models are evaluated based on detection performance metrics such as mAP@50, mAP@50–95, precision, recall, and F1-score as well as computational factors, including the number of parameters, GFLOPs, inference latency, and frames per second (FPS). The objective is to elucidate the relationship between detection performance and computational efficiency across different generations of the YOLO architecture. This study aims to contribute to the field by providing a unified evaluation approach for model performance on the NEU-DET dataset and by addressing the selection of models for industrial surface defect detection based on a variety of criteria.

2. NEU-DET Dataset

2.1. General Characteristics of the Dataset

NEU-DET is a dataset developed for the detection of defects on hot-rolled steel surfaces and is widely used in the literature. The dataset consists of a total of 1,800 grayscale images representing six distinct defect classes. Each class contains 300 images, and the images have a resolution of 200 x 200 pixels (Song and Yan, 2013). NEU-DET provides a suitable benchmark for evaluating the performance of object detection models, as the defects vary in terms of shape, size, texture, and contrast. However, the small image dimensions and the fact that some defects share similar visual characteristics can make accurate detection and localization challenging.

2.2. Defect Classes

NEU-DET covers six classes of defects found on steel surfaces; general information regarding these is provided in Table 1. Since these defects vary in terms of shape, size, texture, and distinctiveness, it is essential to evaluate the performance of detection models for each class individually. Therefore, this study aims to compare not only the overall performance of the YOLO models but also their specific capabilities in detecting different types of defects.

Table I. Steel Surface Defect Classes in the NEU-DET Dataset

Defect Class	Definition
Crazing	Fine, crack-like, and irregular structures.
Inclusion	Defects caused by foreign substances or particles on the surface.
Patches	Irregular regions exhibiting differences in texture and density.
Pitted Surface	Surface defects in the form of pits or cavities.
Rolled-in Scale	Defects resulting from an oxide layer embedded into the surface during the rolling process.
Scratches	Linear surface marks of varying lengths and orientations.

These classes allow for the comparison of models' abilities to recognize defects with distinct visual characteristics and to accurately determine their boundaries.

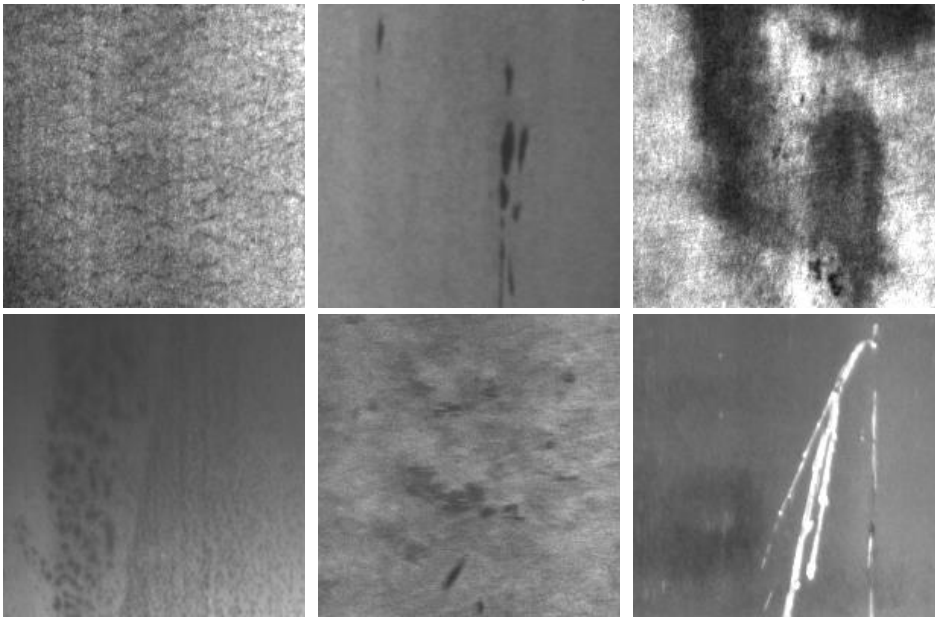


Figure 1. The samples of the six steel surface defect classes in the NEU-DET dataset

2.3. Preparation of the Dataset

In this study, the performances of the YOLOv5nu, YOLOv8n, YOLO11n, and YOLO26n models are compared using the NEU-DET dataset. In the experiments, images are scaled to an input size of 640 x 640 pixels, and the models are trained for 150 epochs with a batch size of 16. The 1,800 images in the dataset are randomly partitioned into training (70%), validation (15%), and testing (15%) sets. For a fair comparison, it is important to use the same data split, class mappings, and evaluation criteria across all models. Keeping the training, validation, and test sets separate from one another is essential for the reliability of the results.

3. YOLO-Based Object Detection Models

You Only Look Once (YOLO) is a family of real-time object detection methods designed to predict the locations and classes of objects within images through a single feed-forward network. Unlike traditional approaches, YOLO performs both localization and classification within a unified learning framework. This characteristic makes YOLO-based models a popular choice for image analysis applications that require high processing speeds (Redmon et al., 2016; Redmon & Farhadi, 2018). The general workflow of YOLO-based object detection can be described through five core components: the input image, feature extraction (backbone), multi-scale feature fusion (neck), the detection head, and the final detection output. While the structure of these components may vary depending on the specific YOLO version, the primary objective remains the same: to extract meaningful features from an image and use them to predict object classes and bounding box coordinates. The backbone extracts feature from the input image at various resolutions. The neck component fuses feature maps obtained at different scales, ensuring that both small and large objects are effectively represented. Finally, the detection head predicts the object classes and their locations. Depending on the application, the detection output typically includes a class label, a confidence score, and bounding box coordinates (Zhao et al., 2019).

The general characteristics of the YOLO models selected for this study can be described as follows. YOLOv5, developed by Ultralytics, is a family of models widely used in real-time object detection applications. The YOLOv5 architecture incorporates components such as convolutional feature extraction, Cross Stage Partial-based blocks, and the fusion of features at various resolutions. The Spatial Pyramid Pooling–Fast module contributes to the efficient representation of diverse spatial contexts (Jocher et al., 2020). YOLOv8 is a family of object detection models that adopts an anchor-free detection approach and utilizes C2f

blocks for feature extraction. The C2f structure aims to enhance feature flow and representation capacity by facilitating the integration of features obtained from intermediate layers. The architecture also employs multi-scale feature fusion components and a detection head that decouples classification from bounding box prediction (Jocher et al., 2023). YOLO11 is an object detection architecture developed by Ultralytics, which reorganizes the feature extraction and detection components found in previous model families. YOLO11 replaces the C2f blocks used in YOLOv8 with C3k2 blocks and incorporates the Cross-Stage Partial with Spatial Attention component into the feature extraction process. This design aims to support the learning of significant spatial relationships within an image while keeping computational costs under control (Jocher et al., 2024). YOLO26 is a family of models introduced by Ultralytics, focusing on real-time visual perception and deployment efficiency. One of the key innovations of YOLO26 is its end-to-end approach, which enables detection without the need for traditional non-maximum suppression during inference. This design employs a one-to-one prediction head, aiming to eliminate the requirement for post-processing steps to filter out redundant detections (Jocher et al., 2026).

4. Experimental Results and Discussion

4.1. Experimental Setup and Evaluation Criteria

In this study, the YOLOv5nu, YOLOv8n, YOLO11n, and YOLO26n models are evaluated on the NEU-DET dataset to compare their performance in detecting industrial surface defects. The comparison considers the models' detection capability, localization accuracy, computational cost, and inference speed. Specifically, the metrics include mean Average Precision (mAP@50), mAP@50–95, precision, recall, F1-score, number of parameters, GFLOPs, and frames per second (FPS). The experiments are conducted using an input resolution of 640 × 640, a batch size of 16, and a training duration of 150 epochs. Performance metrics are obtained using an NVIDIA GeForce RTX 5080 Laptop GPU. Latency measurements are based on the processing of a single image (batch size = 1). The inclusion of pre-processing, inference, and Non-Maximum Suppression (NMS) stages in this measurement protocol ensures that the results reflect the end-to-end computational cost, rather than just the forward-pass duration of the network.

4.2. Comparison of the Detection Performances of the YOLO Models

The experimental results for the four YOLO models on the NEU-DET dataset are presented in Table 2. The results indicate that the models establish different trade-offs between detection performance and computational efficiency.

Table II. Comparison of the performance of YOLO models on the NEU-DET dataset.

Metric	YOLOv5nu	YOLOv8n	YOLO11n	YOLO26n
Parameter	2.51 M	3.01 M	2.59 M	2.51 M
FLOPs	7.2 G	8.2 G	6.4 G	5.8 G
mAP@50	0.762	0.772	0.798	0.765
mAP@50–95	0.449	0.451	0.467	0.450
Precision	0.703	0.726	0.719	0.714
Recall	0.733	0.738	0.775	0.745
F1-Score	0.718	0.732	0.746	0.729
FPS	78	88	68	63

According to the results in Table 1, YOLO11n provides the highest values for mAP@50, mAP@50–95, recall, and F1 score. The model gives mAP@50 of 0.798, mAP@50–95 of 0.467, and F1 score of 0.746. These results indicate that YOLO11n stands out in terms of overall detection performance and the balance between precision and recall. YOLOv8n achieves the highest precision, with a value of 0.726. Furthermore, it delivered the fastest inference speed among the models compared, with a latency of 11.4 ms and a throughput of 88 FPS. Consequently, YOLOv8n can be considered a notable option for applications requiring the limitation of false-positive detections while maintaining high processing speeds. YOLOv5nu lags behind the other models, with mAP@50 of 0.762 and mAP@50–95 of 0.449. Nevertheless, its latency of 12.8 ms and performance of 78 FPS demonstrate that the model can achieve rapid inference with a relatively low computational cost. With 2.51 million parameters, YOLOv5nu is a viable option for deployment on systems with limited memory capacity. YOLO26n has the lowest theoretical computational cost among the models, at 5.8 GFLOPs. It also shares the same parameter count as YOLOv5nu—2.51 million. However, its latency of 15.8 ms and performance of 63 FPS indicate that it falls behind the other models in terms of measured inference speed. This finding suggests that theoretical computational cost alone does not determine inference speed on actual hardware. YOLO11n has the highest average values across both metrics, with mAP@50 of 0.798 and mAP@50–95 of 0.467. The corresponding values for YOLOv8n are 0.772 and 0.451, while those for YOLO26n are 0.765 and 0.450. YOLOv5nu yields the lowest average results,

with 0.762 mAP@50 and 0.449 mAP@50–95. The mAP@50 value for YOLO11n is 0.026 higher than that of YOLOv8n, which achieves the second-highest result. This difference corresponds to 2.6%. In terms of mAP@50–95, YOLO11n also outperforms YOLOv8n by 0.016. These findings indicate that, under the experimental conditions employed, YOLO11n delivers superior average detection performance at both the standard IoU threshold and more stringent localization thresholds.

In the experimental results, the highest precision value of 0.726 is achieved by YOLOv8n. The precision values for the YOLO26n, YOLO11n, and YOLOv5nu models are 0.714, 0.719, and 0.703, respectively. These results indicate that YOLOv8n offers a higher level of accuracy for positive detections compared to the other models. In terms of recall, YOLO11n reaches the highest value at 0.775. The recall values for YOLO26n (0.745), YOLOv8n (0.738), and YOLOv5nu (0.733) show that these models exhibit lower sensitivity than YOLO11n. A high recall metric is particularly desirable in applications where overlooking defects could lead to significant consequences in the quality control process. YOLO11n also gives the highest F1 score at 0.746, followed by YOLOv8n with 0.732, YOLO26n with 0.729, and YOLOv5nu with 0.718. The fact that YOLO11n maintains a high recall value alongside a relatively high precision value explains its superior F1-score.

In terms of the number of parameters, YOLOv5nu and YOLO26n are the smallest models, each with 2.51 million parameters. YOLO11n has 2.59 million parameters, while YOLOv8n has the highest count at 3.01 million. These findings indicate that while the differences in parameter counts among the models are not substantial, they could still be significant depending on deployment conditions. Regarding GFLOPs, YOLO26n has the lowest computational requirement at 5.8 GFLOPs, followed by YOLO11n at 6.4 GFLOPs, YOLOv5nu at 7.2 GFLOPs, and YOLOv8n at 8.2 GFLOPs. Conversely, the fact that YOLO26n exhibits the highest latency at 15.8 ms demonstrates that there is no direct, linear relationship between theoretical computational cost and actual operational speed. An analysis of the measured latency values reveals that YOLOv8n achieves the lowest latency at 11.4 ms, while YOLOv5nu, YOLO11n, and YOLO26n show latencies of 12.8 ms, 14.8 ms, and 15.8 ms, respectively. The corresponding FPS values are 88, 78, 68, and 63. These results indicate that, under the specified hardware and measurement conditions, YOLOv8n provides the highest inference speed. The observation that YOLO11n achieves the highest mAP@50 and F1 scores yet operates more slowly than YOLOv8n highlights a trade-off between accuracy and speed. Accordingly, while YOLO11n stands out for applications where high

detection accuracy is the priority, YOLOv8n may be a more suitable choice for scenarios that require lower latency and higher image processing speeds.

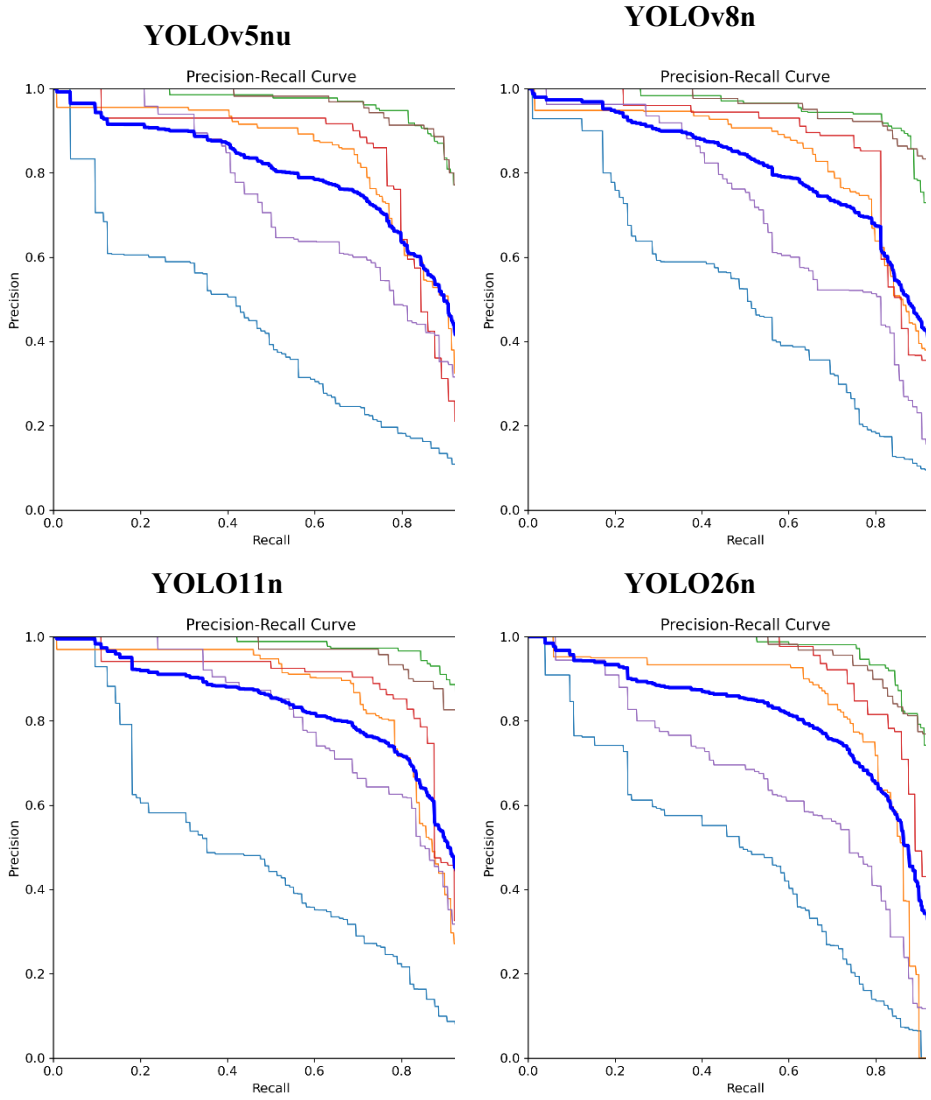


Figure 2. Precision–recall curves for the YOLOv5nu, YOLOv8n, YOLO11n, and YOLO26n models on the NEU-DET dataset.

Figure 2 compares the precision–recall curves for the four models. These curves illustrate the trade-off between precision and recall across various confidence thresholds. The overall curve for YOLO11n maintains relatively high precision values, particularly up to the high-recall region. This observation is consistent with the high mAP and F1 scores achieved by the model in its overall

performance metrics. Meanwhile, YOLOv8n exhibits high precision values within certain threshold ranges. However, the notable variations among the curves for different classes indicate that the models do not perform consistently across all types of defects.

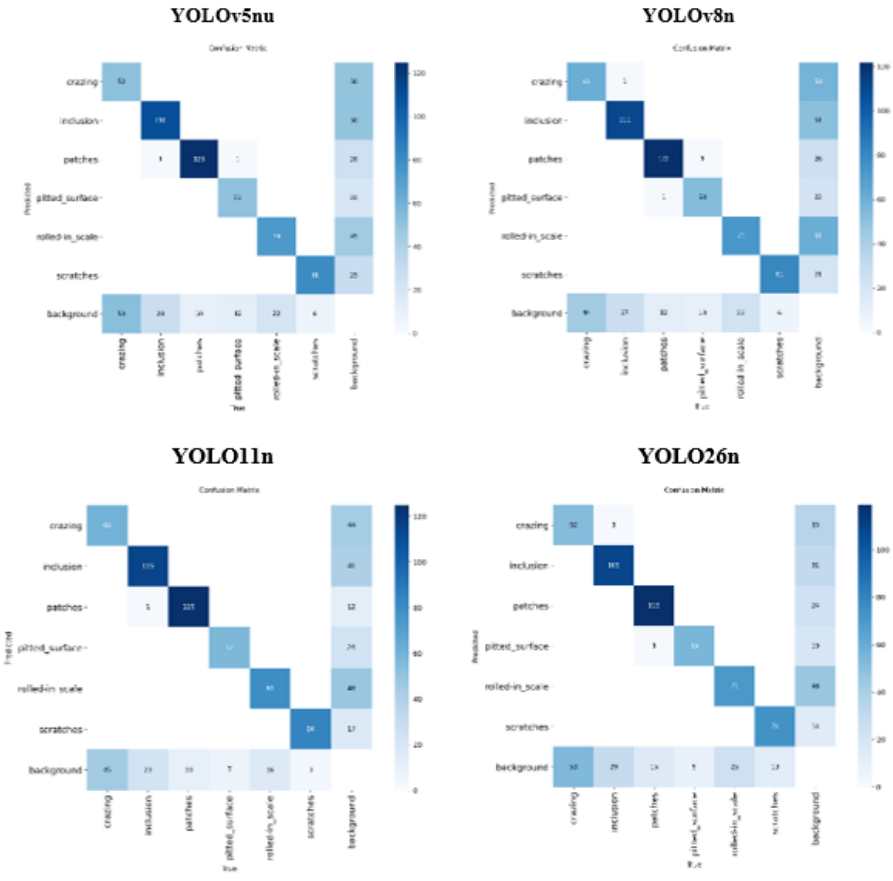


Figure 3. Confusion matrices for the YOLOv5nu, YOLOv8n, YOLO11n, and YOLO26n models on the NEU-DET dataset

Figure 3 shows the prediction results of the models across six surface defect classes and the background. The values along the diagonal of the confusion matrices represent correctly classified detections, while the off-diagonal values indicate misclassifications between classes. YOLO11n achieved a high number of accurate detections, particularly for the "inclusion," "patches," "rolled-in_scale," and "scratches" classes. YOLOv8n also demonstrated strong performance for the "crazing," "inclusion," and "scratches" classes. Conversely,

errors related to the background and confusion between certain defect classes were observed across all models. This suggests that the visual similarities among surface defects, as well as the presence of background patterns, can influence detection performance.

5. Conclusion

In this study, the performances of YOLOv5nu, YOLOv8n, YOLO11n, and YOLO26n models are evaluated comparatively for the detection of steel surface defects using the NEU-DET dataset. The models are analyzed in terms of accuracy, precision, recall, F1 score, number of parameters, computational cost, and inference speed. The results indicate that each model offers distinct advantages in terms of performance and efficiency. According to the experimental results, YOLO11n emerges as the most successful model in terms of overall detection performance, achieving mAP@50 of 0.798, mAP@50–95 of 0.467, and an F1-score of 0.746. Furthermore, with a recall value of 0.775, it outperforms the other models in detecting defects. These findings suggest that YOLO11n is a suitable choice for industrial quality control applications where detection accuracy is the primary requirement. In contrast, YOLOv8n has a precision value of 0.726 and an inference speed of 88 FPS, offering an advantage for applications that demand high processing speeds. Although YOLOv5nu and YOLO26n possess the smallest model size, they exhibit different inference speeds. Notably, while YOLO26n has the lowest theoretical computational cost at 5.8 GFLOPs, its inference speed reaches only 63 FPS. This demonstrates that theoretical computational cost is not the sole determinant of actual operational speed.

In conclusion, YOLO11n stands out for its high detection performance, while YOLOv8n excels in terms of inference speed and precision. Therefore, the choice of model should be guided by the specific requirements of the application regarding accuracy, speed, and available hardware resources. In future studies, validating these models using images captured under diverse industrial conditions and exploring model optimization techniques could help enhance their suitability for real-time quality control systems.

References

Chazhoor, A. A. P., Ho, E. S. L., Gao, B., & Woo, W. L. (2024). A review and benchmark on state-of-the-art steel defects detection. SN Computer Science, 5, Article 114. https://doi.org/10.1007/s42979-023-02436-2

Jocher, G., & Qiu, J. (2024). Ultralytics YOLO11 (Versiyon 11.0.0). https://github.com/ultralytics/ultralytics

Jocher, G., Chaurasia, A., & Qiu, J. (2023). Ultralytics YOLOv8 (Version 8.0.0). Ultralytics. https://github.com/ultralytics/ultralytics

Jocher, G., Qiu, J., Liu, M., Lyu, S., & Kalfaoglu, M. E. (2026). Ultralytics YOLO26: Unified real-time end-to-end vision models. arXiv. https://doi.org/10.48550/arXiv.2606.03748

Jocher, G., Stoken, A., Borovec, J., Changyu, L., Hogan, A., Diaconu, L., ... & Dave, P. (2020). ultralytics/yolov5: v2. 0. Zenodo.

Kou, X., Liu, S., Cheng, K., & Qian, Y. (2021). Development of a YOLO-V3-based model for detecting defects on steel strip surface. Measurement, 182, 109454. https://doi.org/10.1016/j.measurement.2021.109454

Qian, X., Wang, X., Yang, S., & Lei, J. (2022). LFF-YOLO: A YOLO algorithm with lightweight feature fusion network for Multi-Scale Defect Detection. IEEE Access, 10, 130339–130349. https://doi.org/10.1109/access.2022.3227205

Redmon, J., & Farhadi, A. (2018). YOLOv3: An incremental improvement. arXiv preprint arXiv:1804.02767. https://arxiv.org/abs/1804.02767

Redmon, J., Divvala, S., Girshick, R., & Farhadi, A. (2016). You only look once: Unified, Real-Time Object Detection. IEEE Computer Society Conference on Computer Vision and Pattern Recognition/Proceedings - IEEE Computer Society Conference on Computer Vision and Pattern Recognition/Proceedings, 779–788. https://doi.org/10.1109/cvpr.2016.91

Song, K., & Yan, Y. (2013). A noise robust method based on completed local binary patterns for hot-rolled steel strip surface defects. Applied Surface Science, 285, 858–864. https://doi.org/10.1016/j.apsusc.2013.09.002

Wang, Y., Wang, H., & Xin, Z. (2022). Efficient detection model of steel strip surface defects based on YOLO-V7. IEEE Access, 10, 133936–133944. https://doi.org/10.1109/ACCESS.2022.3230894

Zhang, C., Jin, J., Kong, C., Xu, Z., Guo, B., Tang, D., & Cao, Y. (2025). LIDD-YOLO: A lightweight industrial defect detection network. Measurement Science and Technology, 36(1), 0161b5. https://doi.org/10.1088/1361-6501/ad9d65

Zhao, Z., Zheng, P., Xu, S., & Wu, X. (2019). Object Detection with Deep Learning: A review. IEEE Transactions on Neural Networks and Learning Systems, 30(11), 3212–3232. https://doi.org/10.1109/tnnls.2018.2876865

Zhou, Y., & Zhao, Z. (2025). MPA-YOLO: Steel surface defect detection based on improved YOLOv8 framework. Pattern Recognition, 168, 111897. https://doi.org/10.1016/j.patcog.2025.111897

Chapter 2

Characterization of Alloy Steels Tensile Properties of Cr-Ni Reinforced PM AISI 4140 Steel

Mehmet Akif ERDEN[1], Burak AYVACI[2], Bekir GÜNEY[3]

1. INTRODUCTION

Steel is an iron-carbon alloy and is currently the most widely used engineering material. The carbon content is a determining factor in the classification of steels. Although steels can be classified in various ways, chemically they are divided into two groups: alloyed and unalloyed steels. Unalloyed steels consist of iron, carbon, and manganese. Although elements such as silicon, phosphorus, and sulfur are also present, they do not constitute the main components of the steel. They are inexpensive and easily formable. In unalloyed steels, mechanical properties vary depending on the carbon content. Their hardenability is low, and surface defects and dimensional distortions occur after hardening. Their corrosion resistance is low [1-2].

Alloyed steels are steels obtained by the addition of alloying elements. The alloying elements used provide improvements in mechanical properties compared with unalloyed steels. The addition of alloying elements increases the hardening depth. The addition of alloying elements also improves impact resistance. Corrosion resistance is low in unalloyed steels. In steels alloyed with chromium, corrosion resistance increases. Alloying increases fatigue resistance and wear resistance values in steels. Alloyed steels retain their mechanical properties even under different temperature conditions. The alloying elements generally required to obtain alloyed steels are nickel, chromium, molybdenum, manganese, silicon, wolfram, vanadium, niobium, aluminum, titanium, tungsten, lead, copper, and cobalt [3-9].

Hardening mechanisms used in alloyed steels, such as grain-size hardening, precipitation hardening, solid-solution hardening, and deformation hardening, increase the strength of steels. Among these hardening mechanisms, the grain-refinement mechanism increases strength while also improving toughness.

[1] Prof. Dr. Karabuk UniversityDepartment of Biomedical Engineering, Karabuk University, Karabuk 78050, Turkey; makiferden@karabuk.edu.tr, (ORCID: 0000-0002-6322-4269)
[2] Master's student, Graduate Education Institute, Department of Mechanical Engineering, Karabuk University, Karabuk 78050, Turkey; burak.ayvaci37@gmail.com
[3] Assoc. Prof. Dr., Vocational School of Technical Sciences, Karamanoglu Mehmetbey University, 70200, Karaman, Turkey; guneyb@kmu.edu.tr, (ORCID: 0000-0001-9764-9313)

Carburizing steels, which are included among alloyed steels, are steels with carbon contents below 0.2%. In materials subjected to the carburizing process, bending, wear, torsional fatigue resistance, and contact fatigue resistance are high [4]. After the carburizing process, the carbon content generally decreases from the surface, where it is highest, toward the core. The resulting hardness values also vary depending on the carbon content. Chromium is an alloying element that significantly affects the hardening depth of steel. At the same time, due to its strong carbide-forming property, it positively affects the hardness and wear resistance of steel. In addition to all these, the best-known property of chromium is that it increases the resistance of steel to rusting. Nickel-alloyed composite materials are an important field of study under present-day conditions. Nickel-alloyed materials are used in all kinds of industrial fields such as aircraft and gas turbines, rocket engines, nuclear reactors, steam-generating boilers, cutting tools, submarines, and the glass industry, and they continue to develop.

In iron-based materials, when nickel is used with chromium, it is used to increase the depth of hardening. Chromium-nickel-based stainless steels are resistant to scaling and heat. It increases the notch resistance of machine construction steels at low temperatures. If the desired properties include resistance to rusting and resistance to scaling, nickel is the most suitable element for use. It increases strength through its hardening effect in the ferrite phase and has positive effects on toughness. It is frequently used to increase strength and hardness in low-alloy steels [10-11].

AISI 4140 steel has one of the most widespread areas of use among low-alloy Cr-Mo carburizing steels and is known as chromium-molybdenum steel. When AISI 4140 steel is compared with steels in the same group, it has moderate hardenability; however, its strength and toughness are better than those of the others. Its areas of use include automobile and aircraft manufacturing, crankshafts, axle shafts and housings, splined shafts and similar parts with high ductility, as well as parts such as gears and tires [3].

Powder metallurgy is the process of producing metal powders and combining these powders through mechanical and thermal effects to form parts. Today, the production of parts by the powder metallurgy method is widely used and is increasingly becoming an alternative to conventional manufacturing methods. Powder iron-based materials produced by the powder metallurgy (P/M) method are widely used in industry. PM and particulate material processing, as in casting, allow the production of net-shape parts. The economical production of high-quality and complex parts makes powder metallurgy attractive. This method allows pores or phases to be placed in the desired locations to create a usable product. PM enables high-volume production through cavities that allow the

same product to be reproduced repeatedly. With these features, PM eliminates present-day concerns such as efficiency, energy, and raw materials. As a result, the field of PM is continuously developing and replacing conventional metal-forming operations. Powder metallurgy is used in many fields, particularly in the automotive industry. Its application areas include tungsten lamp filaments, gears, orthopedic devices, self-lubricating bearings, electrical contacts, office machine parts, high-temperature filters, aircraft brake pads, jet engine parts, welding electrodes, catalysts, soldering tools, high-temperature filters, nuclear power fuel elements, circuit boards, and dentistry [12-14].

In this study, AISI 4140 alloy steel was obtained as a powder mixture with the desired compositions by adding chromium and nickel elements at different ratios into an iron matrix using the powder metallurgy method. The powders, mixed for 1 hour in a three-axis mixer without balls, were unidirectionally compacted at room temperature under a pressing pressure of 750 MPa and then sintered in an argon atmosphere in an atmosphere-controlled tube furnace, thereby producing alloy steel. The distribution of phases in the produced alloy steels was determined by optical microscopy; the shape, distribution, and type of precipitates were analyzed using SEM and EDS. After the microstructural analysis, tensile and hardness tests were applied to powder metal AISI 4140 alloy steel specimens with different chemical compositions prepared in tensile specimen dimensions. The percentage elongation, yield and tensile strengths, and hardness values of the specimens were explained depending on the microstructural changes. In addition, the fracture surface images obtained from the fractured tensile specimens were examined using SEM, and the fracture type was determined.

2. EXPERIMENTAL METHOD

In the experimental study, the process steps followed were conventionally carried out as mixing, pressing, sintering, and characterization processes. The properties of the powders required for alloy steel production and the names of the supplier companies are given in Table 1.

Table I. Powders and Their Properties

	Elemental Powders	**Powder Size (µm)**	**Purity Value (%)**	**Supplier Company**
1	Iron	<150	99,9	Sintek
2	Carbon	10-20	96,5	Sintek
3	Copper	<75	99	Aldrich
4	Nikel	<150	99,9	Aldrich
5	Molybdenum	<150	99,9	Aldrich
6	Aluminum	<75	93	Aldrich
7	Chromium	<45	99	Aldrich

The powders specified in Table 1 were mixed in the chemical compositions given in Table 2, and AISI 4140 steel containing different amounts of Cr and Ni was produced. Before the mixing process, the powders were weighed according to the ratios of the chemical composition given in Table 2 using a RADWAG AS-60-220 C/2 precision balance with an accuracy of 1/10000. The weighed powders were mixed without balls for 1 hour using a Turbula three-axis mixer.

Table II. Chemical Compositions of Alloyed PM Steels

Component	Graphite (wt.%)	Mo (wt.%)	Cr (wt.%)	Cu (wt.%)	Al (wt.%)	Ni (wt.%)	Iron (wt.%)
AISI 4140	0,55	0,25	1	0,25	0,025	0.075	Balance
AISI 4140-3Cr	0,55	0,25	3	0,25	0,025	0.075	Balance
AISI 4140-3Cr-3Ni	0,55	0,25	3	0,25	0,025	3	Balance

The prepared powders were pressed in a Hidroliksan brand press in the form of tensile specimens at a pressing pressure of 750 MPa. The tensile test specimen dimensions were consolidated by unidirectional compaction using a die manufactured according to ASTM (E8M) powder metal material standards.

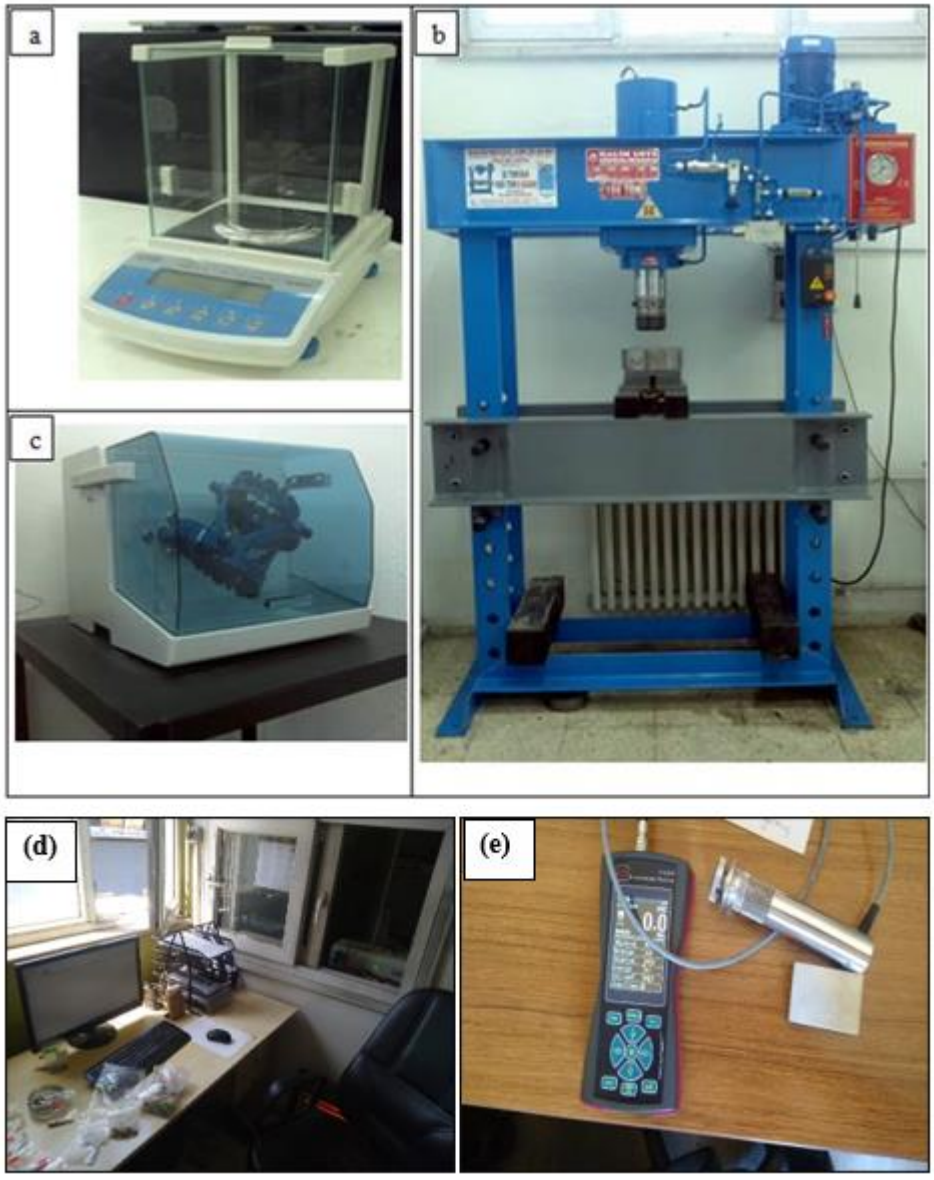


Figure 1. Equipment used for the experimental study: a) precision balance, b) hydraulic press, c) Turbula device, d) spectral analysis device, e) hardness testing device

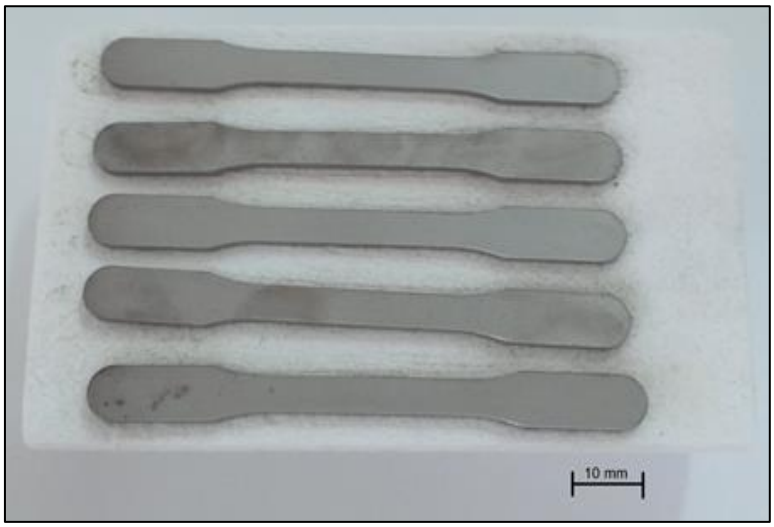


Figure 2. Image of the tensile specimens after pressing.

The sintering process was carried out in an argon atmosphere using a Protherm PTF 16/75/610 atmosphere-controlled tube furnace with a maximum operating temperature of 1600 °C. The specimens with the compositions specified in Table 2 were heated to the sintering temperature of 1400 °C at a rate of 5 °C/min. After the temperature reached the sintering temperature, the specimens were held at this temperature for 1 hour and then cooled to room temperature at a rate of 5 °C/min. Figure 3 shows the atmosphere-controlled furnace used during the sintering stage.



Figure 3. Atmosphere-controlled furnace used in the experimental study.

For hardness measurements, the surfaces of the specimens were ground, polished, and etched using a PRESI brand polishing device. They were then made ready for testing. Hardness measurements of the specimens with prepared surfaces were carried out using a SHIMADZU brand hardness testing device. The hardness measurements were performed by applying an HV0.5 (0.5 kg) load. The hardness value was determined by taking the average of five hardness measurements from each specimen.

The specimens were subjected to a tensile test at a tensile speed of 1 mm/min until fracture. After each test, stress–% strain diagrams were obtained. From these diagrams, the yield strength (0.2%), tensile strength, and % elongation values of the specimens were calculated, and the differences in mechanical properties resulting from the change in alloy content were determined.

Microstructural examinations were carried out using a Nikon brand optical microscope by taking images from different regions of each specimen. SEM examinations were carried out using a Zeiss brand SEM device. In this study, an optical microscope was used to examine the microstructure of specimens sintered in an argon atmosphere. Microalloyed sintered specimens with different compositions were ground using a polishing device with 320, 600, 800, 1000, 1200, and 1500 mesh waterproof abrasive papers, respectively, until the surface irregularities were eliminated. These surfaces were polished using 1, 3, and 6 µm diamond paste abrasives and prepared for etching.

A Nital solution was prepared for the specimens ready for etching by mixing 2% nitric acid into methanol. The etching process was carried out by immersing the specimens in the Nital solution and holding them for 5–8 seconds. The etched surfaces were cleaned with alcohol, dried, and then prepared for examination under the optical microscope. The density measurements of the specimens were carried out using a RADWAG AS density measurement kit on a RADWAG AS-60-220 C/2 precision balance according to the Archimedes principle.

3. EXPERIMENTAL RESULTS AND DISCUSSION MICROSTRUCTURAL RESULTS AND EVALUATION

The microstructure images of the PM steel specimens sintered at 1400 °C in an argon atmosphere are given in Figure 4. When the AISI 4140 steel produced by powder metallurgy was examined, it was observed that the structure consisted of ferrite and pearlite, similar to commercially available steel; however, the pearlitic structure was not homogeneous and was distributed in groups. With the combined addition of Cr and Ni to AISI 4140 steel, it is thought that bainite, martensite, and retained austenite phases were formed.

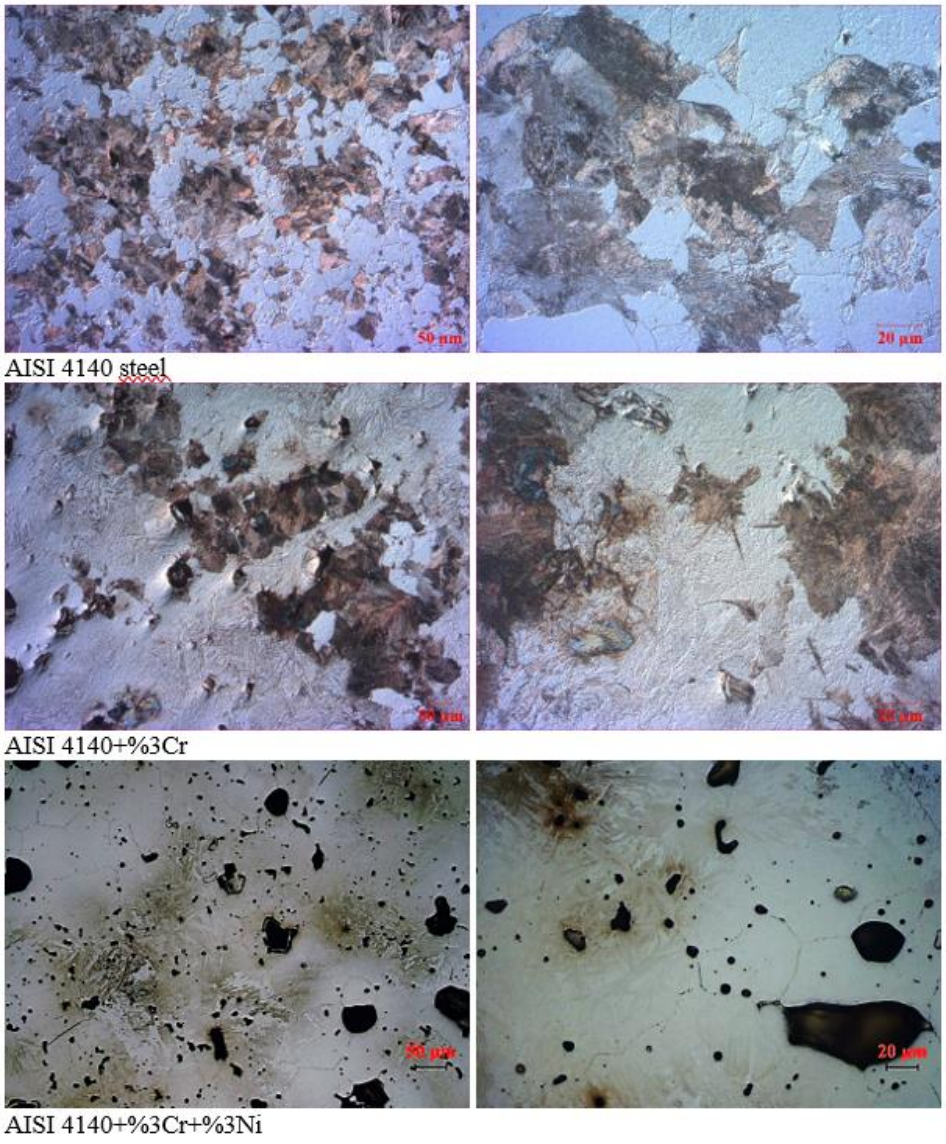


Figure 4. Microstructure images of cold-pressed AISI 4140 PM steels with different chromium, molybdenum, and nickel contents, sintered at 1400 °C in an argon atmosphere.

As seen in Table 3, the theoretical density before sintering, the density after the sintering process, and the amount of porosity were calculated. It is also observed that, as the alloy content in powder metal steels increases, the amount of porosity generally increases. During sintering, the powder particles fused together. After sintering, the density of the specimens naturally increased. In

addition, when Table 5.2 is examined, with the change in the pressing technique, a general increase in density values and a decrease in the amount of porosity were observed with warm and hot pressing. In general, these changes positively affected the mechanical properties.

Table III. Density and % porosity of PM steel specimens sintered at 1400 °C.

Chemical Composition	Theoretical Density (g/cm³)	Density After Sintering (g/cm³)	Density (%)	Porosity (%)
AISI 4140	7,8306	7,6201	97,31	2,69
AISI 4140+3Cr	7,8162	7,2436	92,67	7,33
AISI 4140 + 3 Cr+3 Ni	7,8463	7,2737	92,70	7,30

4. MECHANICAL TEST RESULTS AND EVALUATION

The PM steel specimens (AISI 4140, AISI 4140+3Cr, AISI 4140 3Cr+3Ni) were sintered at 1400 °C and then fractured by applying a tensile speed of 1 mm/min. The tensile graphs obtained from specimens with different alloy ratios are shown in Figure 5. In addition, the tensile strength and % elongation values of the PM steel specimens are given in Table 3.

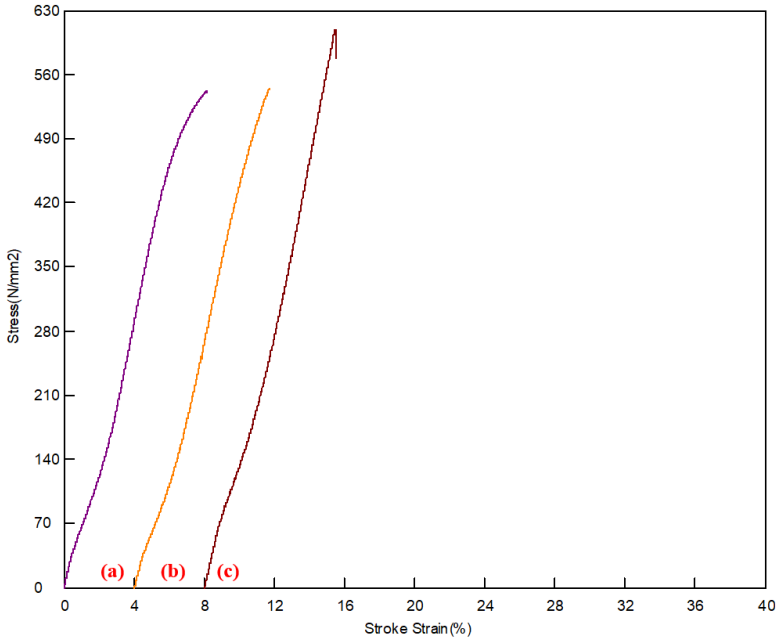


Figure 5. Effect of alloying elements on AISI 4140 steel: a) AISI 4140, b) AISI 4140+3Cr, c) AISI 4140+3Cr+3Ni.

Table IV. Tensile strength (UTS), % elongation, and hardness values of AISI 4140 steel with alloying elements.

Components	Max. Tensile Strength (N/mm^2)	Max. Elongation (%)	Hardness (HV 0.5)
AISI 4140	543	8,1	118
AISI 4140+3Cr	547	7,7	197
AISI 4140 + 3 Cr+3 Ni	610	7,4	386

Similarly, the addition of Cr and Ni elements separately or together to AISI 4140 steel resulted in an increase in tensile strength. However, the % elongation values decreased with the addition of alloying elements [3,15-19]. The hardness values are directly proportional to the tensile strengths. Indeed, Özdemir et al. and Gündüz et al. produced PM steels by adding microalloying elements such as Nb, V, and Ti. When the results they obtained were examined, an increase in the yield strength, tensile strength, and hardness of the materials produced with the addition of microalloying elements, and a decrease in grain size were observed [20-21].

They stated that the reason for this was that precipitates formed by microalloying elements such as NbC(N), VC(N), and AlN during and after sintering inhibited the growth of austenite grains. It was also stated that these precipitates caused an increase in strength through precipitation hardening, dispersion hardening, and grain-size refinement mechanisms. They stated that the reason for this was that precipitates formed by microalloying elements such as NbC(N), VC(N), and AlN during and after sintering inhibited the growth of austenite grains. It was also stated that these precipitates caused an increase in strength through precipitation hardening, dispersion hardening, and grain-size refinement mechanisms. In this study, it is thought that the formation of precipitates, grain-size refinement, and increase in the amount of pearlite with the addition of Cr and Ni, as well as the formation of hard phases such as bainite and martensite in the structure, caused an increase in tensile strength and hardness values [22-27].

The effect of alloying elements in solution on the recrystallization of austenite is very weak. The prevention of grain boundary movement by precipitated particles is much greater than the effect of dissolved atoms [28].

Fracture surface images of the PM steel specimen sintered at 1400°C after the tensile test were taken at X250. When the SEM images of the specimens with AISI 4140 steel composition containing different amounts of Cr and Ni were examined (Figure 6), it was seen that the fracture surfaces exhibited completely partially ductile (honeycomb structure) and partially brittle (cleavage planes)

behavior. It was clearly observed that pores were present on all of the fracture surfaces. This indicates that fracture occurred by the coalescence and propagation of microvoids. However, it was observed that cleavage planes, which are an indication of brittle fracture, were the most in the AISI 4140 alloy steel specimen containing 3 wt.% Cr, moderate in the AISI 4140 alloy steel specimen containing Cr-Ni, and the least in the AISI 4140 alloy steel specimen not containing Cr-Ni. In addition, large voids were observed in the produced PM steel specimens. The presence of these voids shows that single and multiple precipitates such as AlN, MoC(N), CrC(N), and CrMoAlC(N) broke away from the surface during the tensile test. In their study, Shanmugasundaram and Chandramouli [28] observed the formation of such large voids on the fracture surfaces of PM steel containing Cr, Ni, and Mo and attributed this to the separation of carbides, nitrides, and carbonitrides from the surface during the tensile test. As a result of the tensile test, with the increase in the amount of Mo, Cr, and Ni, an increase in yield and tensile strength and a decrease in % elongation were observed. The values obtained as a result of the tensile test are consistent with the fracture surface images [29-30].

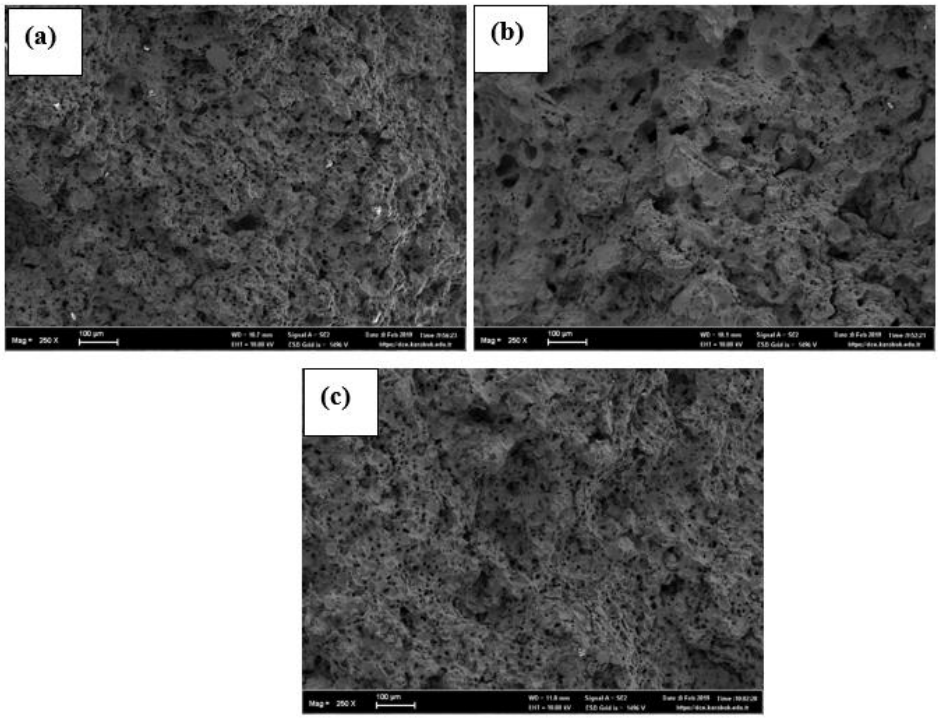


Figure 6. Fracture surface images of specimens with AISI 4140, AISI 4140-3Cr, and AISI 4140-3Cr-3Ni compositions sintered at 1400°C (a- X250; b- X500).

5. GENERAL RESULTS

AISI 4140-Cr-Ni powder metal compositions were produced by cold pressing and sintering at 1400°C in an argon atmosphere. The results obtained from these studies are given below.

1- AISI 4140 carburizing steels can be produced by the powder metallurgy method. Solid-solution hardening and precipitation hardening occurring during sintering or during cooling after sintering increase the strength of the steel.
2- As a result of nickel addition, it was observed that the amount of ferrite increased and the amount of pearlite decreased. When the necessary literature studies were reviewed, it was found that the carbon content in pearlite partially decreased, and that the amount of pearlite in the microstructure increased while the amount of ferrite decreased.
3- In general, it was observed that, up to a certain level, tensile and yield strength increased and percentage elongation decreased with increasing molybdenum and nickel content. The increase in strength was attributed to the increase in the amount of pearlite in the microstructure caused by nickel, as well as to the bainite and martensite phases formed in the structure.
4- As a result of the studies, it was observed that the porosity ratio of the powder metal specimens increased. This result was supported by information in the literature indicating that porosity increases as the amount of alloying elements increases.
5- AISI 4140 PM steels with different Cr and Ni additions were produced by cold, warm, and hot pressing, followed by sintering at 1400 °C in an argon atmosphere. The results listed below were obtained from this study. It was observed that the post-sintering densities of the PM steels were generally around 93%.
6- Alaşım 6- It was observed that the mechanical properties of steels with added alloying elements were superior to those of PM steels without alloying element additions. This is due to the strong carbide-forming properties of the alloying elements.

Acknowledgments

Burak Ayvacı completed this research as part of his master dissertation at Karabuk University in Karabuk, Turkey. This work was supported by Scientific Research Projects Coordination Unit of Karabük University (Karabük, Turkey). Project Number: KBÜ-BAP18YL-017.

Referances

1- Erden, M. A. (2017). The effect of the sintering temperature and addition of niobium and vanadium on the microstructure and mechanical properties of microalloyed PM steels. *Metals*, *7*(9), 329. https://doi.org/10.3390/met7090329

2- Demirtaş, H., & Erden, M. A. (2019). The effect of Cr and Ni addition on mechanical properties of plain carbon steel. *Düzce Univ J Sci Technol*, *7*, 1217-1223.

3- Elkilani, R. H. R., Çuğ, H., Erden, M. A., Abushrenta, H., Albahlol, O., & Cicek, B. (2025). Enhancement of tribological characteristics for Fe-0.55C PM steel via addition of Mo-Ni under different deformation ratios. *Journal of Materials Engineering and Performance*, *34*(11), 10068. https://doi.org/10.1007/s11665-024-10475-w

4- Ulutan, M. (2007). Investigation of the mechanical behavior of AISI 4140 steel after surface hardening and coating methods. *Eskişehir Osmangazi University Institute of Science*, *22*(3), 325–330.

5- Erden, M. A., Demirtaş, H., & Oleiwi, F. H. (2024). Effect of Cr limits on microstructure and mechanical properties of P/M 316L austenitic steel. *Science of Sintering*, *56*, 79–87.

6- Akkaş, M., & Islak, S. (2019). Microstructure, wear and corrosion properties of NiB-TiC composite materials produced by powder metallurgy method. *Science of Sintering*, *51*, 327–338. https://doi.org/10.2298/SOS1903327A

7- Albahlol, O. A. A., Elkilani, R., Çuğ, H., Erden, M. A., Özmen, R., & Esen, I. (2023). Investigation of microstructure and mechanical properties of layered material produced by adding Al2O3 to 316L stainless steel. *Metals*, *13*(7), 1226. https://doi.org/10.3390/met13071226

8- Elitas, M., Güldibi, A. S., & Erden, M. A. (2025). Microstructure and mechanical properties of matching and non-matching resistance spot welds of DP450 and DP800 steel. *Materials Testing*, *67*(11), 1882–1896. https://doi.org/10.1515/mt-2025-0238

9- Bilir, H., Akkaş, M., & Vurdu, C. D. (2025). Powder metallurgy-based production of high-entropy alloys: Structural and functional effects of Si addition. *Technological Applied Sciences*, *20*(2). https://doi.org/10.12739/NWSA.2025.20.2.2A0203

10- Erden, M. A., Uzun, F. G., Akgün, M., & Gökçe, H. (2023). Influence of Ti and Nb addition on the microstructure, mechanical, and machinability properties of 316L stainless steel fabricated by powder metallurgy. *Materials Testing*, *65*(8), 1237–1253.

11- Ertenli, M. F., Erdal, E., Buyukkaragoz, A., Kalkan, I., Aksoylu, C., & Özkılıç, Y. O. (2023). Lateral torsional buckling of doubly-symmetric steel cellular I-beams. *Steel and Composite Structures*, *46*(5), 709–718. https://doi.org/10.12989/scs.2023.46.5.709

12- Erden, M. A., Gündüz, S., Karabulut, H., & Türkmen, M. (2016). Effect of vanadium addition on the microstructure and mechanical properties of low carbon micro-alloyed powder metallurgy steels. Materials Testing, 58(5), 433–437. https://doi.org/10.3139/120.110875

13- Ertenli, M. F., Kalkan, I., & Buyukkaragoz, A. (2021). Gövde buruşmalarının elastik olmayan yanal burkulma sınır uzunluğuna etkisi. Politeknik Dergisi, 24(1), 347–354. https://doi.org/10.2339/politeknik.821093

14- Kinaci, B. F., Erden, M. A., Çuğ, H., Özarpa, C., & Çiçek, B. (2025). Effect of sinter temperature and thermochemical coating on mechanical properties of Ti 6 Al 4 V produced by powder metallurgy. *Journal of Molecular & Engineering Materials*, *13*(3), 18539420. https://doi.org/10.1142/S2251237325500054

15- Erden, M. A., & Ayvacı, B. (2019). The effect on mechanical properties of pressing technique in PM steels. Acta Physica Polonica A, 135(5), 1078–1080.

16- Fadel, A., Glisic, D., Radovicy, N., & Drobnjak, D. (2012). *Journal of Materials Science & Technology*, *28*, 1053.

17- Junhua, K., Lin, Z., Bin, G., Pinghe, L., Aihua, W., & Changsheng, X. (2004). *Materials & Design*, *25*, 723.

18- Li, W., Xu, L., Qiao, L., & Li, J. (2017). *Applied Surface Science*, *42*, 32.

19- Lv, L., Fu, L., Ahmad, S., & Shan, A. (2017). *Materials Science and Engineering: A*, *704*, 469.

20- Özdemirler, D., Gündüz, S., & Erden, M. A. (2017). Influence of NbC Addition on the Sintering Behaviour of Medium Carbon PM Steels. Metals, 7(4), 121. https://doi.org/10.3390/met7040121

21- Gündüz, S., Erden, M. A., Karabulut, H., & Türkmen, M. (2016). Effect of the addition of nioibium and aluminium on the microstructures and mechanical properties of microalloyed PM steels. Materiali in Tehnologije, 50(5), 641–648. https://doi.org/10.17222/mit.2015.248

22- Elkilani, R. H. R. (2024). Effects of hot rolling on microstructures, wear and corrosion resistance of Mo-Ni-W p/m alloyed steels. Journal of Mining and Metallurgy, Section B: Metallurgy, 60(3), 367. https://doi.org/10.2298/JMMB240404030E

23- Erden, M. A. (2020). The effect of sintering time on tensile strength of NB-V microalloyed powder metallurgy steels. *Technological Applied Sciences*, *15*(1), 15–22. https://doi.org/10.12739/NWSA.2020.15.1.2A0180

24- Erden, M. A., Gündüz, S., Karabulut, H., & Türkmen, M. (2017). Wear behaviour of sintered steels obtained using powder metallurgy method. *Mechanics*, *23*(4), 574–580. https://doi.org/10.5755/j01.mech.23.4.18982

25- Erden, M. A., Tasliyan, M., & Akgul, Y. (2021). Effect of TiC, TiN, and TiCN on microstructural, mechanical and tribological properties of PM steels. *Science of Sintering*, *53*, 497–508. https://doi.org/10.2298/SOS2104497E

26- Erhaime, M. E. E., Cug, H., Erden, M. A., Akgul, Y., Incesu, A., & Cicek, B. (2025). Synergetic effect of Nb–V on mechanical, tribological and corrosion properties of AISI 603 steel produced via powder metallurgy. *Journal of Molecular & Engineering Materials*, *13*(2), 2550002. https://doi.org/10.1142/S2251237325500029

27- Karabulut, H., Türkmen, M., Erden, M. A., & Gündüz, S. (2016). Effect of different current values on microstructure and mechanical properties of microalloyed steels joined by the submerged arc welding method. *Metals*, *6*(11), 281. https://doi.org/10.3390/met6110281

28- Shanmugasundaram, D., & Chandramouli, R. (2009). Tensile and impact behaviour of sinter-forged Cr, Ni and Mo alloyed PM steels. *Materials & Design*, *30*(9), 3444–3449.

29- Kostryzhev, A.G.; Al Shahrani, A.; Zhu, C.; Cairney, J.M.; Ringer, S.P.; Killmore, C.R.; Pereloma, E.V. Effect of niobium clustering and precipitation on strength of an NbTi-microalloyed ferritic steel. *Mater. Sci. Eng. A* **2014**, *607*, 226–235.

30- Tracey, V. (1992). Nickel sintered steels-Developments, status and prospects. *Metal Powder Report*, *47*(11), 49.

Chapter 3

Seeing What Nano YOLO Detectors See: Military Aircraft Recognition

Ertuğrul DOĞRULUK[1]

1. INTRODUCTION

Satellite and aerial imagery allow analysts to follow activity at airfields over large areas, and recognising the aircraft parked there is one of the most common interpretation tasks. Deep convolutional detectors have become the standard tool for object detection in optical remote sensing [1], and single-stage You Only Look Once (YOLO) detectors [2] are popular because they are fast and easy to deploy. Military aircraft recognition is a demanding case, however: an aircraft may cover only a few dozen pixels, aircraft are often parked wingtip to wingtip, and several types share almost the same planform.

MAR20 [3] has become the common benchmark for this problem. It contains 3,842 Google Earth images of 60 military airfields with 22,341 aircraft of 20 types. Studies on MAR20 usually propose new modules and report mean average precision (mAP) [4]–[6], but they rarely show many detection results, so it is difficult to judge what a detector actually gets right or wrong on an apron.

This short study takes the opposite approach. It trains five nano detectors of the Ultralytics family [7] under one configuration, reports their test accuracy briefly, and then devotes most of its space to annotated detection examples: dense parking rows, mixed aprons, side-by-side comparisons of the five models and typical failure cases. The aim is to give a clear, visual baseline of what small, off-the-shelf detectors can do on MAR20.

2. MATERIALS AND METHODS

2.1. Dataset

MAR20 images measure about 800 × 800 pixels and are annotated with horizontal and oriented boxes; the horizontal boxes were used here. The 20 types (A1–A20) are the SU-35, C-130, C-17, C-5, F-16, TU-160, E-3, B-52, P-3C, B-1B, E-8, TU-22, F-15, KC-135, F-22, FA-18, TU-95, KC-10, SU-34 and SU-24, and the type names are used throughout this paper. The 3,842 images were pooled and divided 7:2:1 into training, validation and test subsets, stratified by the most frequent type in each image

[1] Assit. Prof. Dr. Department of Software Engineering, Istiklal University of Science and Technology, Kahramanmaraş, Türkiye, ertugrul.dogruluk@istiklal.edu.tr, ORCID: 0000-0002-7285-414X

so that every type appears in every subset (Table 1). Figure 1 shows ground-truth examples that together cover all 20 types. Because this partition differs from the official one, the scores below should not be compared directly with results obtained on the official test list.

Table I. Partition of MAR20 used in this study

Subset	Images	Aircraft	Aircraft per image
Training	2,691	15,629	5.8
Validation	770	4,471	5.8
Test	381	2,241	5.9
Total	3,842	22,341	5.8



Figure 1. Ground-truth annotations of nine MAR20 test images that together contain all 20 aircraft types: (a) tankers and bombers, (b) a mixed apron with E-3, E-8, KC-135 and C-130 aircraft, (c) Sukhoi fighters, (d) Tupolev bombers, (e) C-130, F-15 and F-16 aircraft, (f) transports and P-3C patrol aircraft, (g) P-3C and FA-18 aircraft, (h) C-17 and C-5 transports and (i) F-22 and F-15 fighters

2.2. Detectors and training

The five detectors are the nano versions of YOLOv5nu, YOLOv8n, YOLO11n, YOLO12n and YOLO26n in Ultralytics 8.4.14 [7], each initialised from COCO-pretrained weights and given a 20-class head. They differ mainly in their building blocks: YOLOv8n uses C2f blocks, YOLO11n adds C3k2 blocks and an attention stage, YOLO12n is built around area attention, and YOLO26n predicts without non-maximum suppression (NMS). All models were trained with the same settings: 640-pixel input, batch size 16, 200 epochs, automatic optimizer selection (AdamW), seed 0, mosaic augmentation switched off for the last ten epochs, and no MixUp, CutMix or rotation. Training ran on a single NVIDIA GeForce RTX 4060 GPU. For each model the checkpoint with the best validation mAP@0.5:0.95 was evaluated once on the test subset.

2.3. Evaluation and visualization

Test accuracy is reported as precision, recall, mAP@0.5 and mAP@0.5:0.95 as computed by Ultralytics. For the figures, detections with a confidence of at least 0.25 were matched to the ground truth in order of decreasing confidence, using an intersection over union (IoU) of at least 0.5 regardless of type. Each detection was then counted as correct (matched and correct type), wrong type (matched but wrong type) or background (not matched), and every unmatched ground-truth aircraft as missed. In the figures, correct detections are drawn in the colour of their type with the predicted type and confidence, wrong-type detections in solid red, background detections in dashed orange and missed aircraft in dashed white.

3. RESULTS AND DISCUSSION

3.1. Overall accuracy

Table 2 shows that the five detectors reach almost the same accuracy. On the 381 test images, mAP@0.5 lies between 96.96% and 97.29% and mAP@0.5:0.95 between 79.77% and 80.45%. YOLO12n scores highest on both measures, but its lead over the other models is less than 0.7 points and it needs the longest training time. At a confidence of 0.25, the detectors give the correct type for 2,134 to 2,141 of the 2,241 test aircraft and miss only 5 to 19 aircraft altogether. Most of the remaining errors are therefore wrong types or background detections, not missed aircraft.

Table II. Test results of the five nano detectors (381 images, 2,241 aircraft)

Model	Params (M)	P (%)	R (%)	mAP@0.5 (%)	mAP@0.5:0.95 (%)	Corr.	Wrong	Bkg.	Miss	Train (min)
YOLOv5nu	2.51	95.17	94.51	97.19	79.78	2,136	100	90	5	74.5
YOLOv8n	3.02	96.04	93.63	97.21	79.77	2,134	98	92	9	77.1
YOLO11n	2.59	96.24	94.36	97.06	80.04	2,141	89	87	11	79.7
YOLO12n	2.57	95.50	95.00	97.29	80.45	2,140	96	73	5	110.7
YOLO26n	2.51	95.42	93.60	96.96	80.28	2,140	82	105	19	99.0

P: precision; R: recall. Corr. (correct type), Wrong (wrong type), Bkg. (background) and Miss (missed aircraft) are counts at a confidence of 0.25 with class-agnostic matching at IoU 0.5. Training time covers 200 epochs including validation

3.2. Detection examples

Figure 2 shows YOLO12n detections on nine of the densest test scenes, with 15 to 38 aircraft each. In all nine, every aircraft is found and given the correct type, including long rows of KC-135 and C-130 aircraft in a storage area (Fig. 2a, b), diagonally parked FA-18 fighters (Fig. 2c), small F-16 and SU-24 fighters next to hangars and taxiways (Fig. 2f, g) and C-17 transports on separate parking pads (Fig. 2i). The only extra boxes are a few background detections, mostly on aircraft cut by the image border. Confidence scores of correct detections are typically between 0.85 and 0.95.



Figure 2. YOLO12n detections on nine dense test scenes at a confidence of 0.25. Panel titles give the number of correctly typed aircraft out of all annotated aircraft; dashed orange boxes mark background detections

3.3. Comparison of the five detectors

Figure 3 compares the five models on four harder scenes. On an apron with 17 FA-18 fighters (Fig. 3a), four models type every aircraft correctly, while YOLOv5nu labels two of them as F-15 and misses one. In two Sukhoi scenes (Fig. 3b, c), the models disagree on several aircraft and swap the SU-34, SU-35 and SU-24 labels, which have similar swept-wing planforms at this resolution. The mixed fighter scene in Fig. 3d is the hardest: YOLOv8n types all ten aircraft correctly, whereas YOLO12n calls most F-16s F-15s. These examples show that the small differences in mAP hide clear model-to-model differences on individual scenes, and that no single model is best on every scene.

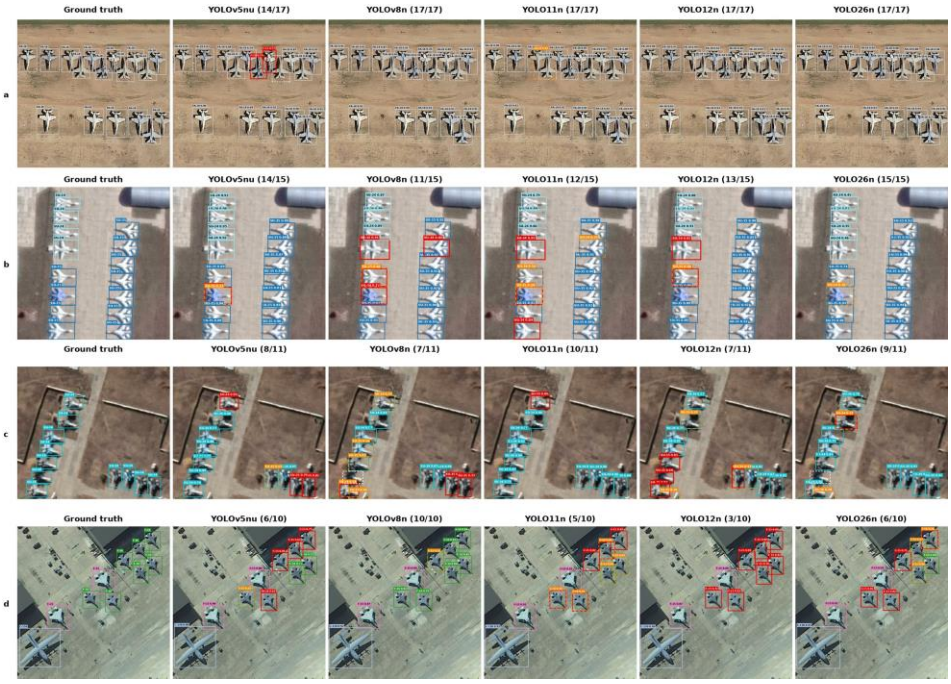


Figure 3. Ground truth and predictions of the five detectors on four test scenes: (a) FA-18 fighters, (b) SU-24 and SU-35 fighters, (c) SU-34 fighters and (d) F-15 and F-16 fighters with a C-130. Numbers in brackets give correctly typed aircraft out of all aircraft; red: wrong type, dashed orange: background, dashed white: missed

3.4. Typical errors

Across the whole test subset, the most frequent YOLO12n confusions are SU-34 predicted as SU-35 (16 cases), F-15 as SU-24 (14), F-16 as F-15 (13), F-22 as F-15 (7) and E-8 and KC-135 in both directions (6 each). Figure 4 shows four examples. In Fig. 4a, two rows of F-15 fighters on a reddish surface are all found but labelled SU-24 with confidences of 0.64 to 0.90. In Fig. 4b, four large four-engine jets annotated as KC-135 are predicted as E-8 with confidences of about 0.95, a type with a very similar four-engine airframe. In Fig. 4c and 4d, F-16 fighters are labelled F-15 and FA-18 fighters F-16. In every case the box itself is well placed; only the type is wrong, and often with high confidence. Small fighters dominate these errors, which agrees with earlier MAR20 studies that also found the F-15, F-16, F-22 and E-8 among the hardest types [4]–[6], [8].

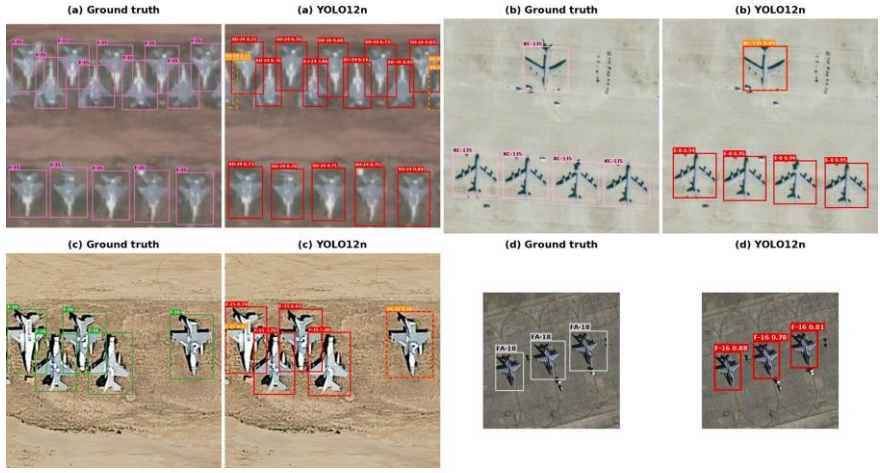


Figure 4. Typical type confusions of YOLO12n, ground truth (left) and prediction (right): (a) F-15 predicted as SU-24, (b) KC-135 predicted as E-8, (c) F-16 predicted as F-15 and (d) FA-18 predicted as F-16. The boxes are correctly placed, but the type is wrong

Figure 5a confirms this picture at the class level. Large aircraft such as the C-5, TU-95, B-52 and TU-160 reach 84–89% AP@0.5:0.95 for most models, whereas the F-15, F-16, F-22 and E-8 stay between about 67% and 77%. The ranking of the five models also changes from type to type, as in the visual comparison. Figure 5b shows that all models learn at a similar pace: validation mAP@0.5:0.95 passes 75% within about 25 epochs and then rises only slowly towards 81%.

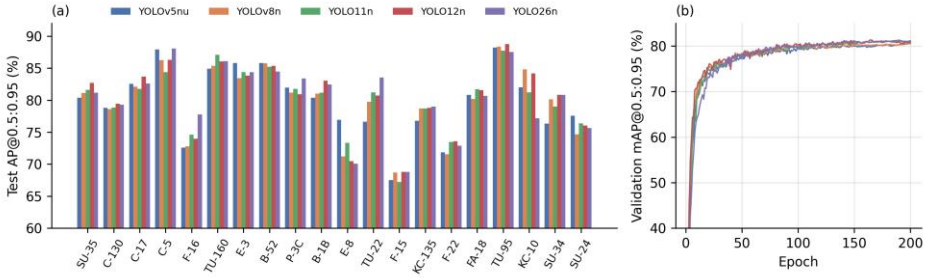


Figure 5. (a) Test AP@0.5:0.95 of each aircraft type for the five detectors. (b) Validation mAP@0.5:0.95 during training

3.5. Limitations

Each model was trained once, so differences of a few tenths of a point may change in another run. The test subset comes from a re-partition of MAR20 rather than the official test list, and because the images were cropped from only 60 airfields, some scene-level overlap between subsets cannot be ruled out. The examples were chosen to illustrate typical behaviour and are not a random sample.

4. CONCLUSION

Five nano YOLO detectors were trained on MAR20 under one shared configuration and examined both numerically and visually. Their accuracy was almost identical, with test mAP@0.5:0.95 between 79.77% and 80.45%, so the choice between them can be made mainly on training and deployment cost. The detection examples showed that all models found nearly every aircraft, even in long, dense parking rows, and that the remaining errors were mostly confident type confusions between similar fighters or between large jets built on the same airframe. Future work will test the models on the official MAR20 split with several training runs and at a higher input resolution, which may help with the smallest fighters.

Acknowledgment

This work was supported by the Istiklal University of Science and Technology Scientific Research Projects Coordination Unit (BAP) under Project Number 2026/2-1.

References

1. K. Li, G. Wan, G. Cheng, L. Meng and J. Han, "Object detection in optical remote sensing images: A survey and a new benchmark," ISPRS J. Photogramm. Remote Sens., vol. 159, pp. 296–307, 2020, doi: 10.1016/j.isprsjprs.2019.11.023.
2. J. Redmon, S. Divvala, R. Girshick and A. Farhadi, "You only look once: Unified, real-time object detection," in Proc. IEEE Conf. Comput. Vis. Pattern Recognit. (CVPR), 2016, pp. 779–788, doi: 10.1109/CVPR.2016.91.
3. W. Yu, G. Cheng, M. Wang, Y. Yao, X. Xie, X. Yao and J. Han, "MAR20: A benchmark for military aircraft recognition in remote sensing images," Natl. Remote Sens. Bull., vol. 27, no. 12, pp. 2688–2696, 2023, doi: 10.11834/jrs.20222139.
4. X. Chen et al., "DET-YOLO: An innovative high-performance model for detecting military aircraft in remote sensing images," IEEE J. Sel. Topics Appl. Earth Observ. Remote Sens., vol. 17, pp. 17753–17771, 2024, doi: 10.1109/JSTARS.2024.3462745.
5. J. Wu, F. Zhao, G. Yao and Z. Jin, "FGA-YOLO: A one-stage and high-precision detector designed for fine-grained aircraft recognition," Neurocomputing, vol. 618, Art. no. 129067, 2025, doi: 10.1016/j.neucom.2024.129067.
6. X. Xu, Z. Chen, X. Zhang and G. Wang, "Context-aware content interaction: Grasp subtle clues for fine-grained aircraft detection," IEEE Trans. Geosci. Remote Sens., vol. 62, Art. no. 5641319, 2024, doi: 10.1109/TGRS.2024.3464851.
7. G. Jocher, J. Qiu and A. Chaurasia, "Ultralytics YOLO," version 8.4.14, Ultralytics, 2026, computer software. [Online]. Available: https://github.com/ultralytics/ultralytics
8. T. Shi et al., "Progressive class-aware instance enhancement for aircraft detection in remote sensing imagery," Pattern Recognit., vol. 164, Art. no. 111503, 2025, doi: 10.1016/j.patcog.2025.111503.

Chapter 4

Powder Metallurgy Processing of W-Based Cutting Tools: Impact of Alloy Chemistry on Microstructure and Mechanical Performance

Aboubaker Alferjani H. ALRAJHE[1], Zakaria Ahmad Farag ALDALİMİ[2], Mehmet AKKAŞ[3]

1. INTRODUCTION

Powder metallurgy (PM) is widely adopted for manufacturing high performance tool and structural materials because it enables tight control over composition, microstructure, and final geometry. In contrast to conventional routes such as casting followed by extensive machining or hot, cold working, PM can reduce material waste, improve compositional uniformity, and support near net shape fabrication, thereby lowering processing costs while enhancing repeatability in production [1]. These advantages are especially relevant when the target application demands a carefully engineered microstructural architecture such as controlled porosity, refined grain particle size, and homogeneous distribution of secondary phases—where small compositional changes can lead to large differences in mechanical response [2].

Within advanced manufacturing and machining technologies, W-based cutting tool materials represent a class of systems valued for their resistance to high temperature softening, their capability to sustain mechanical loads during cutting, and their potential to maintain dimensional stability under severe service conditions. Although tungsten is intrinsically associated with high melting temperature and high stiffness, the practical performance of W-based tool bodies and inserts is not determined by tungsten alone. Instead, performance emerges from a combined effect of alloy chemistry, powder processing quality, and consolidation behavior during compaction and sintering. These interrelated factors govern densification kinetics, pore morphology, interfacial bonding, and the continuity of load bearing paths in the consolidated tool material [3–5].

[1] PhD student, Kastamonu University, Graduate Education Institute, Department of Materials Science and Engineering, Kastamonu, 37150, Turkey; aboubakeralferjani@outlook.com, (ORCID: 0009-0003-6708-2178)
[2] PhD student, Kastamonu University, Graduate Education Institute, Department of Materials Science and Engineering, Kastamonu, 37150, Turkey; zakariaaldalimi@outlook.com, (ORCID: 0009-0003-2062-1218)
[3] Assoc. Prof. Dr., Istiklal Science and Technology University, Faculty of Engineering, Architecture and Design, Department of Mechanical Engineering, Kahramanmaraş, 46100, Turkey; mehmetakkas@istiklal.edu.tr, (ORCID: 0000-0002-0359-4743)

A central challenge for PM processing of W-based systems is achieving a microstructure that simultaneously supports high hardness (for wear resistance) and sufficient toughness (to resist cracking and chipping). This balance is strongly influenced by the type and amount of alloying additions, which can modify diffusion activity, promote (or hinder) interparticle neck growth, affect grain, particle coarsening, and alter the stability of microstructural interfaces formed during sintering [6]. For instance, alloying and binder chemistry may improve densification and bonding, but excessive amounts or non uniform distribution can lead to microstructural discontinuities such as binder rich zones, pore clusters, or weak interfaces that compromise mechanical reliability under cyclic and impact like loads encountered in cutting operations [7,8]. In recent years, increasing attention has been directed toward tailoring W-based tool materials through targeted alloying strategies to overcome limitations associated with monolithic compositions, including insufficient damage tolerance, sensitivity to processing defects, or performance loss under aggressive environments (e.g., machining with coolants, humid conditions, or chemically active media). In this context, understanding how alloy chemistry influences powder packing, compaction response, sintering driven densification, and the resulting microstructure–property relationships becomes essential for both academic insight and industrial implementation [9-11].

Accordingly, the present study investigates the manufacturability and consolidation performance of W-based cutting tool materials produced by powder metallurgy. The work is designed to clarify how changes in alloy chemistry affect microstructural evolution (including pore formation and phase distribution) and how these microstructural outcomes translate into mechanical performance indicators relevant to cutting tool applications. Accordingly, the present study investigates the powder-metallurgical processing of W-based tool materials and examines the influence of alloy chemistry on their consolidation behavior, microstructural evolution, and microhardness response. Particular emphasis is placed on establishing process structure property relationships by correlating compositional modifications with porosity development, interparticle bonding, and hardness variation.

2. RESEARCH SIGNIFICANCE

The significance of this study lies in establishing a systematic relationship between alloy chemistry, powder-metallurgical consolidation, microstructural integrity, and hardness response in W-based tool materials. By maintaining constant compaction and sintering conditions while varying composition, the study isolates the influence of alloy chemistry on pore evolution, interparticle bonding, and mechanical response. The resulting process structure property relationships can

contribute to the compositional design of powder metallurgically produced W-based engineering materials.

3. EXPERIMENTAL METHOD-PROCESS; ANALYTICAL STUDY VEYA SUBJECT

To evaluate manufacturability and consolidation behavior, 3 distinct powder blends were prepared using elemental powders with 99.9% purity and a nominal particle size of 325 mesh. A W-based primary composition was selected to form the principal load bearing framework of the cutting tool material, and alloying additions were introduced in different proportions to examine their effect on microstructural evolution and mechanical response. For clarity throughout the manuscript, the produced compositions are denoted as S1–S3, representing the progressive modification of alloy chemistry.

Powders were weighed using a precision balance to ensure accurate compositional control. Mixing was carried out in a three dimensional Turbula mixer for 16 hours to promote uniform dispersion and minimize segregation effects that could lead to local chemistry gradients. Following powder blending, all compositions were uniaxially compacted under a constant pressure of 275 MPa to obtain green compacts with consistent geometry, enabling a more direct comparison of consolidation response across compositions.

Sintering was performed under a controlled argon atmosphere at 1025 °C for 20 minutes, with the protective environment selected to reduce oxidation risk and support stable interparticle bonding. After sintering, specimens underwent standard metallographic preparation (grinding, polishing, and appropriate etching) to reveal internal features for microstructural analysis. The consolidated materials were then evaluated by SEM based characterization, and mechanical performance was assessed through microhardness testing along defined measurement paths to capture potential heterogeneity.

4. FINDINGS AND DISCUSSIONS

4.1. Scanning Electron Microscopy (SEM) Analysis

SEM examinations demonstrated that microstructure is strongly dependent on alloy chemistry and its distribution within the W-based matrix. Across the produced compositions, the micrographs indicated that powder mixing was effective at generating broadly uniform dispersion of the alloying constituents, with SEM supporting the presence of a reasonably homogeneous elemental distribution in most regions. This outcome suggests that the selected mixing protocol can produce consistent starting powder blends, a prerequisite for reliable compaction and sintering behavior (Figures 1–3).

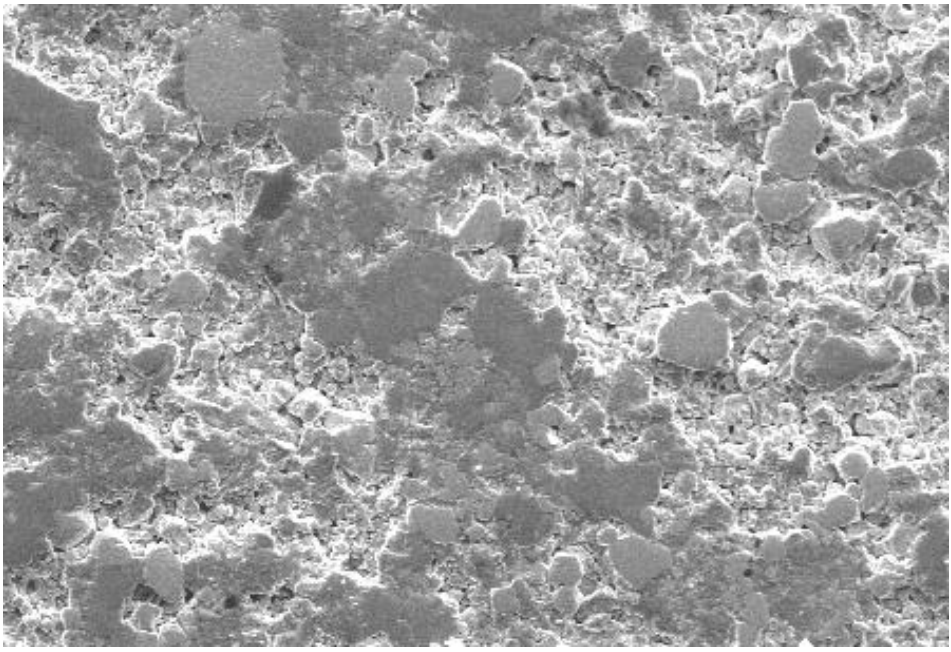


Figure 1. SEM Analysis image of sample number 1

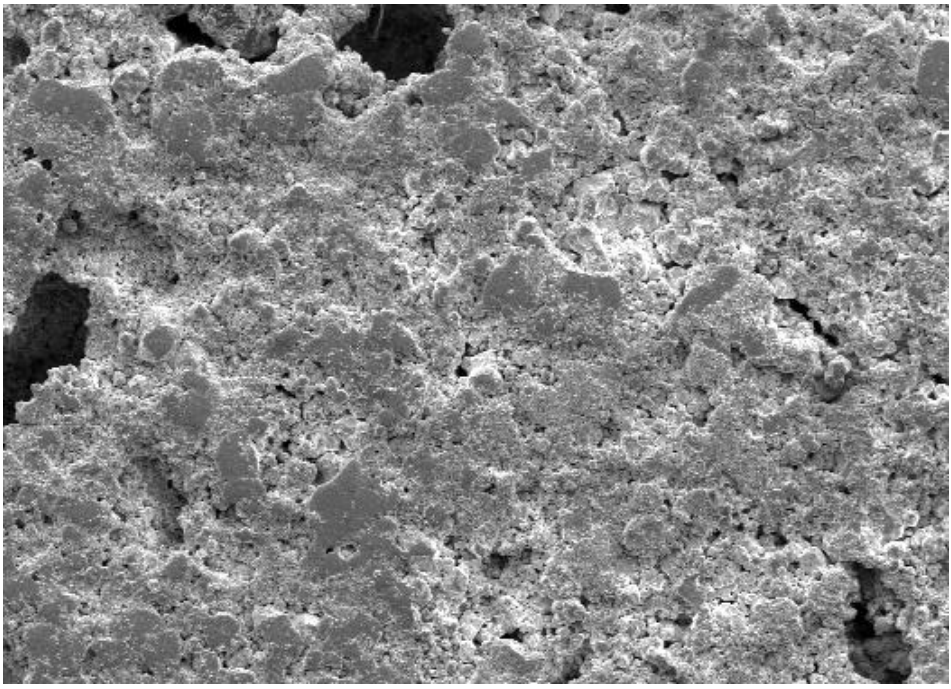


Figure 2. SEM Analysis image of sample number 2

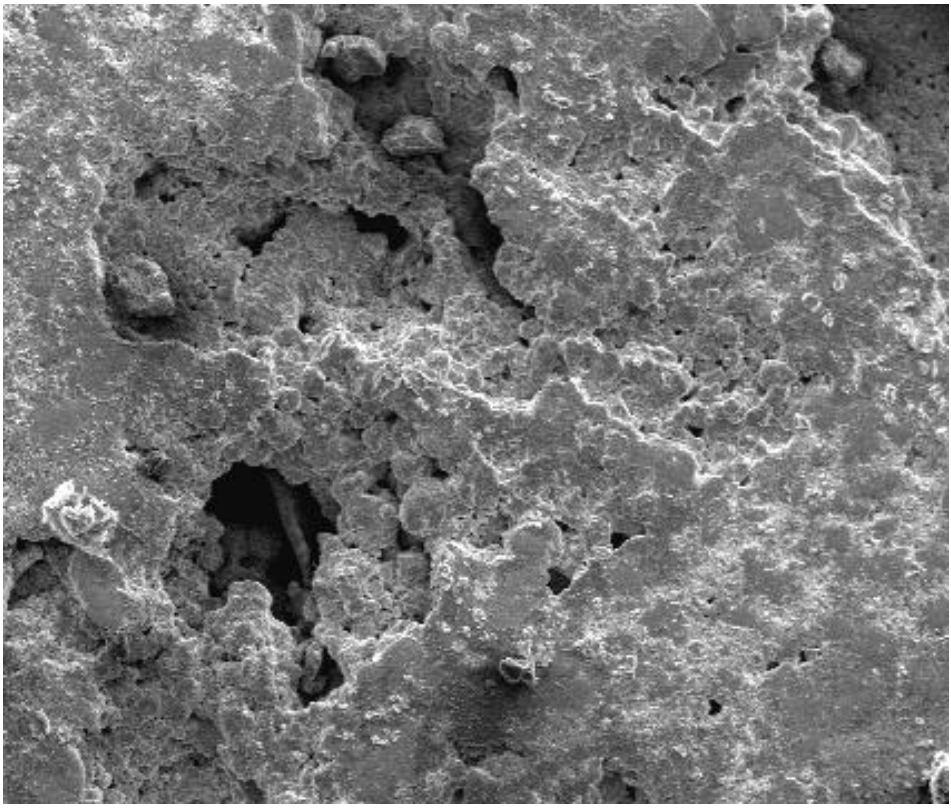


Figure 3. SEM Analysis image of sample number 3

A key observation was that compositional changes altered the evolution of porosity during sintering. Some compositions exhibited more compact microstructural regions with reduced pore connectivity, whereas others showed localized pore clusters and void like defects. This variation can be interpreted as a consequence of alloy chemistry dependent sintering kinetics: alloying additions can either facilitate diffusion and neck growth (improving densification) or, if non ideal in amount, distribution, contribute to heterogeneous shrinkage and defect formation. In addition, the interface quality between the W-based matrix and alloyed regions appeared to vary among S1–S3, implying that interfacial bonding is also sensitive to chemistry and local microstructural arrangement.

Micrographs further suggested that compositions closer to an optimized chemistry range developed more continuous interparticle necks and more compact boundaries, consistent with improved diffusion activity and enhanced sintering efficiency [12–15]. Conversely, the presence of occasional microcrack like discontinuities and voids in specific specimens indicates incomplete densification or local stress accumulation during consolidation, which can

originate from non uniform packing, insufficient diffusion, or local variations in phase distribution. These features are critical for cutting tool reliability because pores and weak interfaces can serve as crack initiation sites under mechanical and thermal cycling. In general, the SEM results confirm that alloy chemistry governs both manufacturability and structural integrity in PM processed W-based cutting tools [16-18].

4.2. Microhardness Response and Mechanical Implications

To evaluate mechanical response in a manner sensitive to local microstructural variations, microhardness measurements were conducted along a defined line on the specimen surface at 100 μm intervals. This approach is particularly relevant for PM manufactured materials, where local differences in porosity, phase distribution, and interface quality can generate spatially varying hardness.

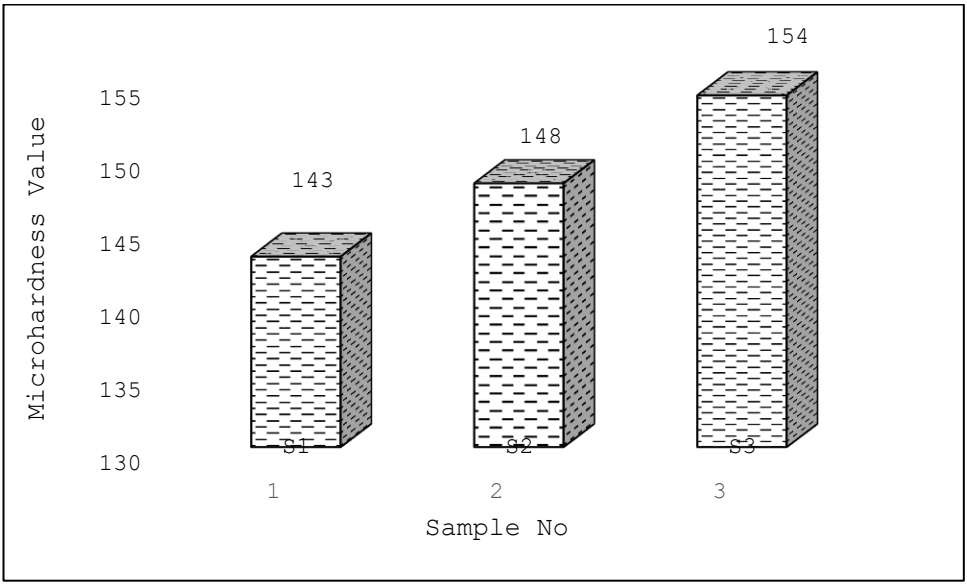


Figure 4. Microhardness value of composite samples

The results revealed a systematic trend in hardness as alloy chemistry was modified. The average hardness of the baseline specimen (S1) was approximately 143 HV, representing the reference response of the W-based matrix under the present consolidation conditions. With the first chemistry modification (S2), hardness increased to approximately 148 HV, suggesting that alloying additions introduced strengthening contributions—potentially through enhanced interparticle bonding, improved load transfer, or the formation of harder microstructural regions. In the subsequent modified composition (S3), hardness

reached approximately 154 HV, indicating further strengthening as the effective fraction or distribution of strengthening constituents increased [19].

From a microstructural viewpoint, this incremental hardening can be rationalized by considering (i) reduced local deformation due to the presence of harder phases, regions, (ii) improved bonding at interfaces that carry load more efficiently, and (iii) a microstructure that limits dislocation motion through refined features and strengthened boundaries [14]. Importantly, hardness improvements should be interpreted together with SEM observations: the most desirable composition is not only the one with the highest hardness, but also the one that achieves this hardness without increasing defect density. In cutting tool applications, excessive brittleness or defect driven crack initiation can negate the benefits of higher hardness [20-24]. Literature comparisons support that alloying strategies can significantly modify hardness and strength in W-based systems, particularly when they alter diffusion behavior and promote a more coherent microstructural network [25]. In the present results, the composition associated with the highest measured hardness can be considered a candidate for an optimal chemistry range under the chosen PM parameters, provided that microstructural integrity remains acceptable. Among the investigated compositions, S3 exhibited the highest microhardness while maintaining comparatively favorable microstructural characteristics.

5. CONCLUSION AND RECOMMENDATIONS

This study demonstrates that alloy chemistry is a decisive parameter controlling the manufacturability, microstructural evolution, and mechanical performance of W-based cutting tool materials produced via powder metallurgy. Under constant compaction and sintering parameters, compositional modifications produced observable differences in pore morphology, microstructural continuity, and defect population. SEM analysis confirmed that some alloy chemistries promote improved densification features and more continuous bonding, whereas others are associated with localized porosity and discontinuities that can reduce structural reliability. Microhardness testing showed a composition dependent strengthening trend, indicating that alloying can enhance mechanical response when coupled with adequate microstructural integrity.

REFERENCES

[1] Suman, V., Maurya, R. S., Debata, M., & Chaira, D. (2025). Effects of Silicon Addition on Physical and Mechanical Properties of W, W–Ni, and W–Ni–Co Alloys Fabricated by Powder Metallurgy. Advanced Engineering Materials, 27(6), 2400831.

[2] Chabak, Y., Efremenko, V., Barma, Y., Petrišinec, I., Efremenko, B., Kromka, F., ... & Kovbasiuk, T. (2025). Enhancing Dry-Sliding Wear Performance of a Powder-Metallurgy-Processed "Metal Matrix–Carbide" Composite via Laser Surface Modification. Eng, 6(11), 313.

[3] Huang, S. G., Liu, C., Liu, B. L., Anwer, Z., & Vleugels, J. (2025). NbC-Ni based cermets: Phase diagrams, microstructure and mechanical properties. International Journal of Refractory Metals and Hard Materials, 128, 107020.

[4] Bilir, H., Akkaş, M., & Vurdu, C. D. (2025). Powder Metallurgy-Based Production Of High-Entropy Alloys: Structural And Functional Effects Of Si Addition. Technological Applied Sciences, 20(2), 38-44.

[5] Ghasali, E., Ebadzadeh, T., Hayati, R., Jie, L., & Orooji, Y. (2026). Effect of microwave sintering on physical and microstructure of Cu-WC composites. Materials Chemistry and Physics, 347, 131459.

[6] Iqbal, Z., Zarif, M., Hussain, M., Hakeem, A. S., Shah, A., Yasir, M., ... & Shafi, H. Z. (2025). Impact of Carbides and BN Addition on the Mechanical and Wear Properties of Pressure-Less-Sintered Novel Tungsten-Iridium Alloys. Journal of Materials Engineering and Performance, 1-17.

[7] Islam, Z., Ahmed, T., Ahmed, B. A., Ogunlakin, N. O., Ahmed, I., Drmosh, Q. A., & Hakeem, A. S. (2025). Enhancement of Co212 superalloy through cBN reinforcement: Insights derived from spark plasma sintering. Journal of Alloys and Compounds, 183747.

[8] Bilir, H., Akkaş, M., & Vurdu, C. D. (2025). Toz Metalurjisi Yöntemi İle Yüksek Entropili Alaşimin Üretimi Ve Karakterizasyonu. Technological Applied Sciences, 20(2), 45-52.

[9] Yang, T., Zhao, L., Wu, W., Chen, P., & Qiu, C. (2025). Effects of Ti+ Al content on the microstructure and mechanical properties of a new nickel-based superalloy fabricated by laser directed energy deposition. Journal of Materials Science, 60(8), 3957-3973.

[10] Han, J., Sung, H., Seol, J. B., Cho, K., Lee, Y., & Choi, H. (2025). Emerging Trends in Additive Manufacturing of Metal Matrix Composites: Opportunities and Obstacles. MetalMat, e70020.

[11] Akkaş, M. (2024). The effect of molten salt on the mechanical properties and microstructure of CuNiSi alloys with reinforced Fe. Science of Sintering, (00), 28-28.

[12] Xue, F., Zhou, H., Wu, N., & Zhang, L. (2025). Carbon-mediated interface structure and mechanical properties in TiB2-WC cermets: From microstructure to performance. International Journal of Refractory Metals and Hard Materials, 129, 107118.

[13] Kumar, R., Antonov, M., Berglund, T., Pampori, T. H., Maurya, H. S., & Viljus, M. (2025). Wear mechanisms of PM-HIP tool steels under low and high-stress abrasion: Role of carbide type and content. Journal of Materials Research and Technology.

[14] Chen, Q., Song, H., Song, X., Li, X., Wang, J., Fu, B., ... & Qu, X. (2025). Fabrication of Nano-Sized Tungsten-Rhenium Alloy Powders via Solution Combustion Synthesis with Hydrogen Reduction and Their Sintering Densification Behavior. Journal of Alloys and Compounds, 183103.

[15] Akkaş, M. (2022). Synthesis and characterization of MoSi2 particle reinforced AlCuMg composites by molten salt shielded method. Türk Doğa ve Fen Dergisi, 11(4), 11-17.

[16] Yue, J. T., Liang, Y. J., Wang, L., & Xue, Y. (2025). Microstructures and high-temperature tensile properties of a Co-Al-W-based superalloy prepared by laser additive manufacturing. Journal of Alloys and Compounds, 1011, 178378.

[17] Ren, R., Niu, B., Liu, Q., Zhang, T., Mei, D., Li, Y., & Li, Q. (2025). Optimization of electrical contact properties and arc erosion resistance of Mo–W–Cu ternary contact materials prepared via hydrogen sintering under DC arc conditions. International Journal of Refractory Metals and Hard Materials, 107469.

[18] Chen, Y., Chen, C., Wang, J., Wang, S., Gong, H., Mao, Y. R., ... & Wu, Y. C. (2025). The effect of Re on the microstructure and mechanical properties of tungsten fiber-reinforced tungsten composites. Journal of Alloys and Compounds, 184139.

[19] Wiśniewski, J., Marczewski, M., Krzyżaniak, W., Adamek, G., Jakubowicz, J., & Garbiec, D. (2025). Characterization of high-energy ball milling of WC-Ti powders and subsequent spark plasma sintering. Ceramics International.

[20] Akkaş, M., K Tabonah, T. M., A Elfghi, A. M., & Özorak, C. (2023). Powder Metallurgical Fabrication Of Co Reinforced Cunisi Matrix Composites: Microstructural And Corrosion Characterization. Technological Applied Sciences, 18(4), 64-74.

[21] Cong, S., Wu, L. H., Wang, Z. W., Wang, F. F., Zhang, X., Du, X. C., ... & Ma, Z. Y. (2025). A new economy-durability tool design to improve joint quality of titanium alloy friction stir welds. Journal of Materials Research and Technology.

[22] Ron, T., Leon, A., Bassis, M., Chen, Z., Shirizly, A., & Aghion, E. (2025). Effect of Hot Isostatic Pressing Treatment on Refractory High-Entropy Alloy WTaMoNbV Produced by Laser Powder Bed Fusion Process. Metals (2075-4701), 15(3).

[23] Wang, Y. F., Li, G. F., Chen, J. X., Luo, L. M., Qin, Y. Q., Sun, F., ... & Wu, Y. C. (2025). Deformation behaviors and microstructure evolution of sintered W-10Re alloy under different conditions. International Journal of Refractory Metals and Hard Materials, 130, 107158.

[24] Akkaş, M., Farag Aldalimi, Z. A., H Alrajhe, A. A., & S Abo Sbıa, A. E. (2025). Powder Metallurgy Processıng Of W-Based Cuttıng Tools: Impact Of Alloy Chemıstry On Mıcrostructure And Mechanıcal Performance. Technological Applied Sciences, 20(4), 107-114.

[25] Xue, T., Wang, Y., Zhang, K., & Sun, L. (2025). Role of binder phase on properties and holding ability of WC based diamond hardbanding matrix. International Journal of Refractory Metals and Hard Materials, 131, 107184.

Chapter 5

Industrial Applications of Laser Technology and Future Perspectives

Bekir GÜNEY[1], Mehmet Akif ERDEN[2]

1. INTRODUCTION

The evolution of industrial manufacturing technologies is progressing towards higher production speeds, lower energy consumption, greater dimensional precision, reduced material waste, and the ability to produce complex geometries. Although conventional machining, mechanical cutting, thermal processing, and welding methods are widely used in many industrial applications, they encounter various technical limitations-particularly when dealing with high-strength materials, precision components, and complex geometries. In this context, laser-based manufacturing technologies offer an alternative production approach by directing a high-energy-density beam onto the material in a controlled manner [1, 2].

The adoption of lasers in industrial manufacturing gained momentum, particularly with the development of laser cutting, drilling, and welding applications during the 1960s and 1980s. Today, the scope of application has expanded significantly due to the development of various laser sources, such as fiber lasers, disk lasers, high-power diode lasers, and ultra-short pulse lasers. In particular, the high electro-optical efficiency, compact design, and superior beam quality of fiber lasers have increased their utilization in metalworking applications [3].

One of the key advantages of laser-based manufacturing technologies is the ability to concentrate energy onto a very small area. This enables high processing precision while allowing only the necessary region of the material to be heated. Consequently, deformation, the heat-affected zone, and the need for secondary processing can be reduced in certain applications. However, the fact that laser-material interaction is influenced by numerous variables-such as wavelength, power density, scanning speed, focal position, material properties, and atmosphere-complicates process control [4].

[1] Assoc. Prof. Dr., Vocational School of Technical Sciences, Karamanoglu Mehmetbey University, 70200, Karaman, Turkey; guneyb@kmu.edu.tr, (ORCID: 0000-0001-9764-9313)
[2] Prof. Dr. Department of Biomedical Engineering, Karabuk University, Karabuk 78050, Turkey; makiferden@karabuk.edu.tr, (ORCID: 0000-0002-6322-4269)

Recent advancements in laser technologies are shifting focus toward the concept of smart manufacturing rather than merely concentrating on process performance. In particular, the use of real-time optical imaging, thermal cameras, acoustic sensors, laser scanning, and X-ray-based monitoring systems especially in laser additive manufacturing enables the process to be evaluated during production, rather than only after it is completed. [5]. Chen et al. (2024) emphasize that sensor-based process monitoring and machine learning-assisted defect detection in laser additive manufacturing are significant for the transition to autonomous production [6].

The primary objective of this study is to examine the industrial applications of laser beams through a comprehensive literature review and to holistically evaluate the technical, economic, environmental, and safety dimensions of laser-based manufacturing technologies. A secondary objective is to outline the current state of the integration of laser technologies with Industry 4.0, artificial intelligence, and digital twin technologies.

The study's key contributions to literature can be summarized as follows:

1. Presenting a holistic classification of industrial laser applications,
2. Comparing laser-based processes with traditional manufacturing methods,
3. Evaluating the energy and environmental performance of laser technologies,
4. Identifying key risks regarding occupational health and safety,
5. Examining the applications of sensors, artificial intelligence, and real-time control in laser processes,
6. Identifying research gaps in literature,
7. Developing a perspective on smart and sustainable laser manufacturing for future research.

To this end, the study is structured around the following research questions:

RQ1: What are the primary industrial application areas of laser beams?

RQ2: Which laser processes are more commonly used for specific materials and sectors?

RQ3: What are the main advantages and limitations of laser-based processes compared to traditional manufacturing methods?

RQ4: How are the energy and environmental performance of laser technologies evaluated?

RQ5: How are artificial intelligence, sensors, and real-time process monitoring transforming laser manufacturing technologies?

RQ6: What are the key future research gaps in laser-based manufacturing?

2. FUNDAMENTAL SCIENTIFIC PRINCIPLES OF LASER TECHNOLOGY

The term "laser" is an acronym for "Light Amplification by Stimulated Emission of Radiation." A laser beam is electromagnetic radiation produced via stimulated emission that is highly directional and coherent and possesses specific wavelength characteristics. A laser is a system that generates light through the process of stimulated emission. The fundamental properties enabling the use of laser beams in industrial applications are high directionality, high coherence, narrow spectral bandwidth, and high-power density. In the laser process, energy density is one of the fundamental parameters determining the behavior of the beam on the material surface. A material's ability to absorb laser energy is influenced by factors such as wavelength, surface condition, temperature, material composition, and the angle of incidence of the beam.

The interaction between the laser beam and the material can trigger mechanisms such as reflection, absorption, transmission, heat conduction, melting, vaporization, and plasma formation. Which of these mechanisms dominate depends on laser power, power density, pulse duration, and processing speed [4, 7, 8].

3. INDUSTRIAL LASER SOURCES AND THEIR APPLICATIONS

The primary types of industrial laser welding and their application areas are presented in Table 1. The development of fiber lasers has brought about a significant transformation, particularly in metal cutting and welding applications. High power density and beam quality enable higher processing speeds to be achieved [9].

Table I. Major laser types and industrial applications.

Laser type	**Typical feature**	**Main applications**
CO_2	Long wavelength	Cutting, surface processing
Nd	Solid-state laser	Welding, drilling, marking
Fiber laser	High beam quality and efficiency	Cutting, welding, marking
Disk laser	High power	Welding, cutting
Diode laser	High electro-optical efficiency	Surface processing, welding
Excimer laser	UV region	Micromachining, electronics
Femtosecond/picosecond laser	Ultrashort pulse	Micro/nano processing

4. LASER CUTTING

Laser cutting is based on the principle that the intense heat generated by the laser beam on the material's surface melts or vaporizes the material, while an assist gas removes the resulting material from the cutting zone [10].

Laser cutting is used particularly for processing materials such as steel, stainless steel, aluminum, copper, titanium, and composite materials [11].

The key parameters affecting the quality of the laser cutting process can be listed as follows: laser power, cutting speed, focus position, assist gas pressure, nozzle geometry, material thickness, and beam diameter [12].

Yilbas et al. (2017) demonstrated that evaluating the laser cutting process for various materials in terms of kerf width and life cycle is important for energy and process optimization [13].

Key advantages of laser cutting include high cutting speeds, narrow kerf widths, low mechanical force, the ability to cut complex geometries, suitability for automation, the absence of tool wear, and high cutting precision. Furthermore, the absence of tool wear, the capability to produce complex geometries, and ease of integration with CNC systems have expanded the method's industrial application. Current literature also emphasizes that modern laser material processing technologies encompass a wide range of applications, such as cutting, drilling, marking, welding, and surface structuring [9].

Laser cutting has limitations such as high investment costs, process constraints with thick materials, energy transfer issues with reflective materials, thermal deformation, and the generation of smoke and particulates [14].

5. LASER WELDING

Laser welding is based on directing a high-energy-density laser beam at the joining zone of two or more materials to create localized melting.

The primary advantages of laser welding technology include high welding speeds, low heat input, a narrow heat-affected zone, high precision, suitability for automation, the ability to join complex geometries, and ease of integration with robotic systems. Laser welding technology is utilized particularly for high-precision welding applications in the automotive and aerospace industries. A comprehensive review published in 2024 highlights laser beam welding as a key technology for automated and robotic manufacturing across a wide range of materials, including steel, titanium, nickel-based alloys, and specific aluminum, magnesium, and copper alloys [15].

Classic laser welding can essentially be evaluated in terms of two regimes: conduction-mode welding and keyhole-mode welding. In the keyhole regime, the

material vaporizes due to high power density, resulting in a narrow, deep weld geometry [16].

Klimpel (2024) reported that laser power, welding speed, and process parameters are decisive for weld quality in modern laser and hybrid laser welding processes, and that automation and online quality monitoring are becoming increasingly important [15].

The primary advantages and limitations of laser welding are presented in Table 2. Low deformation and high automation capability make laser welding attractive, particularly in the automotive and aerospace sectors.

Table II. Advantages and limitations of laser sources.

Advantages	Limitations
High welding speed	High initial investment
Narrow HAZ	Complexity of parameter optimization
Low deformation	Challenges with reflective materials
High level of automation	Equipment maintenance costs
Robotic integration	Process instability
Precise energy transfer	Need for in-line monitoring of defect formation

6. LASER DRILLING

Laser drilling is a significant laser processing method used particularly for creating small-diameter holes that require high precision.

While tool wear and mechanical forces can pose significant challenges in conventional mechanical drilling methods, laser drilling involves no mechanical contact.

Laser drilling is employed in applications such as cooling holes in aerospace turbine blades, fuel injection systems, electronic components, microchannels, and medical parts. The use of ultrashort-pulse lasers has made it possible to minimize thermal effects and enhance processing precision to the micrometer level [4]. However, in laser drilling, conical hole geometry, resolidified material, diameter tolerances, and the heat-affected zone can pose significant process challenges [17].

7. LASER MARKING AND ENGRAVING

Laser marking is used to create permanent, high-resolution marks on material surfaces.

Key applications include serial numbers, barcodes, QR codes, product tracking codes, brand logos, electronic component marking, and medical device traceability.

Laser marking can be easily integrated into automated systems, particularly on high-speed production lines. Bravo-Montero et al. (2022) demonstrated that high-speed laser marking using diode arrays has the potential to increase efficiency and processing speed in industrial production lines [18].

8. LASER SURFACE TREATMENTS

Lasers are used not only for shaping materials but also for modifying their surface properties. Laser surface treatments include surface hardening, remelting, alloying, coating, and texturing. Through these processes, surface hardness, wear resistance, corrosion resistance, and tribological properties can be improved [19].

Studies on laser surface remelting demonstrate that process parameters have significant effects on microstructure, mechanical properties, and wear behavior [20].

9. LASER CLEANING

Laser cleaning is a non-contact surface treatment technology that has emerged as an alternative to traditional mechanical, chemical, or abrasive cleaning methods. A comparison between laser cleaning and traditional cleaning methods is presented in Table 3. Surface contaminants such as rust, oxides, paint, oil, coatings, particles, and biological matter can be removed using controlled laser energy. Laser cleaning mechanisms primarily operate through thermal ablation, thermal stress, and plasma shock wave techniques [21].

A comprehensive 2025 assessment indicates that laser cleaning is rapidly expanding into fields such as aerospace, shipbuilding, automotive, nuclear energy, and microelectronics; however, the selection of process parameters, a full understanding of cleaning mechanisms, and the development of intelligent control remain key research challenges [22]. For this reason, laser cleaning is becoming an important area of research in terms of sustainable manufacturing.

Table III. Comparison of laser cleaning and traditional cleaning methods [23-26].

Feature	Laser cleaning	Chemical cleaning	Mechanical cleaning
Non-contact process	Yes	No	No
Chemical waste	Very low	Can be high	Low
Automation	High	Moderate	Medium
Precision	High	Moderate	Low-Medium
Surface damage	Low with appropriate parameters	Depends on the chemical	Possible due to mechanical contact
Initial cost	High	Moderate	Low-Medium
Remote operation	Possible	Limited	Limited

10. LASER MICROMACHINING AND NANOMACHINING

The need for micromachining technologies has increased with the development of microelectronics, medical devices, and precision engineering applications. Femtosecond and picosecond lasers offer significant advantages in applications requiring the limitation of thermal damage, as they deliver high energy over extremely short durations. Characteristics such as high resolution, precision, and the absence of tool wear support the use of laser micromachining technology in high-tech sectors [4].

Precision at the micrometer or even nanometer scale is required in the manufacturing of microelectronics, optics, sensors, and medical devices. Thanks to pulse durations in the femtosecond and picosecond ranges, ultra-short pulse lasers enable the limitation of heat transfer to the surrounding material. Tünnermann et al. (2023) and Orazi et al. (2021) demonstrate that ultra-short pulse lasers are becoming increasingly important in precision micromachining and advanced manufacturing applications [27, 28]. Information regarding laser micromachining application areas is presented in Table 4.

Table IV. Laser micromachining applications [4].

Application	Application areas
Micro-drilling	Electronics, aerospace
Micro-channeling	Microfluidic systems
Surface texturing	Tribology
Micro-cutting	Medical devices
Micro-marking	Electronics
Precision ablation	Optics and sensors

Laser nanoprocessing is employed in applications such as the creation of nanoscale functional structures on surfaces and the high-precision fabrication of electronic and photonic components; notably, it enables precise material processing with minimal thermal effects, thanks to the use of ultrashort-pulse lasers.

Laser nanoprocessing has become a key technology in advanced micro/nano-manufacturing, driven by the high spatial precision and low thermal impact offered by ultrashort-pulse lasers. Key applications include the creation of nanoscale functional structures on material surfaces, the precision processing of electronic and semiconductor components, and the fabrication of photonic structures. While laser-generated nanoscale surface structures allow for the controlled modification of surface functions, such as wettability, optical properties, and tribological behavior-femtosecond lasers can simultaneously be used to fabricate photonic structures like waveguides, Bragg gratings, and micro-resonators with high precision [29-31]. Information regarding laser nanoprocessing application areas is presented in Table 5.

Table V. Laser nano-processing applications [29-31].

Application area	Basic process	Laser approach used	Key advantage	Industrial/technological use
Nano-surface structuring	Creating nanoscale periodic structures on the surface	Femtosecond/ultrashort-pulse laser	High precision, low thermal damage	Functional surfaces, optical surfaces, tribological applications
Nanopatterning	Creating controlled nano-geometries on the material surface	Ultrashort-pulse laser	Non-contact and high-resolution processing	Microelectronics, sensors, and photonic devices
Photonic structure fabrication	Fabricating waveguides, Bragg gratings, and micro-resonators	Femtosecond laser	Fabrication of precise, three-dimensional structures	Optical and photonic devices
Semiconductor processing	Precision material removal, drilling, and patterning	Femtosecond/picosecond laser	Minimal heat impact and high dimensional accuracy	Electronics and semiconductor manufacturing
Nano-precision drilling	Creating very small-diameter holes	Ultrashort-pulse laser	Small Heat-Affected Zone (HAZ) and high geometric precision	Microelectronics, filters, and precision components
Surface functionalization	Modifying surface morphology and properties	Ultrashort-pulse laser	Control of wettability and optical properties	Biomedical, optical, and energy applications
Tribological surface processing	Creating nano/micro-structures that influence friction and wear	Femtosecond laser	Non-contact and controlled surface modification	Moving mechanical parts and precision systems
Micro/nanoelectronics manufacturing	Fabricating electrodes and conductive structures	Femtosecond laser	Precise and localized material processing	Electronic circuits and sensors
Laser-assisted nano-etching	Controlled material ablation and nanoscale structure formation	Short/ultrashort-pulse laser	Precise control of parameters	Microchips, sensors, and photonic components
Smart nano-processing	Data-driven optimization of process parameters	Ultrashort-pulse laser + ML/AI	Adaptive process control and quality prediction	Smart manufacturing and Industry 4.0

11. LASER-BASED ADDITIVE MANUFACTURING

Additive manufacturing is a production approach that enables the creation of three-dimensional parts by adding material in layers. Laser-based additive manufacturing methods have achieved a significant position, particularly in the production of metal parts [32, 33].

There are various applications, such as Laser Powder Bed Fusion (LPBF), Selective Laser Melting (SLM), Selective Laser Sintering (SLS), and Laser Directed Energy Deposition (LDED). Laser-based additive manufacturing offers significant advantages for producing complex geometries in the aerospace, automotive, energy, medical, and defense industries. In particular, it enables the production of parts featuring internal channels, lattice structures, and optimized geometries that are difficult to manufacture using traditional methods [34].

Herzog et al. (2016) demonstrated that metal additive manufacturing offers significant potential in terms of the production of complex geometries and design freedom [35].

However, in laser additive manufacturing, defects such as porosity, cracking, lack of fusion, excessive melting, surface roughness, residual stress, and geometric deviation can occur [32, 33].

A recent review published in 2026 reveals that beam shaping, laser oscillation, and multi-physics field support in laser-based additive manufacturing can enhance melt pool stability and contribute to the reduction of defects [36].

12. REAL-TIME MONITORING IN LASER PROCESSES

In traditional manufacturing systems, quality control is predominantly performed after production. This approach can necessitate the reproduction of the entire part or a significant portion of it when a defect occurs. In contrast, the laser-based smart manufacturing approach involves data collection during the process. Key sensors in this field include high-speed optical cameras, thermal cameras, photodiodes, acoustic sensors, laser scanners, and X-ray systems. Chen et al. (2024) highlighted the importance of multi-sensor fusion and machine learning-based defect detection, alongside optical, acoustic, laser scanning, and *operando* X-ray monitoring methods, in laser additive manufacturing [6].

13. ARTIFICIAL INTELLIGENCE AND MACHINE LEARNING

Laser processes are very suitable for artificial intelligence applications because they produce high-dimensional and non-linear data [6]. Therefore, artificial intelligence has key application areas in laser processing, such as defect classification, process parameter optimization, surface quality prediction, weld quality prediction, melt pool analysis, thermal behavior prediction, determination

of process stability, and adaptive control [15, 24]. The primary application areas of artificial intelligence in laser processes are presented in Table 6.

Table VI. Application areas of artificial intelligence in laser processes [15, 24].

AI application	Input	Output
Image classification	Camera image	Defect type
Regression	Process parameters	Quality indicator
Deep learning	Multi-sensor data	Defect prediction
Anomaly detection	Real-time signal	Abnormal condition
Optimization	Parameter space	Optimal process
Adaptive control	Sensor + model	New process parameter

However, in transferring artificial intelligence models to industrial applications, data quality, sensor calibration and generalizability of the model across different machines are as important as the size of the training data set [37, 38].

14. DIGITAL TWIN AND CLOSED-LOOP LASER MANUFACTURING

A digital twin is a digital representation of a physical production system updated with real-time data. In laser manufacturing, the digital twin approach can be modeled as follows: Physical process → Sensors → Data collection → Digital model → Artificial intelligence → Decision → Process parameter modification. By making this system a closed loop, the process is not only monitored but can also automatically correct its own behavior within certain limits. This approach is particularly important in laser additive manufacturing [39, 40].

15. SECTORAL APPLICATIONS

Laser technology is extensively used, particularly in the high-value-added and high-precision sectors listed in Table 7 below [41].

Table VII. Laser applications in key sectors.

Sector	Key laser applications
Automotive	Cutting, welding, marking
Aviation	Drilling, welding, cladding, AM
Defense	Cutting, welding, surface processing
Energy	Turbine, coating, maintenance
Electronics	Micromachining, marking
Medical	Implant, micromachining
Marine	Welding and cleaning
Railway	Welding, surface processing
Mold making	Repair, coating
Tool manufacturing	Hardening, texturing

16. COMPARISON OF LASER AND CONVENTIONAL MANUFACTURING METHODS

A comparison of laser and conventional manufacturing methods is presented in Table 8. This comparison does not imply that laser technology is superior to conventional methods in every respect; conventional methods may be more economically advantageous, particularly for low-volume production requiring lower precision. The primary advantage of laser technology becomes evident in applications demanding high precision and a high degree of automation [25, 41, 42].

Table VIII. Comparison of laser and conventional manufacturing methods [25, 41-43].

Criterion	Laser	Traditional methods
Precision	Very high	Medium-High
Contact	Non-contact	Generally, contact-based
Tool wear	None	Yes
Automation	Very high	High
Complex geometry	Suitable	Method-dependent
Processing speed	High	Method-dependent
Initial investment	High	Low-Medium
Energy density	High but localized	Wider area
Digital integration	Very suitable	Medium-High
Process monitoring	Advanced	Method-dependent

17. ENERGY EFFICIENCY AND SUSTAINABILITY

When evaluating the environmental benefits of laser-based technologies, it is important to consider not only the energy consumed during the active processing stage but also the broader life-cycle impacts associated with material inputs, auxiliary equipment, process gases, waste generation, machine usage, and end-of-life considerations. In short, from a sustainability perspective, factors such as the electrical efficiency of the laser source, process time, material loss, auxiliary gas consumption, consumables, the need for surface preparation, the rework rate, and equipment service life must be evaluated collectively [13, 44-46].

In certain applications, such as laser cleaning, eliminating chemical cleaning agents can offer significant environmental advantages. However, the electricity consumption of high-power laser systems should not be overlooked. Therefore, rather than making a sweeping statement that "laser technology is eco-friendly," it is a more scientific approach to conduct an assessment based on the specific application and its life cycle [13, 44-46].

18. OCCUPATIONAL HEALTH AND SAFETY

Occupational health and safety in the industrial use of laser systems is an important issue due to laser radiation as well as thermal, mechanical, electrical, chemical and fire-related hazards that may arise during the process. Table 9 shows the main risks and general control measures in laser processes. The main risks include exposure to direct laser beam, eye and skin damage caused by reflected or scattered beams, high temperature and thermal effects, smoke and particles formed during the process, auxiliary gases, electrical hazards, fire, and risks that may arise from interaction with machine/robotic systems [47, 48]. The ISO 11553-1 standard stipulates that, in addition to hazards arising from laser radiation, electrical, mechanical, and secondary process hazards associated with laser processing machines must also be addressed within the scope of risk assessment [49].

Safety design in laser processing systems should not be based solely on personal protective equipment (PPE); First, the aim should be to eliminate risks or reduce them to an acceptable level through engineering controls and design. In this context, closed laser cabins and protective enclosures, limitation of the beam path, safety interlock systems, beam stoppers and guidance elements, controlled access, appropriate ventilation and filtration systems and safe working procedures must be implemented together. OSHA's laser safety approach also considers engineering controls, administrative/procedural controls, and personal protective equipment; In particular, it recommends completely blocking the laser beam path whenever possible and equipping the housings with interlock systems [48].

For industrial laser processing machines, ISO 11553-1:2020 adopts a safety design based on risk assessment as its fundamental approach and mandates that access to laser radiation be restricted through enclosures and safety functions [47]. Furthermore, the ISO 11553-2:2026 standard published in 2026 specifically addresses hazards arising from electrical, thermal, and laser radiation sources, as well as those related to materials and control systems, for hand-held or hand-guided laser processing machines, and mandates the implementation of appropriate risk-reduction measures [49].

Table IX. Key risks and control measures in laser processes.

Risk	Potential consequence	Basic control
Direct beam	Eye/skin damage	Closed system
Reflected beam	Eye damage	Beam control
Fume	Respiratory risk	Local ventilation
Fire	Operational damage	Fire prevention
Electricity	Electric shock	Electrical safety
High temperature	Burn	Protective equipment
Robotic movement	Mechanical injury	Safety area
Assist gas	Pressure/fire	Gas safety

Standards such as ISO 11553-1 [47] for laser processing machines and IEC 60825-1 [50] for laser product safety must be taken into account.

19. INTEGRATION WITH INDUSTRY 4.0

Industry 4.0 refers to the transformation of production systems into interconnected, intelligent, and real-time operating structures through technologies such as the Internet of Things (IoT), cyber-physical systems, artificial intelligence, big data analytics, and digital twins [51]. Laser technologies align strongly with Industry 4.0-based smart manufacturing systems, thanks to digitally controllable process parameters, process behavior monitorable via sensors, and real-time data generation [52, 53]. In this context, smart laser manufacturing systems rely on the integrated use of components such as laser sources, CNC/robotic systems, sensors, industrial IoT, data analytics, artificial intelligence, and digital twins [54]. Thanks to this structure, the production system evolves from a system that merely executes pre-programmed operations into an intelligent, closed-loop production system capable of monitoring process status in real time, analyzing data, and adapting process parameters under appropriate conditions [6, 39].

20. LITERATURE ANALYSIS

The general topics addressed in scientific and academic studies are presented in Table 10. However, the literature indicates that the research focus particularly on laser additive manufacturing is shifting from post-process quality control to in-process quality prediction. Chen et al. (2024) identify sensor-based monitoring, machine learning, and adaptive defect correction as the key components of this transformation [6]. Das et al. (2024) also emphasize the importance of evaluating different monitoring methods such as optical imaging, thermography, and radiography-in conjunction with machine learning [55].

Table 1X. Prominent research trends in literature.

Research area	Current status	Fundamental problem	Future direction
Laser cutting	Mature technology	Parameter optimization	AI-based optimization [56]
Laser welding	High automation	Defect formation	Online quality control [57]
Laser cleaning	Rapidly evolving	Mechanism uncertainty	Smart cleaning [58]
Micromachining	High precision	Thermal effects	Ultrashort pulses [31]
LPBF	Widespread research	Defects/repeatability	Closed-loop control [59]
LDED	Developing	Geometric accuracy	Adaptive material deposition [60]
AI	Rapidly evolving	Data generalizability	Reliable AI [31]
Digital twin	Early/mid-stage	Real-time model	Autonomous manufacturing [39]

21. RESEARCH GAPS

As a result of the critical evaluation of the literature, the following key research gaps have been identified:

21.1. Lack of standard data

Data obtained from different laser systems differs in terms of formats, sampling frequencies, and sensor characteristics. This situation makes it difficult to transfer artificial intelligence models to different systems.

21.2. Model generalizability

A machine learning model that yields high accuracy on one machine may not exhibit the same performance when a different laser power, material, or optical system is used.

21.3. Real-time control

Detecting the error is not sufficient on its own. After detecting the occurrence of an error, the system must reliably modify the process parameters.

21.4. Multi-sensor fusion

The combined evaluation of optical, thermal, acoustic, and geometric data holds great potential. However, the synchronization and interpretation of multi-sensor data constitute a significant research challenge.

21.5. Explainable artificial intelligence

Explainable Artificial Intelligence (XAI) addresses a significant, yet not fully resolved, challenge in the industrial application of laser technologies. The integration of artificial intelligence and machine learning algorithms into laser-based manufacturing, material processing, quality control, and process monitoring systems offers substantial advantages regarding process parameter optimization, defect detection, and product quality prediction. However, the decision-making mechanisms of complex models, particularly deep learning models often function as "black boxes," making it difficult to understand why a model predicts a specific quality outcome or defect class for a given laser process. In industrial processes influenced by numerous simultaneous variables such as laser power, scanning speed, focal length, beam diameter, material properties, and thermal behavior linking model outputs to physical processes is crucial. A lack of explainability hinders operators and engineers from verifying AI-driven decisions and identifying the causes of erroneous predictions, while also undermining confidence in the model for critical production decisions. Consequently, industrial systems integrating laser technologies with AI must ensure not only high prediction accuracy but also the interpretability and traceability of decisions, as well as their alignment with physical process knowledge. While the use of XAI methods such as SHAP and LIME can help mitigate this limitation, the fact that these explanations do not always fully capture complex laser-material interactions remains a significant area of research.

22. FUTURE RESEARCH PERSPECTIVES

Potential future research areas for laser systems are summarized in Table 11. Furthermore, laser systems are expected to be viewed not merely as high-power beam sources, but as active components of cyber-physical manufacturing systems integrated with sensors, data analytics, artificial intelligence, digital twins, and feedback control mechanisms [61, 62].

Table XI. Future research areas.

Field	Research requirement
Smart laser	Autonomous process control
Artificial intelligence	Explainable and generalizable models
Sensor fusion	Multi-data integration
Digital twin	Real-time physical model
Sustainability	Life cycle analysis
Laser cleaning	Energy and waste optimization
AM	Zero-defect manufacturing
Robotics	Human-robot-laser safety
Ultra-short laser	Reduced thermal impact
Big data	Standardized data infrastructure

A general review of the literature indicates that the role of laser technologies in industrial manufacturing has evolved through three key stages.

The first stage is the period of enhancing process performance. During this phase, the primary research focus was on physical performance indicators such as laser power, beaming quality, cutting speed, welding depth, and surface quality.

The second stage is the era of automation and robotic integration. High production speeds and repeatability were achieved by integrating laser systems with CNC machines, robots, and automated production lines.

The third stage, which is currently evolving, is smart laser manufacturing. In this phase, data obtained from sensors are analyzed using artificial intelligence and digital models, with the aim of controlling the process in real time.

This transformation is particularly evident in laser additive manufacturing. Recent studies show that process monitoring systems are increasingly being used not merely for data collection, but to predict defect formation and enable intervention during production.

However, one of the major challenges facing smart laser manufacturing is transferring the success of artificial intelligence models from laboratory conditions to industrial environments. A model trained in a laboratory setting under fixed material, laser, atmospheric, and optical conditions is not guaranteed to achieve the same level of success on different production machines.

Therefore, future research must focus not only on model accuracy but also on model transferability, uncertainty analysis, explainability, and reliability.

23. RESULTS

In this study, industrial applications of laser beams were examined considering existing literature. It was observed that laser cutting, welding, drilling, marking, surface processing, cleaning, micromachining, and additive manufacturing hold significant application areas within modern production systems.

The primary advantages of laser technologies include high precision, non-contact processing, high power density, automation, robotic integration, and the ability to process complex geometries. Conversely, high investment costs, sensitivity to process parameters, material-dependent optical properties, and safety requirements emerge as key limitations.

While laser welding and cutting technologies have become mature applications-particularly in the automotive, aerospace, and metal manufacturing sectors-laser cleaning, ultra-short pulse laser micromachining, and laser additive manufacturing represent rapidly evolving research areas.

One of the study's most significant findings is the shift in research trends within laser technologies from conventional process optimization to intelligent process control. Technologies such as sensors, artificial intelligence, machine learning, and digital twins will play a critical role in the future development of laser manufacturing systems.

In laser additive manufacturing specifically, real-time process monitoring and adaptive control are replacing the "produce and inspect later" approach with a "monitor during production and correct as needed" strategy. This transformation is of great importance for the development of near-zero-defect production systems.

Furthermore, future studies should focus on four key areas:

1. Generation of standardized process data,
2. Development of generalizable and explainable artificial intelligence models,
3. Development of real-time control systems based on multi-sensor fusion,
4. Evaluation of laser processes in terms of economic and environmental life cycles alongside technical performance.

Ultimately, the future of laser technologies does not depend solely on the development of higher-power laser sources. The true transformation will occur through the integration of the laser source with sensors, robotic systems, artificial intelligence, digital twins, and closed-loop control infrastructures. Therefore, it is anticipated that the laser manufacturing systems of the future will evolve into high-precision, automated, self-monitoring, adaptive, and sustainable production systems.

REFERENCES

1. Chryssolouris, G. (2013). Laser machining: theory and practice. Springer Science & Business Media.
2. Steen, W.M., Mazumder, J., & Watkins, K.G. (2010). *Laser material processing*. *Springer,* Vol. 4.
3. Bogue, R. (2010). Fifty years of the laser: its role in material processing. *Assembly automation*, 30(4), 317-322.
4. Sahu, A.K., Malhotra, J., & Jha, S. (2022). *Laser-based hybrid micromachining processes: A review.* Optics & Laser Technology, 146, 107554.
5. Casalino, G. (2018). Computational intelligence for smart laser materials processing. *Optics & Laser Technology,* 100, 165-175.
6. Chen, L., et al., (2024). In-situ process monitoring and adaptive quality enhancement in laser additive manufacturing: a critical review. *Journal of Manufacturing Systems.* 74, 527-574.
7. Li, S., et al., (2025). A novel beam shaping method for adjustable focus Gaussian-ring mode laser in high-quality welding process. *Optics & Laser Technology,* 190, 113180.
8. Chen, Z., et al., (2026). A review of beam shaping technology in laser welding applications. *The International Journal of Advanced Manufacturing Technology*, 143(3),1133-1160.
9. Tumkur, T.U., et al., (2025). *A review of laser materials processing paradigms.* MRS Bulletin, 50(12), 1519-1538.
10. Biswas, D.J. (2026). Shaping with Light: The Many Faces of Laser Material Processing, in A Beginner's Guide to Lasers and Their Applications, Part 2: The Laser's Impact on Science and Humanity. *Springer*, 297-327.
11. Khatak, P., (2022). Laser cutting technique: A literature review. *Materials today: proceedings*, 56, 2484-2489.
12. Alsaadawy, M., et al., (2024). A comprehensive review of studying the influence of laser cutting parameters on surface and kerf quality of metals. *The International Journal of Advanced Manufacturing Technology*, 130(3), 1039-1074.
13. Yilbas, B.S., Shaukat, M.M. & Ashraf, F. (2017). Laser cutting of various materials: Kerf width size analysis and life cycle assessment of cutting process. *Optics & Laser Technology,* 93, 67-73.
14. Hussein, A. (2026). Advanced Laser Cutting Strategies for Pollution Control: Integrating Material Optimization and Energy-Efficient Path

Planning in Sustainable Manufacturing. *Al Arish Institute Engineering Journal,* 1(1), 37-43.

15. Klimpel, A. (2024). Review and analysis of modern laser beam welding processes. *Materials,* 17(18), 4657.

16. dos Santos Paes, L.E., et al., (2026). Machine learning for bead geometry prediction in 5083-H112 aluminum laser welding considering a challenging dataset. J*ournal of Materials Research and Technology,* 41, 5796-5808.

17. Wang, B., et al., (2026). Aircraft Engine Turbine Blade Air Film Hole Processing Technology: A Systematic Review. *International Journal of Precision Engineering and Manufacturing,*1-27.

18. Bravo-Montero, F., Castells-Rufas, D., *&* Carrabina, J. (2022). High-speed laser marking with diode arrays. *Optics & Laser Technology,* 146, 107551.

19. Kumar, R., Mahajan, S., *&* Kumar, N. (2026). Laser surface modification techniques and their impact on various properties of aluminum alloys: a comprehensive review. *Journal of Adhesion Science and Technology,* 1-38.

20. Piscopo, G. *&* Iuliano, L. (2022). Current research and industrial application of laser powder directed energy deposition. *The International Journal of Advanced Manufacturing Technology,* 119(11), 6893-6917.

21. Cui, Z., et al. (2026). A Review of Laser Cleaning Technology: Mechanisms, Applications, and Performance Analysis. *in Journal of Physics: Conference Series. IOP Publishing.*

22. Flachbart, N., et al., (2025). Laser Cleaning Technologies in Industry: Mechanisms, Applications, and Future Directions for Sustainable Surface Treatment.1-6

23. Zhou, K., et al. (2022). Principle, application and development trend of laser cleaning. *in Journal of Physics: Conference Series. IOP Publishing.*

24. Fang, G., et al., (2025). Research progress of laser cleaning technology for industrial fields in the past decade. *Optik,* 331,172354.

25. Zhu, G., et al., (2022). Mechanism and application of laser cleaning: A review. *Optics and Lasers in Engineering,* 157, 107130.

26. Zhou, Z., et al., (2023). The fundamental mechanisms of laser cleaning technology and its typical applications in industry. *Processes,* 11(5), 1445.

27. Tünnermann, A., Momma, C., *&* Nolte, S. (2023). Perspective on ultrashort pulse laser micromachining. *Applied Physics. A, Materials Science & Processing,* 129(2), 157.

28. Orazi, L., et al., (2021). Ultrafast laser manufacturing: from physics to industrial applications. *CIRP Annals,* 70(2), 543-566.

29. Bonse, J., et al., (2026). Laser-induced nanostructuring. *Photoniques,* (137), 48-53.
30. Verma, J., et al., (2026). Recent advances in ultra-precision manufacturing of electronic, photonic and quantum devices. *Advanced Manufacturing,* 3(1), 13.
31. Sun, Z., et al., (2026). A review of the application of machine learning in short-pulse and ultrashort-pulse laser etching. *Optics & Laser Technology,* 198, 114871.
32. Güney, B. & Erden, M.A. (2025). Effect of heat treatments on microstructural and tribological properties of 3D printed 18Ni-300 maraging tool steel made by selective laser sintering process. *Science of Sintering,* 57, 155-176.
33. Abdalla, A.N., & Sarhan, A.A.D. (2026). In Situ Hybrid Metal Additive Manufacturing: A Review of Architecture, Active Defect Mitigation, Microstructure Refinement, Real-Time Surface Integrity Enhancement, and Digital Integration. *Arabian Journal for Science and Engineering,* 1-70.
34. Sibisi, T.H., et al., (2023). LAM additive manufacturing: a fundamental review on mechanical properties, common defects, dominant processing variables, and its applications. *The International Journal of Advanced Manufacturing Technology,* 128(7), 2847-2861.
35. Wycisk, E., et al., (2016). Additive manufacturing of metals. *Acta Materialia,* 117, 371-392.
36. Lian, R., et al., (2026). Advancements in laser processes for additive manufacturing: techniques and future directions. *Journal of Materials Research and Technology,* 41, 2428-2451.
37. Paolini, D., et al., (2026). Advanced fault detection and diagnosis exploiting machine learning and artificial intelligence for engineering applications. *Electronics,*15(2), 476.
38. Guo, Y., et al., (2024). A review on adversarial–based deep transfer learning mechanical fault diagnosis. *Journal of Big Data,* 11(1), 151.
39. Rao, K.V., & Vaneesha, K.V. (2026). Updating digital twin in supervisory control and data acquisition for sustainable laser beam micro machining. *Advanced Engineering Informatics,* 71, 104355.
40. Wu, X., et al., (2026). Design of laser-assisted processing digital twin system. *Journal of Manufacturing Systems,* 85, 155-174.
41. Deepak, J., Anirudh, R., & Sundar, S.S. (2023). Applications of lasers in industries and laser welding: A review. *Materials Today: Proceedings,*1-6.
42. Ready, J.F. (1997). Industrial applications of lasers. *Elsevier,* 1-599

43. Anderson, M., Patwa, R., *&* Shin, Y.C. (2006). Laser-assisted machining of Inconel 718 with an economic analysis. *International Journal of Machine Tools and Manufactur*e, 46(14), 1879-1891.

44. Shuja, S., YilBaS, B., *&* Shaukat, M. (2026). Life-Cycle Assessment of Laser Drilling in AISI 304 and Inconel 625: Energy, Gas Use, and Equipment Choice. *Lasers in Engineering (Old City Publishing)*, 61(1-3), 157.

45. Faludi, J., et al., (2017). Environmental impacts of selective laser melting: do printer, powder, or power dominate? *Journal of Industrial Ecology,* 21(S1), 144-S156.

46. Reduan, M.T., et al., (2025). A generic mathematical model for gate-to-gate carbon emissions in laser materials processing. *Proceedings of the Institution of Mechanical Engineers, Part B: Journal of Engineering Manufacture*, 239(1-2), 65-75.

47. Standardization, I.O.F. (2020), Safety of machinery—Laser processing machines—Part 1: Laser safety requirements. *ISO 11553-1:2020*.

48. Labor, U.S.D.O. (2026). Occupational Safety and Health Administration. (n.d.). Guidelines for laser safety and hazard assessment. U.S. Department of Labor. *OSHA – Guidelines for Laser Safety and Hazard Assessment*. OSHA.

49. Standardization, I.O.F. (2026). Safety of machinery-Laser processing machines-Part 2: Safety requirements for hand-held or hand-operated laser processing machines. *ISO 11553-2:2026*.

50. Commission, I.E., (2014). Safety of laser products - Part 1: Equipment classification and requirements.

51. Zhong, R.Y., et al., (2017). Intelligent manufacturing in the context of industry 4.0: a review. *Engineering,* 3(5), 616-630.

52. Cai, W., et al., (2020). Application of sensing techniques and artificial intelligence-based methods to laser welding real-time monitoring: A critical review of recent literature. *Journal of Manufacturing systems*, 57, 1-18.

53. Cai, Y., et al., (2023). A review of in-situ monitoring and process control system in metal-based laser additive manufacturing. *Journal of Manufacturing Systems*, 70, 309-326.

54. Tariq, U., et al., (2023). A state-of-the-art digital factory integrating digital twin for laser additive and subtractive manufacturing processes. *Rapid Prototyping Journal,* 29(10), 2061-2097.

55. Das, A., et al., (2024). A critical review of process monitoring for laser-based additive manufacturing. *Advanced Engineering Informatics,* 62, 102932.

56. Patil, C.V., Trikal, S.P., & Shahade, A.K. (2026). A taxonomy of artificial intelligence techniques for machining parameter optimization. *Multiscale and Multidisciplinary Modeling, Experiments and Design*, 9(1), 155.

57. Voets, J., et al., (2026). A Systematic Review and Taxonomy of Machine Learning Methods for Process Optimization and Control in Laser Welding. *Applied Sciences,* 16(3), 1568.

58. Elhamali, S., et al., (2025). Artificial intelligence meets laser technology: A review of recent advances. *Results in Surfaces and Interfaces,* 19, 100484.

59. Taghian, M., et al., (2026). Toward closed-loop quality assurance in powder bed fusion additive manufacturing: Defect detection, machine learning, and computational modeling. *Journal of Manufacturing Processes,* 160, 50-81.

60. Fallahi, H., et al., (2026). Machine Learning in Directed Energy Deposition: A Systematic Literature Review. *Journal of Manufacturing Processes,* 175, 76-108.

61. Liu, Q., et al., (2026). Decoupled Graph Attention Modeling and Anomaly Traceability Method for Multisystem Coupling in SLM Equipment. *Sensors,* 26(12), 3889.

62. Moon, J., et al., (2026).Unifying data model of manufacturing processes for cross-domain collaboration in the Internet of Production. *Production Engineering,* 20(2), 67.

Chapter 6

Intravenous (IV) Stand with Human Following Ability and Its Prototype Study

Oktay ADIYAMAN[1]

1. INTRODUCTION

Together with recent developments in health technologies, autonomous and smart systems use in the hospitals have been made widespread in order to improve patient care and treatment and to alleviate the workload of the health-staff working there. The patients receiving inpatient treatment in the hospitals and healthcare institutions face numerous problems. While some of these problems are related to the patients having inpatient treatment, the others are related with the staff serving as patient caregiver, nurse etc.. One of the foremost challenges is patient transportation and mobilization. Mobilization is a critical component during healing of the patient. Early mobilization is of great significance in reducing the risk of such cases as venous thromboembolic, preserving the capacity of the lungs and preventing the atrophy of muscles. Among hospitalized patients, those receiving intravenous (IV) therapy constitute one of the most frequently encountered patient groups. Mobility is considerably more difficult for patients receiving intravenous (IV) therapy because of the heavy serum stands that must be manually transported. Traditional IV stands require patients to use one hand for support, thereby increasing the risk of loss of balance and falls, as well as IV line dislodgement or excessive tension. Furthermore, mobilizing these devices poses a significant physical challenge for elderly, bariatric, or physically impaired patients. This situation may cause patients to avoid movement or request assistance from healthcare personnel or accompanying individuals whenever mobilization is required, thereby negatively affecting clinical efficiency.

Following a comprehensive review and research into existing IV stands, it has been observed that these stands can be classified into two main categories. The first category consists of IV stands developed for research purposes. The other type comprises the IV stands currently used in most hospitals, hereafter referred to as “commercially available IV stands. Research-oriented IV stands are categorized into two types: autonomous IV stands [1] and robotic IV stands [2].

[1] Assoc. Prof. Dr., Beşiri Organized Industrial Zone Vocational School / Department of Machinery and Metal Technologies, Batman University, Turkey, oktay.adiyaman@batman.edu.tr, (ORCID: 0000-0002-2674-3836)

Commercially available IV stands fall into various designs—as shown in Figures 1(a)–1(g)—including, but not limited to, the ambulatory patient support stand [3], home care IV stand [4], pole-type IV stand [5], Brewer stands [6], and the Dyaun IV stand [7-8]. Commercial IV stands are shown in Figures 1(a)–1(e), while research-oriented stands are shown in Figures 1(f) and 1(g).

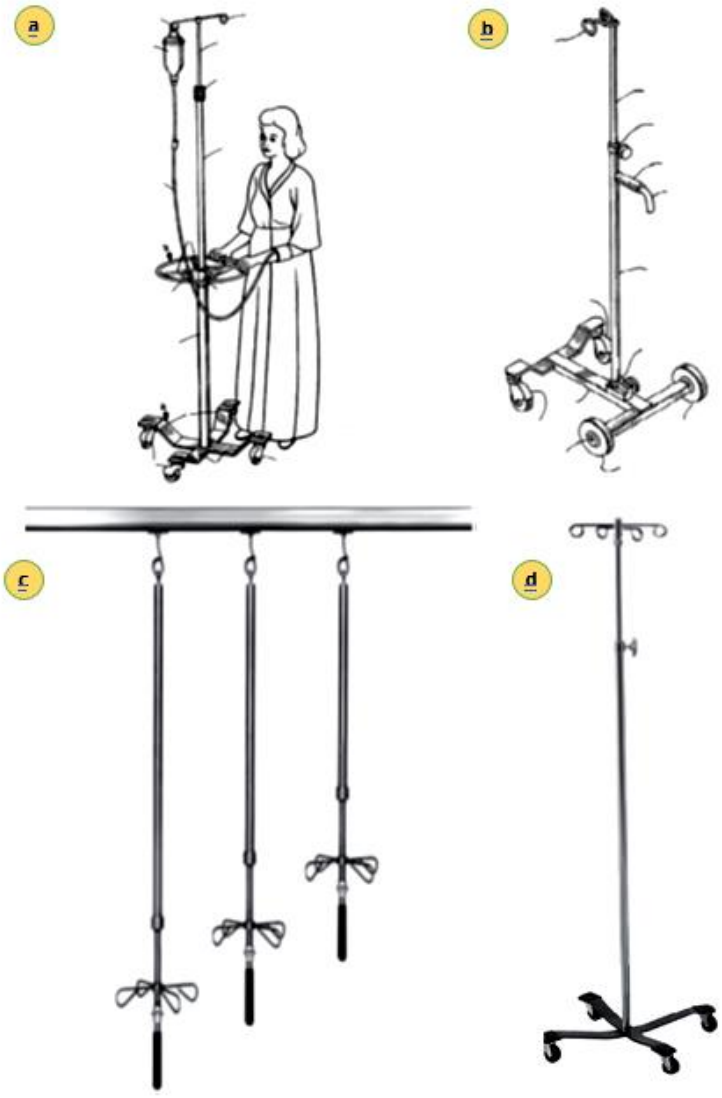




Figure 1. Different types of (IV) stands [9] (a) Ambulatory patient support stand [3]. (b) Homecare IV stand [4]. (c) Hanging IV pole [5]. (d), Simple free-standing pole [6]. (e) Dyaun IV stand [8]. (f) Autonomous IV pole [1]. (g) Robotic IV pole [2].

In recent years, alongside advancements in robotics, software, and intelligent systems, research into making medical transport robots autonomous has gained momentum. Existing autonomous mobile robots in the literature generally rely on principles such as line following, LiDAR-based mapping (SLAM), or following specific markers. However, in complex, dynamic hospital environments with high human density, these methods also entail certain limitations. These limitations can be listed as follows in terms of the technique employed:

- Line-following transport systems do not allow for flexible route planning; thereby, restrict the patient's freedom of movement.
- A transport system relying solely on SLAM-based navigation may have limitations in human- or patient-centered operation, particularly in adapting to the patient's individual movement speed and instantaneous stops.
- Marker-based or wireless signal-based (UWB/Bluetooth) following systems, on the other hand, entail additional hardware costs and require the patient to carry an additional device.

In this study, an autonomous IV stand system capable of detecting a person in real time and following the target patient at a safe distance by processing visual and depth data was developed to overcome the aforementioned disadvantages. The system integrates RGB-D depth cameras with advanced artificial intelligence-based object detection and following algorithms (e.g., YOLO and DeepSORT), enabling precise following of the patient without requiring the patient to carry any additional device. In addition, patient safety was prioritized through the system's obstacle detection and dynamic path-planning capabilities.

2. OBJECTIVE, SCOPE, AND PREVIOUS STUDIES

The primary objective of this study is to design an autonomous IV stand prototype with human-following capabilities that enables patients receiving intravenous (IV) therapy to move safely, independently, and comfortably, and to evaluate its performance under clinical environmental conditions.

The primary original contributions of the study to the literature and practice are as follows:

1. Visual-Based Real-Time Human Following: Target patient identification and following (target-locking) using only image processing and depth analysis, without the need for any additional wearable sensor.

2. **Safe Following Distance Algorithm:** Dynamic distance control that adapts to the patient's steps, walking speed, and momentary stops while preventing tension or entanglement of the IV tubing.

3. **Obstacle Avoidance Adapted to Hospital Environments:** The ability to autonomously stop and navigate around or avoid other people, wheelchairs, or stationary obstacles that suddenly appear in the corridors.

4. **Enhancing Patient Independence:** Contributing to the psychological and physical recovery process by enabling the patient to move without needing assistance from others.

Autonomous mobile medical support systems capable of following patients have been extensively investigated in recent years as part of the integration of robotics into the healthcare sector [1]. These studies, which aim to facilitate the mobilization of patients undergoing intravenous (IV) infusion therapy, have progressed through three main developmental stages, ranging from mechanically tethered systems to fully autonomous, artificial intelligence-based following systems.

The concept of patient-following IV stands emerged from the idea of eliminating the need for patients to physically push the stand [9]. One of the earliest significant milestones in the literature is the "Autonomous IV Stand" project developed by Binger et al. [1] at the Rochester Institute of Technology. This project can be regarded as one of the early examples in the literature of an autonomous IV stand capable of following a patient. The primary objective of the project is to mitigate the physical limitations of conventional IV stands, such as their wide base and limited carrying capacity, alleviate the difficulties experienced by physically weak patients in maneuvering these systems, and enable the IV stand to autonomously follow the patient within the hospital. In the design, a nylon cord/tether connection was employed between the patient and the robotic system, with the patient's direction of movement and position detected through this mechanical linkage to control the movement of the IV stand. The design also aimed to incorporate a smaller base, greater capacity for carrying IV fluid bags, and the ability to be attached to a hospital bed or wheelchair. A key outcome of the study was the demonstration that the "patient-following" approach can be implemented as a feasible engineering solution for IV stands. However, the system's tethered connection to the patient represented a significant limitation in terms of contactless human following in the modern sense.

The second stage of research on IV stands comprises semi-autonomous and remotely controlled systems that operate with active intervention by the patient. The robotic IV stand, entitled "Cutting-Edge Robotic Intravenous Pole," developed by Sayed et al. (2017) [2], was designed to facilitate the

maneuverability of conventional IV stands and to alert the user when the IV fluid bag becomes empty. The system incorporates Arduino-based electronic control, RF communication, omni-wheels, motors, and an alarm mechanism for the IV bag. However, this prototype is not a system that directly "follows the human." Movement was controlled through commands provided by the user via a joystick. Therefore, the study should be regarded as a technological precursor to—rather than a direct version of—human-following IV stands. In the user evaluation conducted, 87.55% of nurses, 94.60% of patients, and 84% of the human resources group expressed positive views regarding the system's health benefits. The authors also proposed that, in future developments, the joystick-controlled system could be automated and equipped with obstacle-detection capabilities. These recommendations support the technical rationale for the fully autonomous following systems developed subsequently.

In the third stage, the field progressed toward fully autonomous and contactless following technologies.

The BMIVPOT system, developed by Sayed-Kassem et al. (2020) [9], represents one of the most comprehensive peer-reviewed studies on human-following IV stands. The aim of this study is to transform an IV stand into a biomedical robot capable of fully autonomous movement and clinical monitoring functions, thereby surpassing the partial automation found in previous research systems. The system incorporates a Raspberry Pi 3 and a camera-based patient-following mechanism, in which a custom TAG with an approximately 15 cm side length, worn by the patient, is identified using image-processing techniques, while an Arduino UNO and four Mecanum wheels are employed for motion control. Thus, the system was designed to enable the IV stand to determine the patient’s position and move accordingly while maintaining a safe distance. In addition, functions such as monitoring serum volume via a load cell, detecting blood leakage and flow using optical sensors, obstacle detection via ultrasonic sensors, and wireless communication have been incorporated into the system. The experimental evaluation demonstrated that the camera-based following mechanism could recognize the TAG from different angles and under conditions involving obstacles, enabling the IV stand to follow the patient. The primary contribution of the study is the transformation of the IV stand from merely a mobile carrier into an autonomous platform that integrates patient following and medical monitoring functions.

More recently, Oguri et al. (2021) [10] developed a contactless LIDAR-based system that does not require the patient to carry any marker (TAG) or additional hardware. Oguri et al., whose study was based on the principle of a “robotic IV stand that moves alongside a human,” are among the prominent Japanese

researchers to have directly addressed the concept of a robotic IV stand capable of following a person. The primary objective of this study is to reduce the risk of tripping or falling associated with pushing a traditional IV stand while walking, and to enable the stand to move automatically alongside the user without physical contact. The prototype incorporated omni-directional wheels, LIDAR, a Raspberry Pi, and an Arduino Due. By mounting the LIDAR on the lower section of the carrier, the user's feet were detected, and the user's direction of movement and approximate center of gravity were determined based on the feet's positions. The control algorithm was designed to ensure that the IV stand maintained an appropriate position alongside and slightly ahead of the user. The experiments demonstrated that the prototype can automatically move with the user at walking speeds of approximately 0.3–0.8 m/s. This study is particularly significant for shifting towards LiDAR-based, contactless human following, in contrast to previous approaches that required tethers or special markers.

Oguri et al. (2023) [11] also worked on a robotic IV stand designed to reduce the risk of falls, improving upon a previous prototype with a specific focus on fall prevention. The aim of this study is to enable the user to walk without touching the IV stand and to ensure the stand moves alongside the user while maintaining an appropriate distance. The system is based on an infrastructure comprising omni-wheels, LIDAR, a Raspberry Pi, and an Arduino Due. The control approach was designed to detect the user’s two legs using the point cloud obtained from the LIDAR sensor, determine the user’s direction of movement, and maintain an appropriate distance between the IV stand and the user. The experimental results demonstrated the functionality of both the control algorithm for following the user’s direction of movement and the distance-maintenance algorithm. The study demonstrates that the human-following IV stand can be viewed not only as a robot that facilitates ease of movement but also as a safety technology aimed at reducing the risk of falls or tripping associated with traditional IV stands.

In their study, Castillo et al. (2023) [12] targeted pediatric patients specifically through the “Patient Following and Following IV Pole” project, developed at the UC Irvine Samueli School of Engineering. The aim of this study was to reduce the need for children undergoing prolonged hospitalization to continuously move IV stands carrying multiple infusion pumps and other IV equipment, either independently or with the assistance of a parent or nurse. The project aimed to enhance mobility, independence, and a sense of normalcy within the hospital environment for children by developing a robotic IV stand that follows and follows the patient. During the design process, surveys and focus group sessions were conducted with potential users, and user needs were evaluated in collaboration with the Children’s Hospital of Orange County. The project was

presented in 2023 as part of the UCI Biomedical Device Design initiative and received the Dean's Choice Award. However, this study is a senior design/prototype development project rather than an academically peer-reviewed clinical trial; therefore, instead of drawing definitive conclusions regarding clinical efficacy or safety, it outlines design requirements and the potential for feasibility regarding pediatric use.

A comparative summary of the studies discussed above in terms of the sensor technologies employed, following algorithms, and clinical applicability is presented in Table 1.

Table 1. General characteristics of IV pole studies

Study / Author(s)	Year	Following Approach	Sensor Technology	Advantages	Disadvantages/Limitations
Binger et al.	2015	Mechanical Connection (Tether)	Potentiometer, Encoder	Simple detection mechanism	It requires a physical connection and is restrictive.
Sayed-Kassem et al.	2017	Semi Autonomous (Joystick)	RF Module, Omni-wheel	High load carrying capacity (15 kg)	The patient needs to operate the controls continuously.
Sayed-Kassem et al. (BMIVPOT)	2020	Visual Label Following (TAG)	Camera, Raspberry Pi, Ultrasound	Integration of multiple biomedical sensors	There is a requirement to wear a special tag due to light sensitivity.
Oguri et al.	2021-2023	Contactless Side-by-Side Following	LIDAR, Omni-wheel, Arduino Due	Markerless following, fall risk prevention	High sensor costs and congestion in confined spaces are present.
Castillo et al. (UCI IVBot)	2023	Pediatric-Focused Autonomous Monitoring	Infrared and Ultrasonic Sensors	High patient intake, personal belongings area	Lacks clinical validation; currently in the prototype stage.

An examination of existing literature reveals that the vast majority of developed systems have remained at the laboratory or preliminary prototype stage. Comprehensive clinical validation studies addressing real-world hospital conditions, including dynamic obstacles (e.g., suddenly moving nurses, wheelchairs, and narrow patient-room doorways), poor or variable lighting conditions, and the risk of tension in infusion tubing, remain limited. In this study, a prototype design for an autonomous IV stand was developed, the system's key components were defined, and insights were provided to scientists regarding research in this field. It is hoped that these IV stands, designed with a problem-

solving approach to ensure trouble-free operation, will be put into service in hospitals in the coming years and made available for use by patients, caregivers, and companions.

3. MATERIALS AND METHODS (SYSTEM ARCHITECTURE)

The developed and mechanically designed autonomous IV pole system consists of five main subsystems, encompassing the hardware architecture, sensor fusion, and human-following control software.

3.1. Hardware Architecture and Mechanical Design

The mobile base of the robotic IV stand features a free-wheeling design to ensure high maneuverability. Lightweight aluminum profiles and Plexiglass materials, suitable for sterilization, have been selected for the body structure. The system hardware comprises the following key components:

- **Main Processing Unit:** A single-board computer (Raspberry Pi 4 / NVIDIA Jetson series) to execute real-time image processing and artificial intelligence algorithms.
- **Microcontroller:** A subordinate controller (Arduino Due / STM32) that communicates with the system to generate low-level PWM signals for the motor drivers and acquire sensor data.
- **Drive System:** Two high-torque DC gear motors with driver boards, plus one steering motor and driver at the front.
- **Lifting drive system:** An additional DC motor and drivers to adjust the IV pole to the desired height.
- **Power Management:** A 12V LiFePO4 battery pack and voltage regulators ensuring uninterrupted operation.

A prototype design was developed by taking all components of the IV stand into consideration, resulting in the configuration shown in Figure 2.



Figure 2. The designed prototype

All elements of the prototype design, the complete view of which is shown in Figure 2, are presented in Figure 3.

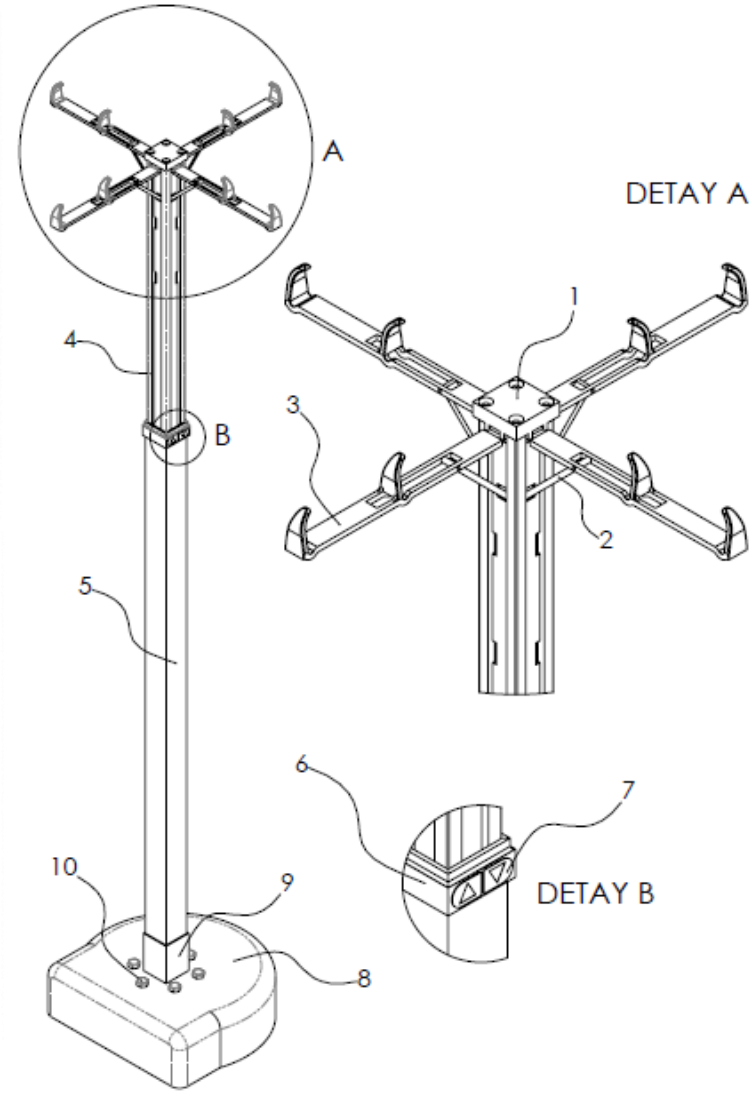


Figure 3. Names of IV Stand Components

The components of the mobile sub-carrier assembly, shown in full in Figure 2 and in a numbered view in Figure 3, are named below:

1	Top cover	2	Support plate
3	IV stand	4	Movable carriage
5	Fixed Linear Guide	6	Height Adjustment Button Assembly
7	Up and down buttons	8	Mobile Lower Support Assembly
9	Subassembly Connection Profile	10	Assembly Bolts

3.2. Mobile Lower Support Assembly

In addition to the general perspective views presented in Figures 2 and 3, the components of the IV stand, including the drive motors, electronic circuits, wheels, and battery, are housed within the lower assembly. The perspective view and assembly components of the lower assembly are shown in Figure 4.

The lower assembly, which ensures the dynamic stability of the system and provides mobility, lowers the center of gravity by concentrating the heavier components at the base, thereby minimizing the risk of tipping.

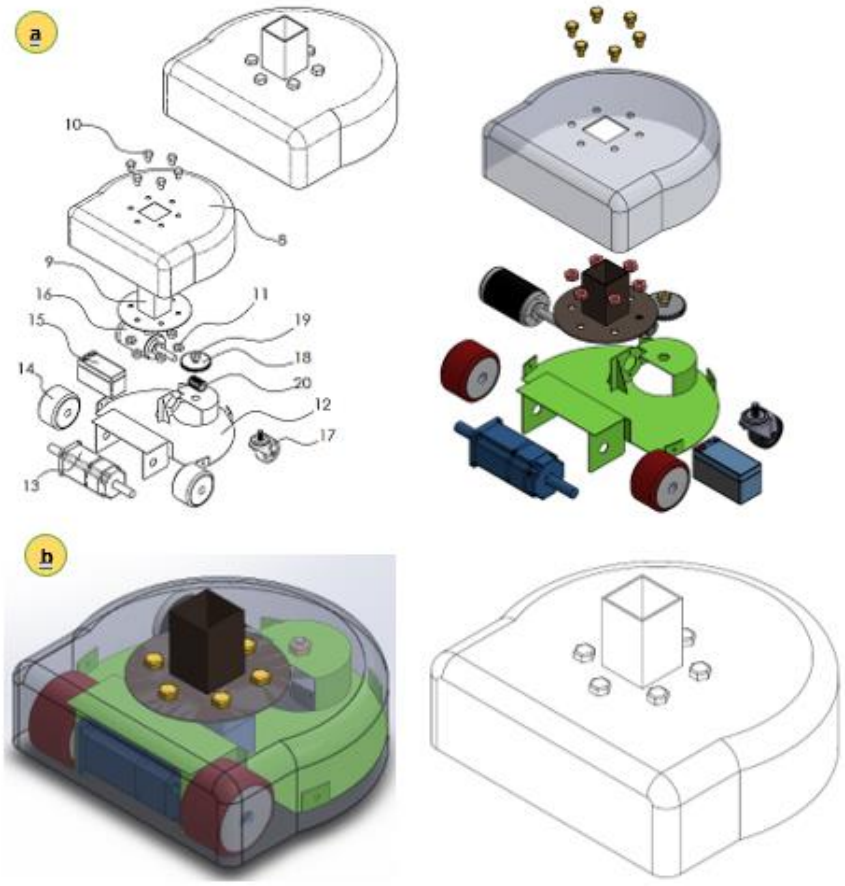


Figure 4. Mobile Lower Support Assembly a) Exploded View b) Assembled View

The components of the mobile lower support assembly, shown in exploded and fully assembled views in Figures 4(a) and 4(b), respectively, are named as follows:

8	Outer Enclosure	9	Subassembly Joining Profile
10	Assembly Bolts	11	Assembly Nuts”
12	Chassis	13	Forward/Reverse DC Motor
14	Load-Bearing Wheels	15	Battery
16	Left-Right DC Motor	17	Swivel Caster Wheel
18	Worm Gear Mechanism	19	Worm Screw Mounting Nut
20	Worm Screw		

The key components of the mobile lower support assembly can be summarized as follows:

Chassis and Protective Cover (Enclosure)

Chassis: As shown in Figures 4(a) and 4(b), the green-colored lower support chassis plate serves as the main body, housing the motors, battery, and steering wheel.

Outer Enclosure: A protective upper cover made of sheet metal or durable plastic (e.g., ABS) is used to protect the electronic components and mechanical transmission parts from external factors (e.g., dust and liquid exposure) while providing an aesthetically pleasing clinical appearance (Figure 4).

Drive and Steering System

Main Drive Components: Two large-surface main drive wheels are positioned on the sides of the chassis (Figure 4a and b).

Support and Steering: A free-swiveling caster wheel with a rotary joint, attached to the rear of the chassis, enables the system to maneuver around its own axis and steer freely through 360 degrees.

Power Supply

The dry/gel battery unit (Figure 4), which enables autonomous movement of the system, is secured to the lower chassis at a position that ensures balanced weight distribution.

3.3. Vertical Movement (Elevator) Mechanism

The linear mechanism, designed to adjust the height of the IV fluid bottle/bag and accommodate the user's height, is based on a high-precision lead screw drive system (Figure 5).

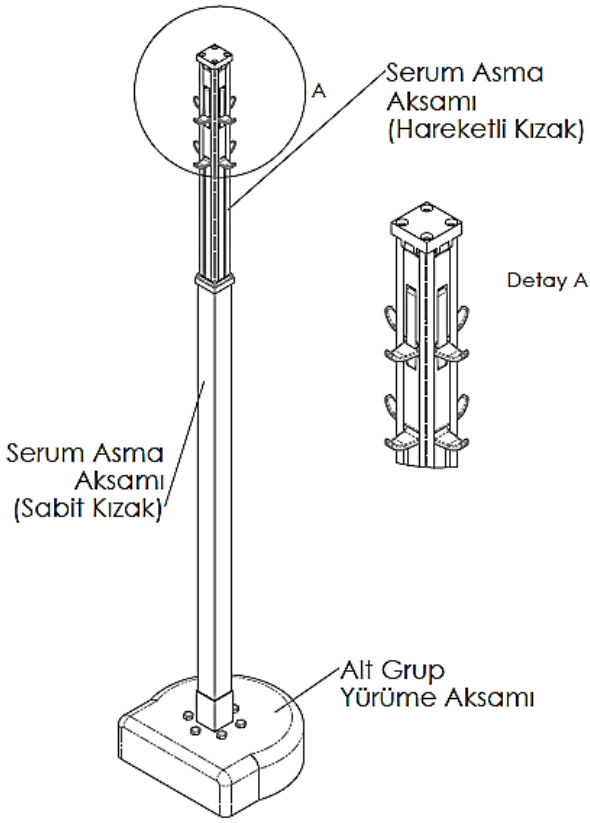


Figure 5. General view of the vertical movement (elevator) mechanism

The sub-components of the vertical movement mechanism can be summarized as follows:

Guide and Carriage Bearing System (Linear Slide System)

Fixed Linear Slide System: The external profile structure secured within the profile sleeve on the lower body (Figure 5).

Moving Carriage: A profiled arm that moves telescopically along the vertical axis within the fixed carriage and supports the upper body and hooks of the IV stand (Figure 5).

Screw-Nut Drive Mechanism

Lead Screw & Nut Assembly: Vertical movement is achieved by a precision lead screw and an integrated lead nut mechanism that operates in conjunction with the screw (Figure 6).

Geared Stepper Motor: The stepper motor that drives the lead screw (Figure 6) transmits its rotational motion to the lead screw through a gear transmission (gear pair) (Figure 6). This provides a self-locking or precisely positionable

lifting force capable of counteracting the IV fluid loads that may be applied from above. Motor control (up/down) is performed using up/down buttons.

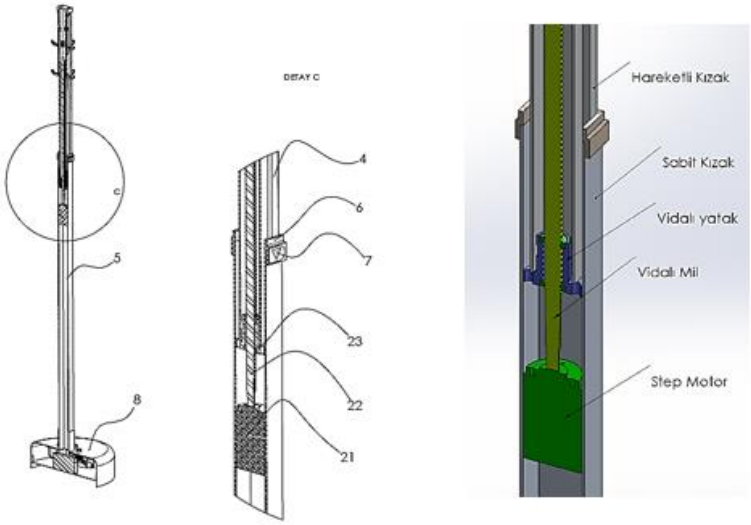


Figure 6. Screw–Nut Drive Mechanism

The components of the mobile lower support assembly, illustrated in a schematic cross-sectional view in Figure 6, are named as follows:

4	Moving Carriage	5	Fixed Carriage
6	Height Adjustment Button Assembly	7	Up/Down Buttons
8	Protective Outer Cover	21	Step motor
22	Lead Screw	23	Lead Nut

3.4. IV Bag Hanger Assembly

This mechanism is located at the top of the IV stand and features a four-arm structure that can be mechanically extended and retracted as required (Figure 7).

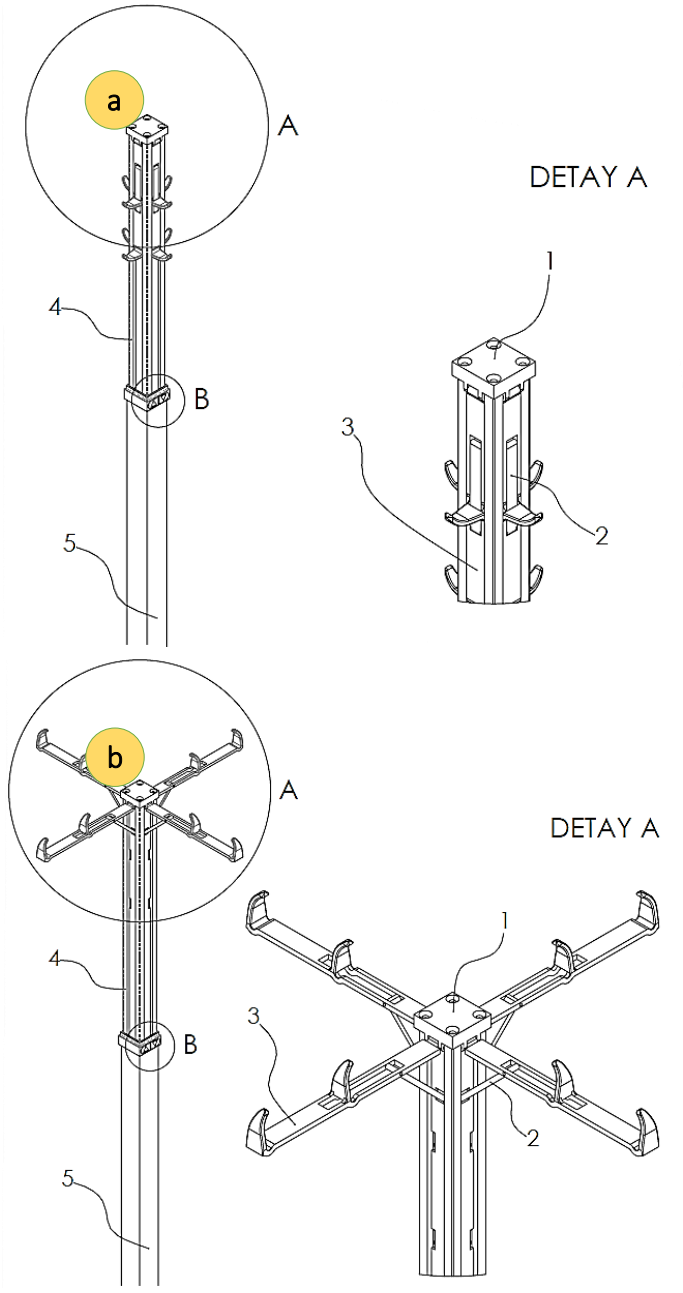


Figure 7. IV Bag Hanger Assembly: (a) Retracted Position; (b) Extended Position

The components of the IV bag hanger assembly, shown in the retracted and exploded views in Figures 7(a) and 7(b), respectively, are named as follows:

1	Top Cover	2	Hanger Mounting Beam
3	IV Bag Hanger	4	Moving Carriage
5	Fixed Carriage		

The IV bag hanger assembly is designed to be extendable and retractable in four different directions as required, with each hanger arm featuring two hanging hooks.

3.5. User Interface and Control

The primary objective of the designed IV stand's user interface and control unit is to enable autonomous movement that does not restrict the patient's mobility, while visually recognizing the patient and following them from a safe distance (e.g., 1–1.5 meters). The core functions for this purpose can be defined as follows:

- Detecting the patient's key points (pose estimation) or face/body using camera-based image processing techniques and artificial intelligence.
- Calculating the distance and angle between the patient and the IV stand.
- Enabling following by sending direction and speed commands to motor drivers.
- Obstacle avoidance (safety layer using ultrasonic/LiDAR sensors).

3.5.1. System Architecture and Operating Principle

The operating principles of the control system to be developed for the IV stand prototype can be broadly defined as follows:

- **Image Acquisition:** The camera transmits the live video stream to the AI processor.
- **Person Detection and Following:** The patient within the frame is detected using YOLOv8-Nano or MediaPipe Pose algorithms, and a bounding box or the body center is calculated.
- **Error Calculation (PID):** Motor direction and speed values (PWM) are generated by calculating the patient's distance from the center (angular error) and magnitude (distance error).
- **Safety Layer:** If the ultrasonic sensors located beneath the IV pole detect an unexpected obstacle, they override the command from the AI and stop the vehicle.

3.5.2. Hardware and Equipment List

Similarly, the list of all equipment designed for the IV stand is provided in Table 2.

Table 2. List of all equipment designed for the IV stand

Component Group	Equipment / Model	Remark / Function	Approximate Number
Artificial Intelligence Processor	Nvidia Jetson Nano (4GB) or Raspberry Pi 4/5	Image processing, execution of the deep learning model	1 Unit
Camera	Intel RealSense D435 (Depth Camera) or Logitech C920 / Pi Camera	Depth sensing (RealSense) or standard USB camera	1 Unit
Motor & Driver	With 12V 100-200 RPM Reducer DC Motor + BTS7960 Motor Driver	Motor and control board with sufficient torque to carry the IV stand	3 Units Motor, 1 Driver
Safety Sensor	HC-SR04 Ultrasonic Sensor or TF-Luna LiDAR	Close-range obstacle detection and emergency stop	3 Units
Power Management	12V LiFePO4 / Li-ion Battery Group + Buck Converter (5V 4A)	Independent/regulated power supply for motors and the processor	1 Packet
Mechanic / Chassis	Round metal/acrylic base, swivel casters, IV stand profile	Body design that keeps the heavy roll center low	1 Sets

3.5.3. Safety, Tip-over, and Risk Analysis

The safety risks and corresponding protective measures for the designed IV stand are outlined as follows:

- **Center of Gravity:** There is a high risk of tipping over because the IV bags are positioned high up; therefore, heavy batteries should be placed in the lower chassis, and the base should have a wide footprint.
- **Emergency Brake:** The system must be equipped with a physical emergency stop button and a hardware-based obstacle sensor at the bottom.
- **Disconnection/Lock-out Condition:** If the patient moves out of the frame, the device must stop immediately and must not perform a random search.

4. CONCLUSION AND EVALUATION

The designed autonomous IV stand, featuring a lower assembly and a height-adjustable lifting system, fully complies with modern medical robotics standards. Thanks to its robust chassis structure, low center of gravity, and lead-screw-driven height adjustment mechanism, the IV stand serves as a prototype designed to offer high stability, independent mobility, and patient safety in clinical settings.

REFERENCES

1. M. Binger, C. Conway, N. Goddard, N. Jacobs, C. Pysher, and E. Whritenor, Autonomous IV Stand (P15073), Rochester Institute of Technology, Rochester, NY, USA, 2015.
2. A. Sayed-Kassem, A. Ghandour, L. Hamawy, and A. Zaylaa, "Cutting-edge robotic intravenous pole: preliminary design and survey in academic medical center in Lebanon," Journal of Biomedical Engineering and Medical Devices, vol. 2, no. 1, 2017
3. J. W. Pryor, "Ambulatory patient support stand," US Patent 4332378A, 1982.
4. G. Jost and C. C. Tseng, "Home care intravenous stand," US Patent 4905944A, 1990.
5. B. J. Kunik, "Pole apparatus for hanging intravenous bags or other similar devices," US Patent 390952S, 2002.
6. M. G. Vignali, Intravenous Stand Design, Worcester Polytechnic Institute, Worcester, MA, USA, 2015.
7. K. L. Kramer and M. W. Weismiller, "Sliding IV pole," US Patent 5407163A, 1995.
8. J. C. Schott, M. D. Schott, and J. D. Fox, "Intravenous stand support assembly," US Patent 6079678A, 2000.
9. Sayed-Kassem, A., Kozah, N., Hajj-Moussa, G., Harb, R., & Zaylaa, A. J. (2020). BMIVPOT, a fully automated version of the intravenous pole: Simulation, design, and evaluation. Journal of Healthcare Engineering, 2020(1), 7963497.
10. Oguri, T., Yokota, S., Matsumoto, A., Chugo, D., Muramatsu, S., & Hashimoto, H. (2021). Development of robotic IV pole moving side by side with human: First report: Design of the first prototype and forward moving experiment. In 2021 14th International Conference on Human System Interaction (HSI) (pp. 240–245). IEEE. https://doi.org/10.1109/HSI52170.2021.9538675
11. Oguri, T., Yokota, S., Matsumoto, A., & Hashimoto, H. (2023). Development of robotic IV pole for reducing risk of falling. The Proceedings of the Conference on Information Intelligence and Precision Equipment, 2023, IIPC-5-26. https://doi.org/10.1299/jsmeiip.2023.IIPC-5-26
12. Castillo, U., Lim, L., Magallon, I., Tabban, A., & Trimble, K. (2023). Patient tracking and following IV pole. UC Irvine, Samueli School of Engineering, Department of Biomedical Engineering. https://escholarship.org/uc/item/3d91f2w1

Chapter 7

GUI-Based Image Processing for Automated Delamination Detection and Quantification in Composite Laminates

Şehmus BADAY[1], Hüseyin GÜRBÜZ[2], Mehmet Emin DEMİR[3]

1. INTRODUCTION

Composite materials are engineered by combining two or more distinct constituents to obtain a set of properties that cannot generally be achieved by the individual constituents alone. Owing to their high specific strength and stiffness, low density, corrosion resistance, and tailorable mechanical behavior, composite materials are extensively used in aerospace, automotive, defense, marine, energy, and sporting applications [1–10]. Nevertheless, their structural reliability is seriously hindered by delamination, a critical damage mechanism that develops beneath the surface to disrupt interlaminar load transfer, diminish load capacity, and jeopardize overall structural integrity. Drilling is frequently required during the final assembly of composite components to accommodate bolts, rivets, and other mechanical fasteners. During drilling, the mechanical action of the cutting tool can generate damage at the hole entrance and exit. Delamination is widely recognized as one of the most critical forms of machining-induced damage in laminated composite materials because it can degrade hole quality and compromise structural integrity. During drilling, the interaction between the cutting tool and the layered structure produces interlaminar stresses that can initiate and propagate separation around the hole. The extent of this damage is governed by a combination of machining parameters, tool geometry, laminate architecture, and material properties. Accurate quantification of delamination is therefore important not only for quality assessment but also for investigating the influence of these parameters on drilling performance. To this end, several geometric indices and inspection methods have been proposed. Geng et al. [11] comprehensively reviewed the formation, evaluation, and suppression of drilling-induced delamination, emphasizing that reliable damage quantification is essential for optimizing composite drilling processes. Advanced

[1] Assoc. Prof. Dr., Beşiri Organized Industrial Zone Vocational School, Mechanical Program, Batman University, Turkey, sehmus.baday@batman.edu.tr, (ORCID: 0000-0003-4208-8779)
[2] Assoc. Prof. Dr., Department of Mechanical Engineering/Faculty of Engineering and Architecture, Batman University, Turkey, huseyin.gurbuz@batman.edu.tr, (ORCID: 0000-0003-1391-172X)
[3] Assoc. Prof. Dr., Beşiri Organized Industrial Zone Vocational School, Textile Technology Program, Batman University, Turkey, memin.demir@batman.edu.tr, (ORCID: 0000-0001-9630-6378)

non-destructive techniques, such as computerized tomography and ultrasonic C-scans employed by Tsao and Hocheng [12], can provide detailed damage profiles. However, their implementation often requires specialized instrumentation and greater experimental resources. These practical considerations have encouraged the development of digital image analysis as a comparatively accessible route for the quantitative evaluation of visible drilling damage. Davim et al. [13] and Nagarajan et al. [14] demonstrated that quantitative damage indices can be obtained directly from acquired images, establishing an important foundation for replacing purely manual geometric measurements with computer-assisted procedures. Furthermore, because drilling-induced damage is generally irregular, a single maximum-diameter measurement may not fully represent the spatial distribution of the damage. Tsao et al. [15] and subsequent studies [16] supported the combined use of diameter- and area-based metrics when assessing complex delamination morphologies. More recently, attention has shifted toward increasing the degree of automation in image-based measurement. De Albuquerque et al. [17] applied artificial neural networks to radiographic images, while Lukacs et al.[18] proposed digital image-processing algorithms, reflecting a broader transition toward automated quantification. Koc[19] developed an image-processing program for automatic delamination calculation, reporting close agreement with ImageJ; however, the method exhibited high sensitivity to brightness and lighting conditions, requiring manual adjustment depending on material type and surface color.

The current literature therefore indicates a clear progression from conventional geometric measurement to digital image processing and, more recently, toward automated damage-detection approaches. However, a practical gap remains between threshold-dependent analysis procedures and more data-intensive intelligent methods. When a large number of experimental images must be evaluated, conventional image-based evaluation still requires repeated manual image inspection, boundary selection, and data recording, which is time-consuming and introduces operator-dependent variability. To address these limitations, this study presents a Python-based graphical user interface (GUI) designed for the automated detection and quantitative assessment of delamination around machined holes in composite materials. The developed framework integrates Hough-based automatic hole detection, image calibration, Morphological Chan-Vese active-contour segmentation, mask refinement, delamination-boundary extraction, calculation of conventional and area-informed delamination factors, visualization, and Excel data export within a single environment. Rather than claiming the complete replacement of expert judgment, the proposed system operates as a hybrid analysis framework. It automates repetitive, time-consuming operations to standardize the evaluation procedure while retaining manual hole definition and damage region selection

alternatives for challenging images where automatic detection is unsuitable. This structure aims to significantly reduce processing time and user-dependent variability, providing an efficient, transparent, and training-data-independent tool for quantitative delamination assessment.

2. DELAMINATION IN COMPOSITE MATERIALS AND ITS ENGINEERING SIGNIFICANCE

2.1. Definition of Delamination

In laminated composites, delamination can be described as separation between adjacent plies or layers. Once separation occurs, interlaminar load transfer is disturbed and the structural integrity of the laminate may be reduced. Delamination may originate from manufacturing defects, impact, fatigue, environmental exposure, or machining operations. During drilling, axial forces can promote interlaminar separation, particularly near the entrance and exit surfaces of the hole. Even when initially localized, delamination may propagate under subsequent service loading. Its detection and quantitative characterization are therefore important for both manufacturing quality and structural reliability.

2.2. Delamination Mechanisms During Drilling

During drilling of composite laminates, cutting forces generate complex stress states within the fibers, matrix, and interlaminar regions. The damage mechanisms at the hole entrance and exit are not identical. At the entrance, the action of the drill may lift the upper plies and initiate interlaminar separation. This mechanism is commonly described as peel-up delamination. Near the exit, the remaining uncut laminate becomes progressively thinner and may no longer withstand the axial thrust force. The lower plies can then be displaced downward and separate, producing push-out delamination. The extent of drilling-induced delamination can be affected by feed rate, cutting speed, drill geometry, tool wear, fiber orientation, laminate stacking sequence, and the mechanical properties of the composite.

2.3. Engineering Significance

Delamination should not be regarded solely as a visual surface defect. Interlaminar separation can modify the effective load-bearing region and local stress transfer around a machined hole. This is particularly important in mechanically fastened joints, where the region surrounding the hole directly participates in load transfer. Accordingly, evaluation and optimization of composite drilling should consider delamination together with other machining responses such as thrust force, surface quality, dimensional accuracy, and tool wear.

3. MEASUREMENT AND QUANTITATIVE EVALUATION OF DELAMINATION

3.1. Image-Based Delamination Analysis

Digital images obtained by optical imaging, scanning, or other inspection techniques can be used to characterize drilling-induced delamination. The essential image-analysis task is to distinguish the nominal hole from the surrounding damaged region and then extract geometric quantities such as the nominal hole diameter, maximum damage diameter, and segmented damage area.

3.2. Conventional Delamination Factor

A commonly used geometric measure expresses delamination as the ratio of the maximum damage diameter to the nominal or detected hole diameter:

$$Fd = D_{max}/D$$

Here, D_{max} denotes the maximum extent of the delaminated region and D denotes the nominal or detected hole diameter. In an ideal undamaged condition, D_{max} approaches D and F_d approaches unity. As damage propagates outward from the hole, D_{max} and consequently F_d increase. The principal advantage of this measure is its simplicity. However, because it is governed by a single maximum dimension, a localized radial extension can increase F_d even when much of the hole perimeter remains relatively undamaged.

3.3. Area-Based Adjusted Delamination Factor

To incorporate information on the spatial extent of the segmented region, the developed software also evaluates an adjusted delamination factor:

$$F_{(da)} = \alpha(D_{max}/D) + (1 - \alpha)(A_d/A_{nom})$$

In this expression, A_d is the area represented by the finalized segmentation mask, A_{nom} is the nominal hole area, and α is a weighting coefficient that controls the relative contribution of the diameter- and area-based terms.

$$A_{(nom)} = \pi(D/2)^2$$

Including an area term allows the analysis to account for geometric information that is not represented by the maximum diameter alone.

3.4. Limitations of Manual Measurement

Manual image-based measurement is practical for a small number of specimens, but its disadvantages become increasingly important as the dataset grows. Each image must be opened, inspected, measured, and recorded individually, creating a repetitive workflow that can require substantial analyst time. Manual definition of the delamination boundary is also inherently dependent on visual judgment, especially for low-contrast images or irregular damage morphologies. Different users may select slightly different boundaries, and the same user may not reproduce exactly the same selection at different times. These considerations motivated the use of image-processing algorithms to standardize repetitive parts of the analysis.

4. IMAGE-PROCESSING-BASED DELAMINATION DETECTION

4.1. Image Acquisition and Pre-processing

The analysis begins by loading a digital image into the software. A color representation is retained for visualization, while a grayscale image is generated for image processing. Grayscale intensity values are rescaled before subsequent detection and segmentation operations.

4.2. Automatic Determination of Hole Geometry

The hole is automatically detected using a Hough-circle-based procedure. The grayscale image is first converted to an 8-bit representation and median filtering is applied to reduce high-frequency noise. Candidate circles are then identified, and when multiple candidates are present, the circle closest to the image center is selected. The procedure returns the hole center and diameter in pixels. If automatic detection is unsuitable, the GUI provides a manual three-point alternative. The user selects three points on the hole boundary and a circle is fitted through those points to obtain the center and diameter.

4.3. Image Calibration

Pixel measurements are converted to physical dimensions using either the known nominal hole diameter or a two-point reference of known physical length. For nominal-diameter calibration, the scale factor C is calculated as:

$$C = D_n / D_p x$$

where D_n is the nominal diameter in millimeters and D_{px} is the detected diameter in pixels. In the two-point method, the user selects the endpoints of a known length and enters its physical dimension, from which the mm/pixel scale is determined.

4.4. Automatic Segmentation of the Delamination Region

The primary automatic segmentation method is a morphological Chan–Vese active-contour procedure. A circular initial level set is generated around the detected hole center, with a seed radius defined relative to the detected hole diameter. The active contour is then evolved for a user-defined number of iterations; the default value in the GUI is 150.

The resulting mask is checked using simple geometric conditions. If the initial segmentation is considered unsuitable, an alternative path based on adaptive Gaussian thresholding followed by morphological closing is applied. A geometric fallback mask is also available when the segmented region does not satisfy the internal checks.

4.5. Mask Refinement and Boundary Extraction

The raw damage mask is combined with the nominal hole disk, internal holes are filled, and only the connected component containing the detected hole center is retained. This step reduces the influence of unrelated image regions. The outer contour of the finalized mask is subsequently extracted and used as the delamination boundary.

4.6. Determination of Maximum Damage Diameter

To determine D_{max}, the convex hull of the extracted boundary points is formed and pairwise Euclidean distances between hull points are evaluated. The largest distance is taken as the maximum damage diameter. This procedure is useful for irregular and directionally extended damage because it is not restricted to a single horizontal or vertical measurement.

4.7. Manual Damage-Region Definition

For images in which automatic segmentation is not satisfactory, the GUI provides a manual polygon mode. The user selects multiple points along the perceived damage boundary, and the resulting polygon is converted to a binary mask. This option preserves expert intervention and allows the analysis to continue when automatic segmentation is challenged by image quality or complex morphology.

5. DESIGN AND OPERATING PRINCIPLE OF THE DEVELOPED GUI

5.1. Software Architecture and Libraries

The application was implemented in Python. OpenCV and scikit-image are used for image-processing operations, NumPy and SciPy support numerical and geometric calculations, Tkinter provides the graphical user interface, and Matplotlib is

embedded for image display and graphical overlays. Pandas and openpyxl support tabular data handling and Excel export.

5.2. General GUI Structure

The main window is organized around the sequence of the analysis. The image canvas occupies the main visualization area, while the control panel contains dedicated sections for calibration, hole detection, damage-region definition, calculation of results, and the accumulated results table. Figure 1 shows the main interface of the developed GUI during delamination analysis. The interface combines image loading and batch processing with calibration, automatic or manual hole detection, damage-zone segmentation, numerical calculation, and result visualization in a single environment. The analyzed image is displayed centrally, while the calibration, detection, segmentation, and calculation controls are arranged in the right-hand panel.

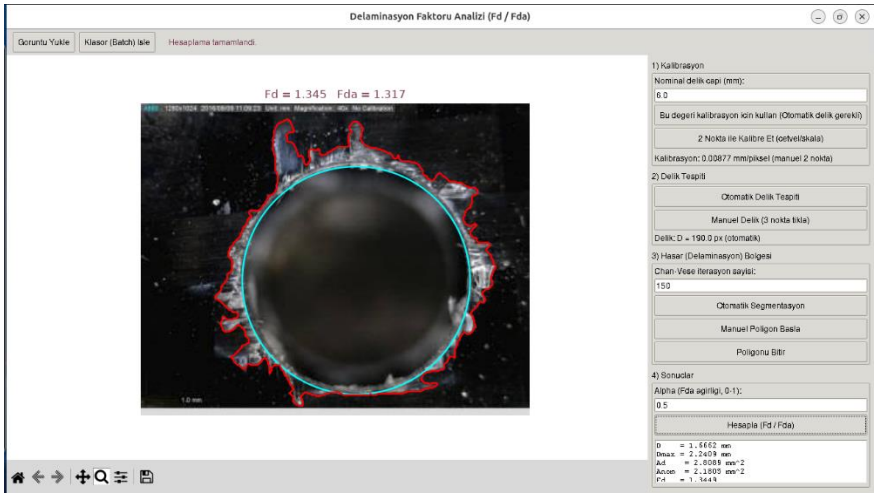


Figure 1. Main interface of the developed GUI for delamination-factor analysis.

The analyzed image is displayed with the nominal hole boundary (cyan) and detected damage-zone boundary (red), while calibration, hole detection, segmentation, and numerical result controls are provided in the interface.

5.3. Single-Image Analysis Workflow

For a single image, the user loads an image, detects the hole automatically or manually, performs calibration, defines the damage region using automatic segmentation or a manual polygon, and then calculates the geometric quantities and

delamination factors. The detected hole and damage boundary are overlaid on the image so that the result can be visually inspected before being saved.

5.4. Calculation and Display of Results

After the finalized damage mask has been obtained, the software calculates D, D_{max}, A_d, A_{nom}, F_d, and F_{da}. These quantities are displayed in the GUI and the current image is annotated with the calculated delamination-factor values.

A representative annotated output generated by the GUI is presented in Figure 2. For this example, the nominal hole boundary is indicated by the cyan circle and the detected delamination boundary by the red contour. The GUI simultaneously reports the calculated conventional delamination factor (F_d = 1.345) and adjusted delamination factor (F_{da} = 1.317), allowing the detected damage morphology and the corresponding quantitative indices to be evaluated together.

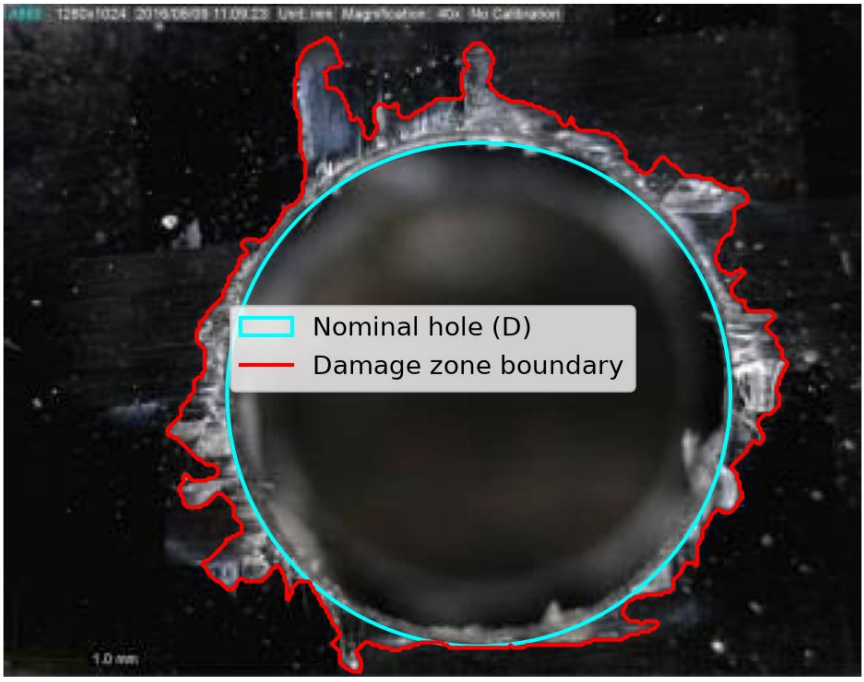


Figure 2. Representative GUI output for Trial_1.

The cyan circle denotes the nominal hole boundary (D), the red contour denotes the detected damage-zone boundary, and the calculated values are F_d = 1.345 and F_{da} = 1.317. The example illustrates how the software converts the segmented damage geometry into an immediately interpretable visual and numerical output. Irregular damage extensions around the hole are retained in the detected boundary, while the

nominal hole remains separately identified for calculation of the delamination indices. This visualization also enables the user to inspect the automatic result before saving or exporting the measurement.

5.5. Saving and Exporting Results

Each analysis can be associated with a specimen identifier. The result is added to an internal table, while an annotated PNG image is saved for visual documentation. Accumulated results can subsequently be exported to an Excel workbook.

5.6. Batch Processing

A batch-processing mode is included for datasets containing multiple images. The user selects a folder, after which supported image files are processed sequentially. For each image, the software performs automatic hole detection, calibrates the image from the nominal diameter, automatically segments the damage region, calculates the geometric parameters and delamination factors, saves an annotated image, and writes the numerical results to a common Excel file. A sample Excel output generated by the program is presented in Figure 3.

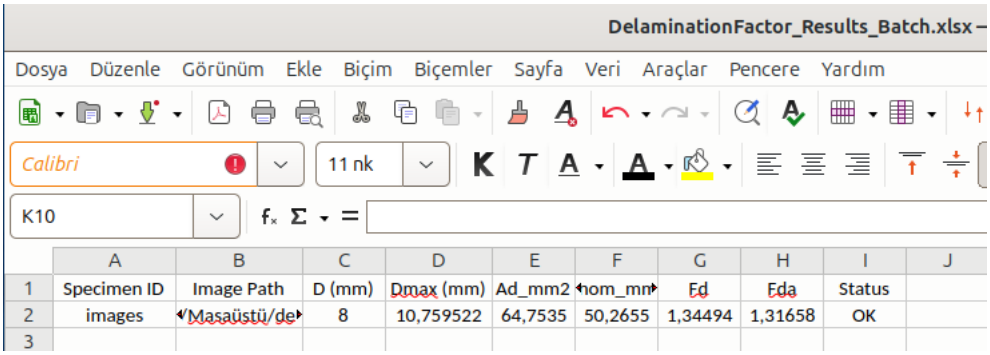


Figure 3. Excel output

Batch processing directly addresses one of the main motivations for developing the application: reducing the repeated manual actions required when a large experimental image set must be evaluated. Nevertheless, the annotated output images should be inspected to identify cases in which automatic detection or segmentation may have failed. Figure 4 shows Workflow of the GUI-based delamination analysis for composite holes, including single-image analysis and automatic batch processing.

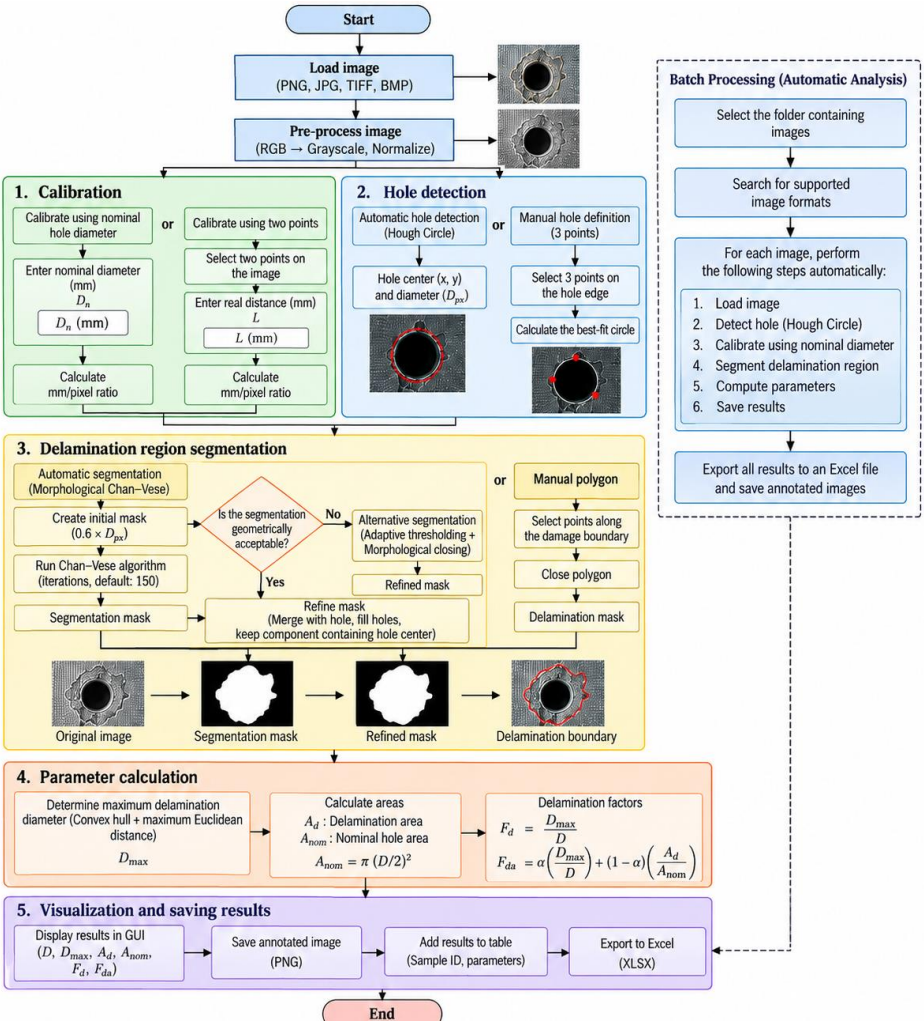


Figure 4. Workflow of the GUI-based delamination analysis

Algorithm 1. GUI-based delamination analysis procedure

Input: composite-hole image; nominal hole diameter or known calibration length; weighting coefficient α; segmentation iteration count.

1. Load the image and generate the grayscale normalized representation.

2. Detect the hole automatically using the Hough Circle Transform; if required, determine the hole from three manually selected boundary points.

3. Convert pixel dimensions to physical units using nominal-diameter or two-point calibration.

4. Segment the delamination region using Morphological Chan–Vese; if the internal geometric checks fail, apply adaptive Gaussian thresholding and morphological closing.

5. Combine the segmented mask with the hole disk, fill internal holes, and retain the connected component containing the hole center.

6. Extract the damage boundary, form its convex hull, and calculate the maximum pairwise Euclidean distance D_{max}.

7. Calculate D, D_{max}, A_d, A_{nom}, F_d, and F_{da}.

8. Display the detected boundaries and numerical results; save the annotated image and export accumulated results to Excel.

Output: calibrated geometric measurements, delamination factors, annotated image, and tabulated results.

6. VALIDATION AND PERFORMANCE EVALUATION

6.1. Time-Efficiency Assessment

To quantify the practical time advantage of the developed GUI, the analysis duration was recorded during 24 consecutive manual delamination measurements. Manual boundary selection and area measurements were conducted pixel-by-pixel using the standard polygon and measurement tools in image analysis software to ensure high precision. The first measurement required 81 s and included the initial system setup, determination of the measurement configuration, adjustment of the required settings, and operator familiarization. Therefore, this first measurement reflects both setup and learning effects in addition to the actual analysis time. Across all 24 manual measurements, the mean analysis time was 45.54 ± 9.91 s (median: 42.5 s; range: 36–81 s; CV: 21.8%). When the first setup/familiarization measurement was excluded, the mean duration for measurements 2–24 decreased to 44.00 ± 6.56 s. The later measurements showed a substantially narrower time distribution; measurements 11–24 required 40.36 ± 2.92 s on average (CV: 7.2%), indicating that the manual procedure approached a more stable operating range after the initial familiarization period.

In contrast, GUI-based analysis required approximately 20 s per image under the current test conditions. Relative to the overall mean manual analysis time of 45.54 s, this corresponds to an estimated time reduction of approximately 56% and an approximately 2.3-fold increase in analysis speed. These results demonstrate the substantial potential of the developed GUI to reduce the time required for repetitive delamination measurements.

The time-saving percentage was calculated as:

$$T_s(\%) = [(t_manual - t_GUI)/t_manual]x100$$

where t_{manual} is the manual analysis time and t_{GUI} is the GUI-based analysis time. Because the current GUI duration represents an approximate average value rather than individually recorded times for all 24 images, the time-efficiency result should be interpreted as an estimate. Image-by-image GUI timing in future validation would enable paired statistical comparison and a more rigorous assessment of processing-time variability.

Table 1. Time-efficiency comparison between manual and GUI-based delamination analysis.

Metric	Manual analysis	GUI analysis	Interpretation
Number of measurements	24	Approx. mean timing	Manual series recorded consecutively
Mean analysis time	45.54 s	20 s	≈56% time reduction
Manual median	42.5 s	—	Robust central tendency
Manual range	36–81 s	—	Includes setup/learning effect
Estimated speed increase	Reference	≈2.3× faster	Based on overall manual mean

6.2. Manual versus GUI-Based Measurements

Compare manual/reference measurements with GUI outputs for D_{max}, A_d, F_d, and F_{da}. A possible absolute percentage error measure is:

$$E(\%) = [(X_GUI - X_ref)/X_ref]x100$$

6.3. Analysis-Time Comparison

Measure the time required to analyze the same images manually and using the GUI. A possible time-saving metric is:

$$T_s(\%) = [(t_m - t_a)/t_m] \times 100$$

6.4. Repeatability and Operator Variability

If possible, repeat manual measurements by the same operator and by multiple operators. Report descriptive statistics and an appropriate repeatability or variability analysis. A simple coefficient of variation may be reported as:

$$CV(\%) = (s/\bar{x}) \times 100$$

6.5. Segmentation Accuracy

If expert reference masks are available, compare the automatic segmentation with those masks using overlap metrics such as Intersection over Union (IoU) and the Dice similarity coefficient:

$$IoU = \left|M_{Gui} \cap M_{ref}\right| / \left|M_{Gui} \cup M_{ref}\right|$$
$$Dice = 2\left|M_{Gui} \cap M_{ref}\right| / \left(\left|M_{Gui}\right| + \left|M_{ref}\right|\right)$$

7. ADVANTAGES AND LIMITATIONS OF THE DEVELOPED APPROACH

The developed GUI integrates image loading, calibration, hole detection, segmentation, geometric measurement, delamination-factor calculation, visualization, and data export within one software environment. This reduces the need to transfer measurements manually between multiple programs. Batch processing is particularly useful for experimental studies containing many images because the same computational procedure can be applied sequentially and the results can be stored in a common data structure. Another advantage is the combination of automatic and manual modes. When Hough-based hole detection or Chan–Vese segmentation is unsuitable, the user can define the hole using three points or delineate the damage region with a polygon. The system therefore functions as a hybrid analysis platform rather than a fully automatic black box.

The method nevertheless has limitations. Automatic segmentation can be affected by image contrast, illumination, resolution, surface texture, and the visual distinction between damaged and intact regions. Hough-circle detection can also be sensitive to the visibility and circularity of the hole boundary. Because area-based measurements are sensitive to the segmented boundary, image-acquisition conditions should be standardized as far as practicable. The algorithm and its parameters should also be validated before the software is applied to different composite systems, hole sizes, imaging arrangements, or damage morphologies.

8. CONCLUSIONS AND FUTURE WORK

A Python-based graphical user interface was developed to facilitate image-based evaluation of drilling-induced delamination in composite materials. The application integrates image loading, calibration, hole detection, damage segmentation, geometric analysis, calculation of delamination factors, visualization, and data export.

The implemented workflow combines Hough-circle-based hole detection, morphological Chan–Vese segmentation, mask refinement, and geometric determination of the maximum damage extent. Manual hole and polygon-selection options are retained to support cases in which automatic analysis is unsuitable. The software calculates both the conventional delamination factor F_d and an area-informed adjusted factor F_{da}, while also reporting the associated geometric quantities in physical units after calibration. Annotated images and numerical results can be saved for subsequent analysis. The batch-processing mode provides a practical route for reducing repetitive user actions in studies containing many images. However, the quantitative benefit in analysis time, measurement agreement, and repeatability must be established through the validation study described in Section 6.

Future work may investigate machine-learning or deep-learning segmentation methods, provided that sufficiently large and appropriately labeled datasets are available. Additional descriptors such as damage orientation, circumferential distribution, local radial extension, and morphological features could also be integrated to extend the GUI from a delamination-factor calculator toward a broader composite-damage analysis platform.

REFERENCES

1. Chen, Hongda, Wang, Jihui, Colin, David, Li, Shuxin, and Drechsler, Klaus (2023) Temperature-Dependent modelling of tension, in-Plane shear, and bending behaviour in non-isothermal thermo-Stamping process simulation of unidirectional UHMWPE fibre reinforced thermoplastic TPU composites. *Journal of Thermoplastic Composite Materials*. 36 (10), 3891–3918.
2. Cao, D., Hu, H., Duan, Q., Song, P., and Li, S. (2019) Experimental and three-dimensional numerical investigation of matrix cracking and delamination interaction with edge effect of curved composite laminates. *Composite Structures*. 225 111154.
3. Ji, D., Li, W., Liu, Z., Liu, H., Gao, F., Wang, M., et al. (2025) Quantitative stiffness evaluation and damage mechanism investigation in open-hole composites via multi-modal SHM data fusion. *Mechanical Systems and Signal Processing*. 237 112998.
4. Pillai, U., Triantafyllou, S.P., Essa, Y., and de la Escalera, F.M. (2020) An anisotropic cohesive phase field model for quasi-brittle fractures in thin fibre-reinforced composites. *Composite Structures*. 252 112635.
5. Adams, M., Huijer, A., Kassapoglou, C., Vaders, J.A.A., and Pahlavan, L. (2024) In Situ Non-Destructive Stiffness Assessment of Fiber Reinforced Composite Plates Using Ultrasonic Guided Waves. *Sensors*. 24 (9), 2747.
6. Bu, F., Wei, W., Wang, X., Li, X., Shen, G., Ma, C., et al. (2025) Weakening Detection of Composite Structure Adhesive Layer Based on Nonlinear Guided Waves. *Applied Sciences*. 15 (4), 1836.
7. Xiao, W., Sha, G., Lu, X., Zuo, H., Cao, M., Soman, R., et al. (2024) Experimental and numerical studies on compressive failure behaviors of stepped-scarf repaired composite stiffened panels. *Engineering Failure Analysis*. 163 108458.
8. Hassani, S., Mousavi, M., and Gandomi, A.H. (2022) Damage detection of composite laminate structures using VMD of FRF contaminated by high percentage of noise. *Composite Structures*. 286 115243.
9. Cao, D., Hu, H., Wang, Y., and Li, S. (2021) Experimental and numerical studies on influence of impact damage and simple bolt repair on compressive failure of composite laminates. *Composite Structures*. 275 114491.
10. Zhang, Y., Han, X., Liu, R., Li, R., Zhong, Y., Cao, D., et al. (2024) Effect of temperature aging of thermoset UD prepregs on inter-ply friction behavior and formability in prepreg compression molding process. *Polymer Composites*. 45 (9), 7861–7878.
11. Geng, D., Liu, Y., Shao, Z., Lu, Z., Cai, J., Li, X., et al. (2019) Delamination

formation, evaluation and suppression during drilling of composite laminates: A review. *Composite Structures*. 216 168–186.

12. Tsao, C.C. and Hocheng, H. (2005) Computerized tomography and C-Scan for measuring delamination in the drilling of composite materials using various drills. *International Journal of Machine Tools and Manufacture*. 45 (11), 1282–1287.
13. Davim, J.P., Rubio, J.C., and Abrao, A.M. (2007) A novel approach based on digital image analysis to evaluate the delamination factor after drilling composite laminates. *Composites Science and Technology*. 67 (9), 1939–1945.
14. Nagarajan, V.A., Selwin Rajadurai, J., and Annil kumar, T. (2012) A digital image analysis to evaluate delamination factor for wind turbine composite laminate blade. *Composites Part B: Engineering*. 43 (8), 3153–3159.
15. Tsao, C.C., Kuo, K.L., and Hsu, I.C. (2012) Evaluation of a novel approach to a delamination factor after drilling composite laminates using a core–saw drill. *The International Journal of Advanced Manufacturing Technology*. 59 (5), 617–622.
16. Silva, D., Pamies Teixeira, J., and Machado, C.M. (2014) Methodology analysis for evaluation of drilling-induced damage in composites. *The International Journal of Advanced Manufacturing Technology*. 71 (9), 1919–1928.
17. De Albuquerque, Victor Hugo C, Tavares, João Manuel R S, and Durão, Luís M P (2010) Evaluation of Delamination Damage on Composite Plates using an Artificial Neural Network for the Radiographic Image Analysis. *Journal of Composite Materials*. 44 (9), 1139–1159.
18. Lukács, T., Pereszlai, C., Magyar, G., and Geier, N. (2023) Drilling-induced delamination measurement using a novel digital image processing algorithm. *Procedia CIRP*. 118 828–832.
19. KOÇ, Savaş (2025) Development of a program for automatic calculation of the delamination factor using image processing techniques. *Journal of Composite Materials*. 59 (28), 3201–3214.

Chapter 8

Microstructural Engineering of Fiber Modified Thermoplastic Composites for Lightweight Aerospace Components

Mehmet AKKAŞ[1]

1. INTRODUCTION

The development of advanced materials for aerospace engineering requires a careful balance between structural efficiency, manufacturing feasibility, operational reliability, and economic considerations. In modern aircraft and unmanned aerial systems, material selection is increasingly guided by the ability to achieve functional performance without introducing unnecessary mass or manufacturing complexity [1]. Although conventional metallic materials continue to provide reliable solutions for numerous aerospace components, polymer-based materials have created additional opportunities for lightweight construction, geometrical flexibility, and the integration of multiple functions within individual components [2]. Within this context, engineering thermoplastics represent an important category of materials whose characteristics can be tailored through the incorporation of suitable reinforcement phases. Their potential is particularly relevant to components where mechanical integrity, environmental resistance, and dimensional accuracy must be achieved under practical manufacturing conditions [3,4]. A significant advantage of thermoplastic-based materials lies in the relationship between their molecular structure and processing behavior. Unlike permanently crosslinked polymer networks, thermoplastic matrices can undergo physical transitions that permit shaping and, under appropriate conditions, subsequent reprocessing [5]. This characteristic offers considerable flexibility in component manufacturing, material recovery, and product development. Nevertheless, the engineering performance of a thermoplastic cannot be evaluated independently of its molecular architecture, thermal response, and interaction with reinforcing constituents. Differences in polymer-chain mobility, crystallinity, intermolecular interactions, and sensitivity to processing conditions can produce substantially

[1] Assoc. Prof. Dr., Istiklal Science and Technology University, Faculty of Engineering, Architecture and Design, Department of Mechanical Engineering, Kahramanmaraş, 46100, Turkey; mehmetakkas@istiklal.edu.tr, (ORCID: 0000-0002-0359-4743)

different mechanical responses, even when similar reinforcement strategies are employed. Consequently, the development of fiber-modified thermoplastics requires an understanding of both the inherent characteristics of the polymer matrix and the structural changes introduced during composite fabrication [6].

Polytetrafluoroethylene (PTFE), polyamide (PA), acrylonitrile butadiene styrene (ABS), and polycarbonate (PC) provide a particularly interesting basis for investigating these relationships because they represent distinct polymer structures and engineering characteristics. PTFE is distinguished by its fluorinated molecular structure, chemical stability, and favorable tribological behavior, although its extremely high melt viscosity imposes specific manufacturing requirements. Polyamide exhibits a combination of mechanical strength and toughness, with properties that can be influenced by moisture absorption and molecular organization. ABS, characterized by its multiphase polymer structure, offers a useful combination of impact resistance and manufacturing versatility [7,8]. Polycarbonate is recognized for its toughness, dimensional stability, and engineering applicability where resistance to mechanical damage is important. These differences create an opportunity to investigate how the effectiveness of fiber reinforcement changes according to the physical and chemical characteristics of the surrounding polymer. They also highlight the importance of considering each material's processing limitations when establishing meaningful comparisons [9].

The incorporation of fibrous reinforcements provides an additional level of control over the mechanical behavior of polymer systems. Glass and carbon fibers are especially relevant because their mechanical characteristics, density, surface properties, and economic implications differ considerably. Glass fibers offer an established reinforcement option for applications requiring a balance between mechanical performance and material cost. Carbon fibers provide a high elastic modulus and favorable specific mechanical properties, making them attractive where structural efficiency is an important design consideration. However, the mechanical contribution of either reinforcement depends on more than its intrinsic strength or stiffness. Effective reinforcement requires the surrounding polymer to transfer applied stresses to the fibers, while the internal structure must remain sufficiently uniform to prevent premature damage initiation. Fiber distribution, orientation, retained length, surface compatibility, and local matrix deformation therefore influence the mechanical behavior of the final composite. Particular attention should be given to reinforcement at relatively low concentrations [10,11]. In highly filled composite systems, the reinforcing phase may contribute substantially to the overall stiffness, whereas materials containing small fiber fractions can remain strongly influenced by the characteristics of the

polymer matrix. Under such conditions, the introduction of a limited amount of reinforcement may alter local deformation behavior, resistance to indentation, and the development of microscopic damage without necessarily producing large changes in all mechanical properties. The effectiveness of reinforcement is consequently related to the balance between localized strengthening mechanisms and the potential formation of structural discontinuities [12]. Poor fiber distribution, inadequate wetting, and weak interfacial interaction may introduce sites of stress concentration that counteract the expected benefits of reinforcement. Evaluating low fiber contents is therefore valuable for determining whether measurable improvements can be achieved while retaining the processing advantages and inherent characteristics of the original polymer.

The manufacturing stage represents a critical link between material formulation and final performance. During composite preparation, thermal exposure, mechanical mixing, and shaping conditions can influence the distribution and physical integrity of the reinforcement. The magnitude of these effects depends on the rheological behavior of the matrix and its response to the selected manufacturing route. For this reason, a processing procedure suitable for one engineering thermoplastic may not provide equivalent material quality when applied to another [13]. Establishing matrix-specific preparation conditions is particularly important when comparing polymers with markedly different melt-flow characteristics. Furthermore, the relationship between processing and mechanical response cannot be adequately understood through macroscopic measurements alone. Scanning electron microscopy (SEM) provides complementary information on fiber distribution, fracture-surface characteristics, interfacial separation, and localized defects. When interpreted together with mechanical measurements, these observations can help identify the structural features associated with differences in composite performance [14].

From an aerospace engineering perspective, the value of fiber-reinforced thermoplastics should also be considered in relation to the intended function of the component. Materials suitable for protective covers, equipment enclosures, internal fittings, and selected secondary structures may be subject to different performance requirements than those used in primary load-bearing assemblies. Accordingly, the selection of a reinforced polymer should not be based exclusively on a single mechanical property [15]. Manufacturing constraints, expected service conditions, component geometry, damage mechanisms, and economic feasibility must also be considered. A comparative evaluation of different polymer–fiber combinations can provide useful preliminary evidence for identifying promising material systems and determining where further investigation is necessary. Such an approach is particularly valuable during early-

stage material development, before undertaking more demanding assessments involving fatigue, impact loading, thermal cycling, or environmental exposure [16-18].

Against this background, the present study investigates the influence of glass and carbon fiber incorporation on the mechanical and microstructural characteristics of four engineering thermoplastics: PTFE, PA, ABS, and PC. Unreinforced materials are considered alongside formulations containing 0.5, 1.0, and 2.0 wt.% of the respective fiber types, enabling the effects of matrix selection, reinforcement identity, and fiber concentration to be examined within a common comparative framework. Material preparation is approached according to the processing requirements of each polymer, while mechanical characterization and SEM observations are used to investigate the relationship between reinforcement incorporation and the resulting material characteristics [19-21]. Rather than assuming a universal strengthening effect, the investigation seeks to identify the extent to which the response to glass or carbon fiber reinforcement depends on the selected thermoplastic matrix. The resulting evaluation is intended to contribute to the understanding of composition-dependent behavior in engineering thermoplastic composites and to support preliminary material selection for lightweight aerospace-related components [22].

2. EXPERIMENTAL METHOD AND PROCESSING

The experimental investigation was structured around four commercially relevant engineering polymers, namely polytetrafluoroethylene (PTFE), polyamide (PA), acrylonitrile butadiene styrene (ABS), and polycarbonate (PC). These materials were selected to represent thermoplastic systems with different molecular structures, processing characteristics, and mechanical responses. Two fibrous reinforcement materials, glass fiber (GF) and carbon fiber (CF), were incorporated independently into the polymer matrices to investigate the influence of reinforcement chemistry on composite behavior. A systematic compositional approach was adopted to distinguish the effects of polymer identity, fiber selection, and reinforcement concentration. For each thermoplastic, three reinforcement fractions corresponding to 0.5, 1.0, and 2.0 wt.% were considered for both GF and CF. Reference specimens without fibrous additions were also included to establish the baseline behavior of the individual polymers. Accordingly, the experimental design comprised 28 nominal material compositions, consisting of four unreinforced polymer systems and 24 fiber-containing formulations. Reinforcement percentages were calculated relative to the total mass of each prepared composition. This arrangement enabled direct

comparisons between the two reinforcement systems at equivalent nominal concentrations while accounting for the different characteristics of the polymer matrices.

The preparation of the fiber-modified thermoplastics involved a sequence of material blending, thermal processing, and specimen shaping operations. For the conventionally melt-processable polymer systems, extrusion compounding was employed to promote the incorporation of reinforcing fibers into the thermoplastic matrices. The extrusion equipment was configured with five independently regulated heating zones, allowing the temperature distribution along the processing barrel to be controlled through a programmable logic controller. Thermal conditions were selected with consideration of the processing requirements of the individual polymer matrices. During extrusion, the combined action of temperature and mechanical shear facilitated the movement and redistribution of the fibrous phase within the softened polymer. Since the constituent materials differed in rheological behavior, the processing conditions required consideration of the individual matrix characteristics rather than assuming identical thermal conditions for all formulations. The resulting extruded material was cooled and converted into pellets, providing a feedstock suitable for subsequent specimen preparation. The potential influence of mechanical shear on fiber integrity was also considered when interpreting the microstructural characteristics of the manufactured composites. For PA-, ABS-, and PC-based compositions, the compounded pellets were subsequently shaped using injection molding. This manufacturing stage enabled the preparation of test specimens from the previously compounded materials. The molding process was governed by controlled thermal and pressure conditions, with particular consideration of the polymer-specific flow and solidification behavior. Specimen fabrication was intended to provide sufficiently consistent geometries for comparative characterization.

Scanning electron microscopy (SEM) was employed to investigate the internal morphological characteristics of the composite materials and to support the interpretation of their mechanical behavior. Examination of representative specimen surfaces provided information regarding the distribution of reinforcing fibers, the continuity of the polymer phase, and the local interaction between the constituent materials. Microstructural observations focused on features relevant to composite integrity, including fiber-rich regions, reinforcement separation, interfacial discontinuities, and the presence of pores or other processing-related defects. Where fracture surfaces were available, additional attention was given to matrix deformation, fiber exposure, and possible fiber pull-out characteristics. These features were considered useful indicators of the local response of the

composite structure under mechanical loading. The microstructural evaluation was integrated with the hardness comparisons to examine possible relationships between local material morphology and measured mechanical response. Particular attention was directed toward determining whether variations in reinforcement concentration were accompanied by observable differences in fiber distribution or defect formation. This combined characterization approach provided a basis for evaluating the compatibility of the selected fibers with the individual thermoplastic matrices and for discussing their potential use in lightweight aerospace-related components.

3. FINDINGS AND DISCUSSIONS

The morphological evaluation of the developed thermoplastic composites provided important information regarding the influence of reinforcing fibers on the structural characteristics of the polymer matrices. Scanning electron microscopy (SEM) was used to investigate the morphological differences associated with glass fiber (GF) and carbon fiber (CF) incorporation. The microstructural features observed in the examined specimens indicated that the internal structure of the composites was influenced by the interaction between the reinforcement phase and the surrounding polymer. These characteristics are particularly important for understanding the potential mechanical behavior of fiber-modified engineering thermoplastics [23-25]. The SEM micrographs presented in Figures 1–3 illustrate representative morphological characteristics of the investigated materials. Examination of the polymer regions indicated that the reinforcement process modified the internal morphology compared with that of the unreinforced material. The reference polymer exhibited a relatively continuous surface structure, whereas the addition of fibers introduced morphological discontinuities associated with the presence of reinforcement and the development of fiber–matrix boundaries [26]. These changes resulted in more heterogeneous surface characteristics, reflecting the coexistence of polymer-rich and reinforcement-containing regions. The reinforcing constituents were generally distributed within the examined polymer regions, suggesting that the adopted material preparation procedures enabled the incorporation of fibers into the thermoplastic matrices. However, the observed distribution was not completely uniform in every region. Local differences in reinforcement concentration and orientation were evident, demonstrating the importance of processing conditions in determining the final composite morphology. Such variations can influence the distribution of local stresses and the mechanical response of the material, particularly where the reinforcement arrangement creates differences in structural continuity [27].

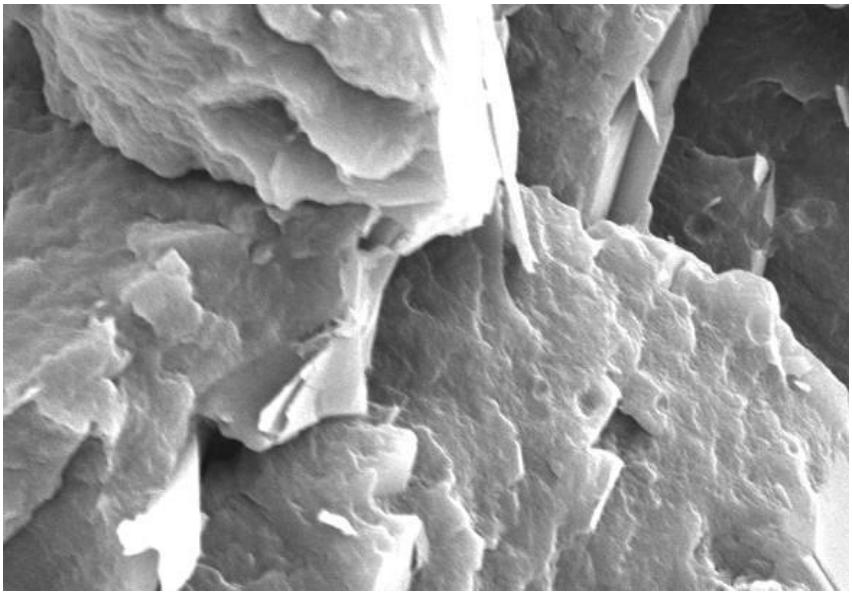


Figure 1. SEM micrograph of Sample 1.

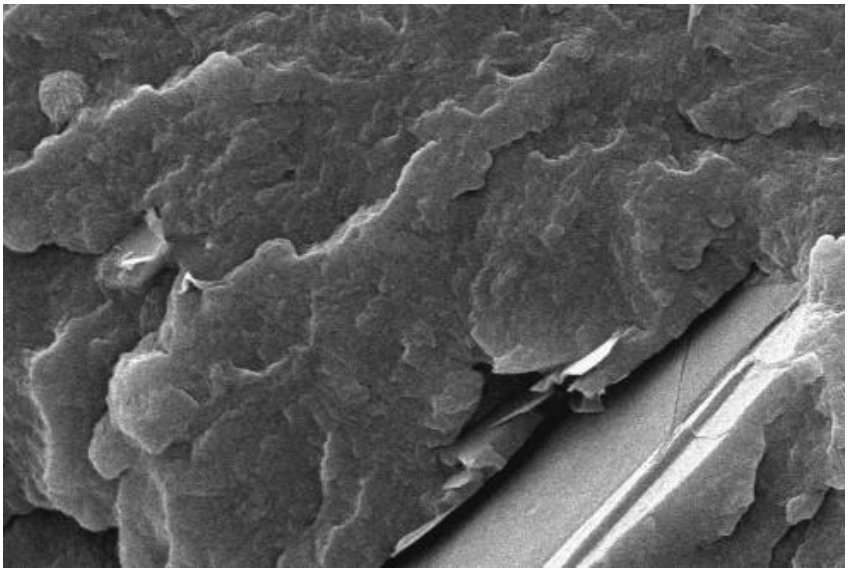


Figure 2. SEM micrograph of Sample 2.

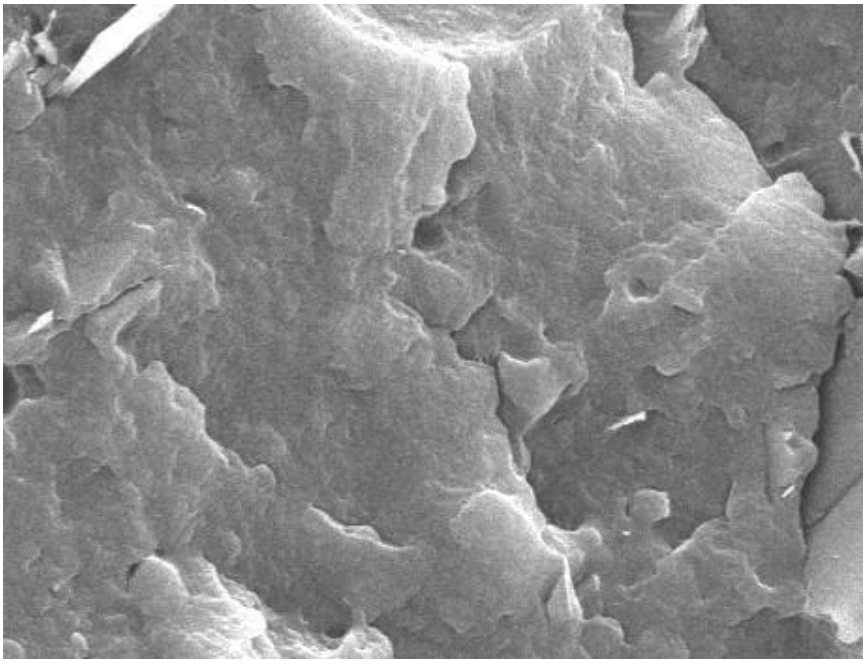


Figure 3. Representative SEM micrograph of Sample 3.

The microstructural response of the thermoplastic systems was also influenced by the concentration of the reinforcing phase. The investigated compositions contained relatively small quantities of glass or carbon fibers, corresponding to 0.5, 1.0, and 2.0 wt.%. Within this concentration range, the polymer matrix remained the principal constituent of the composite, while the fibers introduced localized regions with different morphological and mechanical characteristics. At relatively low reinforcement concentrations, the SEM observations indicated that individual fibers could be accommodated within the surrounding polymer with comparatively limited local accumulation. The continuity of the matrix around the reinforcing phase is an important structural characteristic because it determines the extent to which the polymer can support and interact with the incorporated fibers [28]. Regions exhibiting close contact between the two constituents may provide favorable conditions for mechanical interaction, although the actual strength of the interface cannot be established from morphological observations alone [29].

Increasing the reinforcement fraction introduced a greater number of fiber-containing regions within the polymer structure. This change affected the spatial arrangement of the reinforcing phase and increased the complexity of the local microstructure. In certain examined regions, differences in fiber orientation and localized reinforcement accumulation became more apparent. These observations

suggest that the relationship between fiber concentration and composite quality is not governed exclusively by the quantity of reinforcement introduced into the matrix [30]. The formation of fiber-rich regions can create local differences in deformation behavior, particularly when neighboring fibers are separated by relatively thin polymer layers. Furthermore, the presence of interfacial gaps or small cavities can influence the integrity of the surrounding material. Therefore, increasing the amount of reinforcement does not necessarily produce a proportional improvement in mechanical performance. The microstructural characteristics observed in this investigation emphasize the need to consider reinforcement concentration together with fiber distribution and matrix continuity when assessing composite formulations. Some examined surfaces displayed evidence of fiber pull-out, characterized by the partial removal or separation of reinforcing fibers from the surrounding polymer. This morphology indicates that interfacial separation occurred during the deformation or fracture process. Such features may result from limited adhesion, differences in the deformation characteristics of the constituents, or stresses developed during mechanical loading [31]. Nevertheless, fiber pull-out should not be interpreted as evidence of poor adhesion in isolation, since its occurrence is also affected by fiber geometry, orientation, and the local fracture mechanism.

Other regions exhibited fibers retained within the surrounding polymer, including fractured reinforcement segments. These observations indicate that different local failure mechanisms may coexist within the same composite system. Fiber fracture can occur when the stresses acting on a reinforcing filament become sufficiently high, while interfacial separation may develop when the local resistance to debonding is exceeded. Consequently, the relative occurrence of these morphological features provides qualitative insight into the mechanical interaction between the reinforcement and matrix. The examination also identified small voids and discontinuities in selected regions. Such features may originate from incomplete polymer penetration around the reinforcement, local processing irregularities, or damage generated during specimen fracture [32]. Their presence is relevant because internal cavities and interfacial defects can modify stress distribution and promote localized deformation. However, their precise origin cannot be determined from SEM images alone. Overall, the observed fracture-related characteristics demonstrate that composite integrity depends on the combined behavior of the fiber, matrix, and their interface. The presence of multiple morphological features also highlights the complexity of damage development in thermoplastic composites, where localized plastic deformation, interfacial separation, and reinforcement fracture may contribute differently depending on the material combination.

The use of two chemically and mechanically distinct reinforcement materials provided an opportunity to examine differences in the microstructural response of the investigated thermoplastics. Glass and carbon fibers possess different intrinsic properties and surface characteristics, which may influence their interaction with the selected polymer matrices. In the glass-fiber-containing specimens, the reinforcement phase was distinguishable from the surrounding polymer through its characteristic morphology and fiber–matrix boundaries. The examined regions showed that glass fibers contributed to the development of a heterogeneous structure in which local reinforcement orientation and interface characteristics varied across the observed surfaces. The quality of contact between the fibers and the surrounding thermoplastic appeared to differ between individual regions, indicating that the effectiveness of reinforcement incorporation was not necessarily uniform throughout the material.

An important aspect of the investigation was the inclusion of four thermoplastic matrices with substantially different molecular structures and processing characteristics. PTFE, PA, ABS, and PC differ in their thermal behavior, rheological response, and molecular interactions, making the matrix itself a major variable in determining composite morphology. The SEM observations suggested that the surrounding polymer influenced the extent to which the reinforcement was embedded and the morphological continuity of the fiber–matrix regions. Differences in the appearance of exposed fibers, local cavities, and interfacial boundaries indicated that the resulting composite structures were not controlled solely by reinforcement identity or concentration. Matrix rheology is particularly relevant during composite production because the movement and deformation of the polymer influence the incorporation and redistribution of the reinforcing phase [33]. Differences in melt viscosity may affect the ability of a polymer to occupy spaces between adjacent fibers and establish close contact with reinforcement surfaces. However, these effects must be considered together with the actual manufacturing conditions used for each material. In summary, SEM characterization demonstrated that the incorporation of glass and carbon fibers modified the morphological characteristics of PTFE-, PA-, ABS-, and PC-based materials. The examined structures revealed differences in reinforcement distribution, fiber–matrix contact, fracture-related features, and localized defects. These observations highlight the interdependence of material composition, manufacturing behavior, and microstructural development. The comparative approach provides a useful foundation for understanding low-content fiber reinforcement in engineering thermoplastics and for guiding the further development of composite materials intended for lightweight aerospace applications.

4. CONCLUSION AND RECOMMENDATIONS

This study investigated the microstructural characteristics of glass fiber (GF) and carbon fiber (CF) reinforced engineering thermoplastics using scanning electron microscopy (SEM). Four polymer matrices, namely polytetrafluoroethylene (PTFE), polyamide (PA), acrylonitrile butadiene styrene (ABS), and polycarbonate (PC), were considered with reinforcement concentrations of 0.5, 1.0, and 2.0 wt.%. The investigation focused on understanding how differences in polymer composition, reinforcement type, and fiber concentration influenced the morphological characteristics of the resulting composite systems. SEM observations revealed that the incorporation of fibrous reinforcements altered the surface morphology and internal structural features of the investigated thermoplastics. Compared with the relatively continuous appearance of unreinforced polymer regions, fiber-containing specimens exhibited more complex morphological characteristics associated with reinforcement distribution and the formation of distinct fiber–matrix boundaries. The examined microstructures demonstrated that the distribution of reinforcing fibers was influenced by both the amount of reinforcement and the characteristics of the surrounding polymer. At lower fiber concentrations, several examined regions exhibited comparatively uniform reinforcement distribution, with individual fibers surrounded by the polymer matrix. As the reinforcement content increased, localized variations in fiber arrangement became more noticeable, including fiber-rich regions and differences in orientation. These observations highlighted the importance of maintaining a suitable balance between reinforcement concentration and microstructural uniformity. Nevertheless, the findings did not establish a universally optimal fiber concentration, since the observed morphology also depended on the selected matrix and reinforcement system. The microstructural examination further identified features associated with fiber–matrix contact, including exposed fibers, interfacial gaps, localized cavities, and fiber pull-out. These characteristics provided qualitative information about the structural continuity of the composite constituents. Differences in the observed interfacial morphology indicated that fiber incorporation did not produce identical structural characteristics in all thermoplastic matrices. The distinct processing and material characteristics of PTFE, PA, ABS, and PC therefore represent important considerations when interpreting the resulting composite morphology. Overall, the SEM findings demonstrated that the microstructural characteristics of fiber-reinforced engineering thermoplastics were governed by the combined influence of polymer matrix selection, reinforcement type, and fiber concentration. The results emphasize the

importance of morphological characterization in the development of thermoplastic composite materials and provide a preliminary structural basis for selecting and refining candidate formulations for aerospace-related components. Although their suitability for specific applications cannot be established through SEM characterization alone, the observed microstructural differences offer useful guidance for subsequent material development and processing optimization.

ACKNOWLEDGMENTS

This book chapter was prepared based on research supported by the Scientific Research Projects Coordination Unit of İstiklal Science and Technology University under Project No. 2025/6-4 BAP.

REFERENCES

[1] Kumar, K., Kumar, S., & Doddamani, M. (2026). Engineering and Additive Manufacturing of High-Temperature Glass Fiber Reinforced Thermoplastic Polyimide Composites: Processing-Structure-Performance Relationships. Journal of Materials Research and Technology.

[2] Kanhere, S. V., Bermudez, V., & Ogale, A. A. (2021). Carbon and glass fiber reinforced thermoplastic matrix composites. In Fiber Reinforced Composites (pp. 273-306). Woodhead Publishing.

[3] Cogswell, F. N. (2013). Thermoplastic aromatic polymer composites: a study of the structure, processing and properties of carbon fibre reinforced polyetheretherketone and related materials. Elsevier.

[4] Sun, L., Wu, S., Chu, D., Wang, T., Shen, W., Li, Z., ... & Xing, S. (2026). Advances in Forming Processes of Carbon Fiber-Reinforced Thermoplastic Composites: From Material Challenges to Interface Engineering. Materials, 19(14), 2988.

[5] Sathishkumar, N., Arunkumar, N., Hariharan, K., Rajasuresh, K., & Skandhakumar, V. (2026). Performance evaluation of GFRP composites reinforced with cryogenically treated S-glass fibers for aerospace applications. Journal of Elastomers & Plastics, 00952443261481360.

[6] Goh, G. D., Dikshit, V., Nagalingam, A. P., Goh, G. L., Agarwala, S., Sing, S. L., ... & Yeong, W. Y. (2018). Characterization of mechanical properties and fracture mode of additively manufactured carbon fiber and glass fiber reinforced thermoplastics. Materials & Design, 137, 79-89.

[7] Davidson, M., Graunke, R., Green, A., Haelsig, H., Heinemann, L., Antony Jose, S., & Menezes, P. L. (2026). Carbon fiber-reinforced polymer matrix composites: Processing, properties, and applications. Fibers, 14(3), 29.

[8] Sarker, T., Ghosh, P. C., Bhuiyan, A. A., Islam, M. R., & Rabbi, M. S. (2026). Advances and evolution of thermoplastic composite materials for aerospace structures: A comprehensive review. Journal of Thermoplastic Composite Materials, 08927057261447758.

[9] Adetunji, E. O., Obukeajeta, O. D., Frank, O., Godwin, A. N., Ayodeji, A. M., & Ayomide, O. J. (2026). A Review of the Mechanical Properties and Applications of Fiberglass Reinforced Polymer Composite. Journal of e-Science Letters.

[10] Guney Yilmaz, S., Ferik, E., Birak, S. B., Ozkutlu Demirel, M., Oz, Y., & Kaboglu, C. (2026). High-performance thermoplastic nanocomposites for aerospace applications: a review of synthesis, production, and analysis. Journal of Reinforced Plastics and Composites, 45(1-2), 237-267.

[11] Eslami-Farsani, R., Bagheri, P., & Nasiri, Z. (2026). A review on recycling methods for glass fibers reinforced thermoplastic polymer composites. Polymers for Advanced Technologies, 37(7), e70691.
[12] Bhowmik, P., Sharma, H., Arora, G., Kumar, M., Dhiman, B., Ayyappan, V., ... & Siengchin, S. (2026). Advances in thermoplastic composites focusing on processing, recyclability, and performance. Discover Mechanical Engineering, 5(1), 64.
[13] Solairaju, J. A., & Thanikodi, S. (2026). Processing structure property relationship of flax/hemp/glass hybrid laminates: multifactor effects of TiO_2, SiC, and fiber sequencing on mechanical and thermal performance. Materials Physics and Mechanics, 54(2), 83-100.
[14] Kim, T., Velikonja, V., & Behdinan, K. (2026). Meta-regression analysis of process-structure-property relationships in additively manufactured continuous carbon fiber composites. Progress in Additive Manufacturing, 1-29.
[15] Rajak, D. K., Wagh, P. H., & Linul, E. (2021). Manufacturing technologies of carbon/glass fiber-reinforced polymer composites and their properties: A review. Polymers, 13(21), 3721.
[16] Oz, M. E., Ekici, B., & Eryılmaz, O. (2025). Aeroelastic analysis of single–ply aramid and glass woven composite wing structures: numerical and experimental approaches. Journal of Innovative Engineering and Natural Science, 5(1), 371-385.
[17] Bharti, R., Mursaleen, M., & Dey, A. (2026). A review of FDM methods, microstructure, and structure–property relationships in polymer composites. Advanced Composite Materials, 1-100.
[18] Rajak, D. K., Wagh, P. H., & Linul, E. (2021). Manufacturing Technologies of Carbon/Glass Fiber-Reinforced Polymer Composites and Their Properties: A Review. Polymers 2021, 13, 3721.
[19] Ab Ghani, A. F. (2021). Hybrid carbon/glass fiber reinforced polymer; a frontier material for aerospace industry: A review on mechanical properties enhancement. Current Science and Technology, 1(2), 41-51.
[20] Efimov, D., Haragâş, S., Cristea, A. F., Alexander, E. G., & Sas-Boca, I. M. (2026). A Critical Review of Polyamide-Based Materials in Advanced Manufacturing: StructureProperty Relationships, Additive Manufacturing, and Technical Constraints in Metal Substitution. Sustainability, 18(21), 10803.
[21] Khan, M. K. A., Mujahid, Y., Alahmed, N., & Khan, K. A. (2026). A review of multifunctional hybrid fiber-reinforced polymer (HFRP)

composites for aerospace applications. Advanced Composites and Hybrid Materials, 9(2), 118.

[22] Asrafali, S. P., Periyasamy, T., & Lee, J. (2026). Structure–Property Relationship of Polybenzoxazine Composites for Advanced Applications. Polymers, 18(15), 1870.

[23] Çetin, M. E. (2021). Increasing low-velocity impact strength of glass fiber sandwich composites with nanoparticle reinforced adhesive. Gazi Üniversitesi Fen Bilimleri Dergisi Part C: Tasarım ve Teknoloji, 9(3), 492-504.

[24] Bock, C., Ellis, B., & Rais-Rohani, M. (2026). Investigating Process–Structure–Property Relationships in Large-Scale Additively Manufactured Carbon-Filled PETg. Materials, 19(11), 2270.

[25] Sheth, M. R., Raj, L., Raj, M., & Rathva, P. (2026). Hydroquinone-based multifunctional unsaturated polyester–epoxy resin systems and its carbon fiber-reinforced composites: Fabrication, characterization, and structure–property relationships. High Performance Polymers, 09540083261483348.

[26] Ürgün, S., Fidan, S., Yarar, E., Özsoy, M. İ., & Bora, M. Ö. (2026). Thermomechanical Properties of Carbon and Glass Fiber-Reinforced Epoxy Composites as Function of Drilling Parameters. Polymers, 18(19), 2316.

[27] Alshammari, B. A., Alsuhybani, M. S., Almushaikeh, A. M., Alotaibi, B. M., Alenad, A. M., Alqahtani, N. B., & Alharbi, A. G. (2021). Comprehensive review of the properties and modifications of carbon fiber-reinforced thermoplastic composites. Polymers, 13(15), 2474.

[28] El Magri, A., Vanaei, H. R., El Hakimi, A., & Hammouti, B. (2026). Process-Structure-Property Relationships and Multi-Response Optimization of Z-Direction MEX-Printed Polyphenylene Sulfide.

[29] Hussain, M., Alsenaani, F., Khalil, A., Albazi, A., Bahaeddin, F., Al-Mazrouei, N., & Mohammad, A. F. (2026). Structure–Property Relationships of Polylactic Acid Composites Reinforced with Chemically Recycled Carbon Fibers from CFRP Waste. Recycling, 11(6), 109.

[30] Yadav, V. V. V., Kumar, M. H., Bal, S., Techawinyutham, L., Rangappa, S. M., & Siengchin, S. (2026). Basalt Fiber-Reinforced Thermosetting Polymer Composites: A Critical Review of Fiber Properties, Interfacial Engineering, Hybridisation, Durability, and Applications. Journal of Vinyl and Additive Technology.

[31] Tarih, Y. S., Acar, V., Gündoğdu, Ö., & Yar, A. (2024). Vibration response of thermoplastic veil interleaved carbon fiber reinforced epoxy composites. Türk Doğa ve Fen Dergisi, 13(1), 128-132.

[32] Omar, N. W. Y., Shuaib, N. A., Hadi, M. A., & Azmi, A. I. (2019, November). Mechanical properties of carbon and glass fibre reinforced composites produced by additive manufacturing: A short review. In IOP Conference Series: Materials Science and Engineering (Vol. 670, No. 1, p. 012020). IOP Publishing.

[33] Jayabal, R., Kumar, N., Bhikhuprasad Dave, D., Santhosh, M. B., Pratap Singh, A., Basheer, S., ... & Kamakshi Priya, K. (2026). Sustainable Fiber–Reinforced Polymer Nanocomposites: Processing–Structure–Property–Performance Relationships and Machine Learning–Driven Design. Journal of Natural Fibers, 23(1), 2705003.